

Bangor University

DOCTOR OF PHILOSOPHY

Anisotropic Magnetic Nanoparticles as Reporters in a Magneto-optic Bidiagnostic System

Armstrong, Oliver

Award date:
2020

Awarding institution:
Bangor University

[Link to publication](#)

General rights

Copyright and moral rights for the publications made accessible in the public portal are retained by the authors and/or other copyright owners and it is a condition of accessing publications that users recognise and abide by the legal requirements associated with these rights.

- Users may download and print one copy of any publication from the public portal for the purpose of private study or research.
- You may not further distribute the material or use it for any profit-making activity or commercial gain
- You may freely distribute the URL identifying the publication in the public portal ?

Take down policy

If you believe that this document breaches copyright please contact us providing details, and we will remove access to the work immediately and investigate your claim.



PRIFYSGOL
BANGOR
UNIVERSITY

DOCTORAL THESIS

**Anisotropic Magnetic Nanoparticles as
Reporters in a Magneto-optic
Biodiagnostic System**

Author: Oliver L. Armstrong
MSc BSc

Supervisor: Dr. P. John
Thomas

*A thesis submitted in fulfilment of the requirements
for the degree of
P.hD in Chemistry
in the*

Dr. J. Thomas' research group
in the Department of Chemistry

June 12, 2020

Declaration of Authorship

I, Oliver L. ARMSTRONG, declare that this thesis titled, “Anisotropic Magnetic Nanoparticles as Reporters in a Magneto-optic Biodiagnostic System” and the work presented in it are my own. I confirm that:

- This work was done wholly or mainly while in candidature for a research degree at this University.
- Where any part of this thesis has previously been submitted for a degree or any other qualification at this University or any other institution, this has been clearly stated.
- Where I have consulted the published work of others, this is always clearly attributed.
- Where I have quoted from the work of others, the source is always given. With the exception of such quotations, this thesis is entirely my own work.
- I have acknowledged all main sources of help.
- Where the thesis is based on work done by myself jointly with others, I have made clear exactly what was done by others and what I have contributed myself.

Signed:

Date:

Abstract

This project was concerned with the design and fabrication of asymmetric nanoparticles with desirable magnetic and optical properties, to be used as reporter particles in a bio-diagnostic system. This diagnostic system has certain criteria as to how the reporter particles' properties must be so that they are of use. Throughout this project several chemical processes have been explored for producing nanoparticles with an elongated dimension so that they are of a rod or wire shape. A large part of the work has centered on producing iron oxide rod cores to provide the magnetic component, and then with subsequent coating of gold and silver nanoparticles to provide the optical properties required. The magnetic properties of the core have attempted to be manipulated by use of a co-precipitation synthesis to dope the lattice with transition metals. Digestive ripening, iterative coating of noble metals and interface coating are three of the synthetic routes that have been explored to coat the produced cores with gold and silver.

We have also looked at two alternative routes to producing surrogate reporter nanoparticles with inherently different properties. One of which was using the so-called Polyol reduction method to producing a silver-nickel composite nanowire. The second was a hydrogenation reduction of cobalt precursors, with a subsequent gold coating. The nickel and cobalt components of these alternatives provide the magnetic part, with noble metals again fulfilling the optical requirements.

The resulting particles synthesised in these experiments have subsequently been analysed through a variety of analytical techniques, to characterise their structural, morphological, magnetic and optical properties. The best candidate particles were tested for their applicability to the target bio-diagnostic magneto-optic system.

Acknowledgements

Initially and primarily, I would like to sincerely thank my project supervisor and academic lead, Dr. J. Thomas. His ability to tune concepts into more relatable notions, unflappable approach to obstacles and soft influence has greatly helped me grasp the tasks required in this project and to develop beyond the basic assignment. Dr. Thomas' input has proved invaluable to guiding experimental developments, while providing the all too important freedom to explore avenues other than the "safe" option required for true research. His support and enthusiasm for my attendance at conferences and other outreach opportunities has equally developed my skills out of the lab.

Secondly a tribute must be made to my project supervisors based in our company partner, Dr. J. Bowen and Dr. C. Allendar. Both of whom have provided great support throughout this project; their affable demeanour instantly quelled any initial nervousness, while providing solid leads as to where experimentation should be made, and allowing unabridged access to specialist equipment. Transparent working between this project and the developments of the company have allowed for this work to be directed to good affect.

Visits to the partner company premises lead to close working with Dr. S. Eppler and Dr. R. Matelon. Both of these people added a great amount to this project, sharing practical knowledge, helping with use of equipment and other invaluable guidance.

I would like to strongly acknowledge Dr. L. Francis and other staff at the International Iberian Nanotechnology Laboratories, in Braga, Portugal. His openness, enthusiasm to collaborate and provide access and training on high value equipment under his management has proven invaluable for this project, and many key developments and quality analysis would not have been made without his input.

Thanks must also be made to all the academic staff at the former School of Chemistry at Bangor University, who were always more than happy to help out within the department, provide advice on specialist areas, sharing of equipment and other important aspects to help their students progress. It is truly woeful that these talented academics and tutors may be lost from this institution through no fault of their own. Similarly other chemistry

students both undergraduate and postgraduate within the department for being part of a friendly, open and collaborative environment.

Technicians in both the Chemistry and Electronic Engineering departments must also receive thanks. Their unwavering commitment to helping all students, provide training of equipment and source any required items is imperative to the research.

Thank you also for the optical simulations kindly performed for me by fellow PhD candidate James Monks.

Tremendous gratitude is also directed to the Welsh Government for their support of this project through the Knowledge Economy Skills Scholarship (KESS) funding program, established with European Structural Funds (ESF). The funding has facilitated this research and collaboration between academia and industry, whilst enabling dissemination and collaboration throughout Europe which has only occurred thanks to this scholarship.

Finally I am immensely grateful for the support and encouragement from family, friends and loved ones throughout this process. Through whatever peaks or troughs I have experienced these past years your love and commitment has sustained me to toil in the tough parts, and then inspired me to take stock and enjoy the summits.

Contents

Declaration of Authorship	i
Abstract	iii
Acknowledgements	v
1 Introduction	1
1.1 Unique Properties of Nanoparticles: the Importance of Surface vs. Bulk Atoms	2
1.1.1 Optical Properties	5
1.1.2 Magnetic Properties	10
1.2 Magneto-optic Theory	13
1.3 Crystal Growth	16
1.3.1 Capping agents / Surfactants	18
1.3.2 Structure Directing Agents	19
1.4 Synthesis Processes	19
1.4.1 Forced Hydrolysis	19
1.4.2 Noble Metal Coating	20
1.4.3 Digestive Ripening	20
1.4.4 Interface Coating	21
1.4.5 Polyol Reduction	21
1.4.6 Hydrogenation Reduction	22
1.4.7 Pickering Emulsions	22

1.5	Biphasic Fluid Interfaces	23
1.6	Analysis Techniques	24
1.6.1	Electron Microscopy	24
	SEM	25
	TEM	26
	Associated Techniques	27
1.6.2	UV/Vis Spectroscopy	28
1.6.3	Powder X-ray Diffraction Crystallography	29
1.6.4	Raman Spectroscopy	29
1.6.5	Thermo-gravimetric Analysis	30
1.6.6	Nuclear Magnetic Resonance Spectroscopy	30
1.6.7	Vibrating Sample Magnetometry	31
1.6.8	Magneto-optic Test Setup	31
1.7	Project Aims	32
2	Hematite Nanorice Core Synthesis	35
2.1	Introduction	36
2.2	Forced Hydrolysis Synthesis	36
2.2.1	Original Published Method	36
2.2.2	Influence of Co-precipitating Agents	37
2.3	Hematite Structure and Other Iron Oxide Phases	39
2.4	Experimental	41
2.4.1	Results and Discussion	42
	XRD	43
	Raman	44
	Electron Microscopy	45
	Thermo-gravimetric Analysis	48
	Vibrating Sample Magnetometry	48
2.5	Conclusions	50
3	Doping of Hematite Core with Transition Metals	53
3.1	Introduction	54

3.2	Doping to Influence Magnetism	55
3.3	Experimental	55
3.3.1	Results and Discussion	56
	XRD	57
	Raman	59
	Electron Microscopy	60
	Magneto-optic System	62
3.4	Conclusions	64
4	Noble Metal Coating	65
4.1	Introduction	66
4.2	Simulated Optical Resonances	66
4.3	Published Methods to Formation of Metal Coats	68
4.3.1	Linker Group Functionalisation	68
	APTES / APTMS	69
	Polyelectrolyte	70
	Silicate	71
4.3.2	Growth of noble metal shells	72
	Duff's gold seeds	72
	Turkevich gold seeds	73
	Gold Seeds by NaBH_4 reduction	74
	Shell Deposition with Formaldehyde	74
	Shell Deposition with Formaldehyde - via THPC	74
	Shell Deposition with Hydroxylamine	75
	Shell Deposition with Ascorbic Acid	75
	Shell Deposition with CO	76
	Shell Deposition with Sodium Citrate	76
	Shell Deposition with NaBH_4	76
4.4	Experimental	76
4.4.1	Results and Discussion	78
	Electron Microscopy	78
	TGA	80

4.5	Conclusions	82
5	Digestive Ripening for Shell Deposition	85
5.1	Introduction	86
5.2	Size Focussing	86
5.3	Digestive Ripening Agent	88
5.4	Experimental	90
5.4.1	Results and Discussion	91
	UV/Vis	91
	Electron Microscopy	93
5.5	Conclusions	95
6	Interface Coating	97
6.1	Introduction	98
6.2	Previous work	99
6.3	Interface coating	100
6.4	Experimental	101
6.4.1	Results and Discussion	102
	UV/Vis	102
	Electron Microscopy	104
	Magneto-optic System Testing	109
6.5	Conclusions	111
7	Polyol Synthesis of Silver and Nickel Composites	113
7.1	Introduction	114
7.2	Polyol solvent	115
7.3	Silver nanowires	116
7.3.1	PVP	117
7.3.2	Seeds and Etchants	119
7.4	Experimental	120
7.4.1	Results and Discussion	121
	XRD	122
	Raman	123

Electron Microscopy	124
7.5 Conclusions	126
8 Cobalt Nanorods Synthesised by Hydrogenation Reduction	127
8.1 Introduction	128
8.2 Experimental	129
8.2.1 Results and Discussion	130
Electron Microscopy	130
8.3 Conclusions	132
9 Pickering Emulsions	133
9.1 Introduction	134
9.2 Experimental	135
9.2.1 Results and Discussion	135
Optical Microscopy	137
Electron Microscopy	138
Nuclear Magnetic Resonance Spectroscopy	141
9.3 Conclusions	142
10 Conclusions and Future Work	143
A Table of Digestive Ripening Experiment Conditions	151
B Table of Interface Coating Experiment Conditions	157
C Table of Polyol Experiment Conditions	163
D Supplementary HRTEM images	169
Bibliography	175

List of Figures

1.1	Histogram plots with data acquired from webofknowledge.com literature search function. The top graph shows the number of publications for the labelled search term over an 18 year period from the millennium. The bottom graph relates to the same 18 year period counting the number of publications in certain research areas for the same search terms	3
1.2	Plot of surface atom percentage to total number of atoms for nanocrystals ¹	5
1.3	Images of Lycurgus cup showing the difference between transmitted and reflect light through the glass.	6
1.4	Part a. diagrammatically demonstrates the principle of LSPR, where part b. shows optical absorption spectra of spherical gold nanoparticles of the noted diameters. ²	8
1.5	Diagrammatic representation of the two separate resonance modes of a rod-shaped particle. Part a. shows transversal resonance mode while part b. shows the longitudinal resonance with incident electromagnetic radiation ³	9
1.6	Diagrammatic representation of magnetic spin moments in zero external magnetic field	10
1.7	Hysteresis loops, or magnetisation vs. applied magnetic field plots, of the labelled magnetic classes ⁴	11
1.8	Diagram demonstrating the principle of this biodiagnostic system with anisotropic magnetic reporter particle, upon protein binding to reporter particle sees an increase in hydrodynamic area and hence phase lag ⁵ . . .	14

1.9	Graphical representation of the LaMer model of nucleation, where C_{∞} and C_{crit} indicate the equilibrium concentrations of the bulk material and critical concentration for nucleation from solution respectively ⁶ . . .	17
1.10	Diagram of nanoparticles of subsequent shells on one central atom, with labelled total atom numbers ⁷	18
1.11	Schematic comparing emulsions stabilised with molecular and solid particulate surfactants ⁸	23
2.1	Crystal structure of akaganeite (β -FeOOH) showing preferential bi-dentate binding of phosphate (blue balls) over mono-dentate binding positions (red balls), green balls indicate position of chloride ions commonly found in akaganeite	39
2.2	Crystal structures of: (a) hematite and (b) akagenite. Brown shapes represent iron valency, red balls; oxygen atoms and green balls; chloride ions	40
2.3	XRD plots of nanorice particles sampled at 24 and 72 hours of heating, and reference data of hematite and akaganeite	43
2.4	Raman spectroscopy data of samples prepared at 24 and 72 hours of heating, alongside a reference hematite spectra	44
2.5	SEM images of hematite spindles resulting from 72 hours of 100°C heating in forced hydrolysis of FeCl ₃ with KH ₂ PO ₄	46
2.6	HRTEM images of hematite spindles resulting from 72 hours of 100°C heating in forced hydrolysis of FeCl ₃ with KH ₂ PO ₄ , with inset electron diffraction patterns and expanded lattice interference	46
2.7	TEM images of precipitates at: image a. 24 hours, and image b. 48 hours of heating, with inset electron diffraction patterns	47
2.8	Histograms with fitted distribution curves compiled from measurements of 593 particles seen in figure 2.5	49
2.9	VSM of hematite nanorice formed after 72 hours of heating	50
3.1	XRD plots of α -Fe ₂ O ₃ nanorice doped with 3 different transition metals: cobalt, nickel and copper. The bottom data plot is that of undoped α -Fe ₂ O ₃ nanorice particles, with labelled lattice indices	57

3.2	XRD plots focussed to 31–37° of particles doped with; nickel, cobalt and copper in images a., b. and c. respectively with increasing proportions of up to 10%	58
3.3	Raman spectra of hematite nanorice core, and 10% doping of cobalt, nickel and copper	59
3.4	Raman spectra of hematite nanorice core (SP9 - prepared in chapter 2), and 10% doping of cobalt, nickel and copper, focussed on the A_{1g} peak between 200–250 cm^{-1}	60
3.5	SEM and TEM images of nanorice particles doped with cobalt, image a. is of 5% cobalt and image b. 10% cobalt	61
3.6	SEM image of 5% nickel doped hematite nanorice, with expanded areas of interest. Inset image a. shows the close packing arrangement of spindle particles, with inset image b. showing a cluster of these agglomerated particles along the opposing axis	62
3.7	Plots of amplitude against frequency, and phase against frequency for nanorice particles doped with 5% nickel, 10% cobalt, 10% copper, and sample IC50 for reference (chapter 6)	63
4.1	Graph showing simulated longitudinal resonance of $\alpha\text{-Fe}_2\text{O}_3$ nanorice coated with 10 nm of either gold or silver	66
4.2	Scheme detailing the various possible attachments of APTES to iron oxide via surface hydroxyl groups ⁹	69
4.3	SEM and TEM images of gold seeds deposited on hematite nanorice cores via APTES linking group. Image a. shows an SEM image of a group of these particles, whereas b. and c. are TEM images with inset electron diffraction patterns	79
4.4	HRTEM images of silver seeds deposited on hematite nanorice cores via APTES linking group. Image a. shows a group of these particles, whereas b. shows HRTEM–EDX mapping images, showing the spatial data of certain elements	80

4.5	Thermo-gravimetric analysis data plot of hematite nanorice, nanorice functionalised with APTES and of nanorice with deposited gold seeds via APTES group	81
5.1	Diagram showing the role of digestive ripening agent in this process ¹⁰ . .	88
5.2	UV/Vis spectroscopy of samples DR51, 52 and 53	92
5.3	HRTEM–EDX mapping of sample DR51	93
5.4	HRTEM image of sample DR52 with inset electron diffraction pattern . .	94
5.5	HRTEM images of cores coated with varying amounts of gold. Images a., b., c. and d. are of samples DR45, 46, 47 and 48 respectively, while image e. shows HRTEM–EDX mapping of sample DR42	96
6.1	Diagram showing the equilibrium position of a spherical particle at the interface of two liquids, resulting in a reduction of interfacial tension ¹¹ . .	98
6.2	Diagram showing coating of hematite nanorice core with gold and silver particulates when suspended at the interface of water and toluene phases.	100
6.3	UV/Vis absorption spectra of four hematite nanorice cores coated at the toluene-water interface; with either gold, or gold and silver.	102
6.4	HRTEM–EDX mapping of hematite cores with gold and silver deposited at the interface, series a. is of silver grown on gold seeds, whereas series b. is of a 50:50 mix of gold and silver grown on gold seeds	105
6.5	TEM images of IC18 and IC20 samples: row a. is of IC18 with an inset electron diffraction pattern in the top right corner; row b. is of IC20 . . .	106
6.6	TEM and SEM images of IC34 sample	107
6.7	TEM images of IC50 sample	108
6.8	TEM images of IC65 sample, with inset electron diffraction pattern in the top right corner	109
6.9	Plots of amplitude against frequency, and phase against frequency for samples IC18, 50 and 65 in DI water and 25% /w glycerol solutions . . .	110
7.1	Diagram showing how PVP preferentially protects the (100) crystal face of silver nanowires ¹²	118

7.2	Diagram detailing the mechanism by which copper ions facilitate the growth of silver nanowires ¹³	120
7.3	XRD data plot of sample NW46	122
7.4	Raman spectra of sample NW46	123
7.5	HRTEM images of sample NW46	124
7.6	HRTEM-EDX mapping of particles formed by reduction of nickel precursor	125
8.1	Images showing phase transfer step of cobalt ions from aqueous to organic solvents	129
8.2	HRTEM images of cobalt and cobalt oxide nanoparticles formed after hydrogenation reduction reaction, with inset electron diffraction pattern, row a. is of sample 29 and row b. shows sample 24	131
9.1	Schematic illustration of the Pickering emulsion synthesis scheme with silver precursor.	134
9.2	Pickering emulsions prepared with silver nanoparticles by the method detailed with phase soluble dyes to demonstrate presence of emulsions, in each image the left vial contains no THPC hence no emulsions formed and both right vials were prepared as normal with THPC. Image (a) shows an aqueous soluble red dye, with image (b) showing a lipophilic solvent dye	136
9.3	Photographs showing droplets of oil present in the majority water layers. Image (a) shows freshly prepared emulsion with silver, opposed to (b) which is imaged 3 months after initial preparation. Images (c) and (d) show Pickering emulsions prepared with gold nanoparticles, freshly made and aged 1 month respectively.	137
9.4	Histogram plots of droplet diameter size from fresh and aged samples of Pickering emulsions stabilised with silver and gold nanoparticles, plots a., b., c. and d. are measured from droplets seen in the relevant images seen in figure 9.3	139

9.5	HRTEM images of nanoparticles synthesised in-situ of Pickering emulsion preparation. Image (a) shows as formed gold nanoparticles, with image (b) showing silver nanoparticles with an inset image of the nanoparticles after 3 months of ageing in emulsion condition. The main images a. and b. both have scale bars of 10 nm	140
9.6	^1H NOSEY 2D NMR spectra of (a.) silver nanoparticles produced at the interface of toluene and water, and (b.) silver nanoparticles synthesised with the same reducing agents, however solvent in a mix of CH_3OH and H_2O	141
D.1	HRTEM image of sample DR42 with inset electron diffraction pattern . .	170
D.2	HRTEM-EDX image and mapping of sample DR51 showing presence of gold-silver core-shell morphology deposited on hematite core	171
D.3	HRTEM-EDX image of NW46 showing presence of silver only	172
D.4	HRTEM image of crystalline nickel or nickel oxide particles produced from reduction of $\text{Ni}(\text{CH}_3\text{CO}_2)_2 \cdot 4\text{H}_2\text{O}$ in ethylene glycol	173

List of Tables

2.1	Centrifuge washing regime followed with a centrifugal force of 2400 xg / 4500 xrpm	42
2.2	Peak positions and phonon assignments of Raman spectra in figure 2.4 . .	44
2.3	Calculated interplanar distances of hematite lattice planes	48
3.1	Table of ionic radii ¹⁴ discussed in this chapter	56
5.1	Table presenting difference in proportion of gold and silver precursors used in synthesis of conditions presented in figure 5.2	91
5.2	Table presenting difference in proportion of gold precursor to seeded core particles used in the synthesis of conditions presented in figure 5.5	95
6.1	Table presenting differences in the synthesis conditions presented in figure 6.3	103
A.1	Table of digestive ripening experiments performed (chapter 5)	152
B.1	Table of interface coating experiments performed (chapter 6)	158
C.1	Table of polyol experiments performed (chapter 7)	164

List of Abbreviations

LSPR	Localised Surface Plasmon Resonance
XRD	X-Ray Diffraction Crystallography
SEM	Scanning Electron Microscopy
TEM	Transmission Electron Microscopy
UV/Vis	UltraViolet/Visible Spectroscopy
NP	Nano Particle
EDX	Energy Dispersive X-ray Spectroscopy
EELS	Electron Energy Loss Spectroscopy
AFM	Atomic Force Microscopy
SQUID	Superconduction Quantum Interference Device Magnetometry
VSM	Vibrating Sample Magnetometry
TGA	Thermo-Gravimetric Analysis
XPS	X-ray Photoelectron Spectroscopy

List of Symbols

r	distance	m
Δ	difference	–
γ	interfacial energy	Nm ^{−1}
ω	angular frequency	rad
θ	relative angle	°
\AA	Angstrom	10 ^{−10} m
φ	phase lag	°

List of Analytical Equipments

FEI Quanta 650 FEG Environmental SEM

Hitachi TM4000Plus SEM

JEOL JEM 2100 80-200kV

Probe-Corrected FEI Titan G2 80-200kV ChemiSTEM

Philips X'Pert Powder X-Ray Diffractometer, Cu K- α 1.541 Å radiation source

Renishaw Model 1000 Ramascope, 633 nm laser source

Perkin Elmer Lambda 35 UV/Vis spectrometer

Agilent Cary 60 UV/Vis spectrometer

Brüker 400 MHz Nuclear Magnetic Resonance Spectrometer

TA instruments SDT Q600

Magneto-optic reporter-nanoparticle application test system

Bioforce Nano eNabler Molecular Printing System, onboard digital microscope $\leq 700\times$ magnification

Chapter 1

Introduction

This introduction will serve as an overview to the reasons why this project has been undertaken, a brief review of the literature in a way to be aware of the background research that already exists relevant to the work, and the brief aims that are hoped will be met through this project. An induction will also be made into the chemical processes explored and the analytical means by which the produced particles have been studied.

1.1 Unique Properties of Nanoparticles: the Importance of Surface vs. Bulk Atoms

Nanoparticles have been used for centuries owing to their unique properties, albeit often unawares of the users as to the reasons behind these novel properties. These particles of matter are on such a small scale that more novel and revolutionary techniques of analysis have been required to characterise and observe them, and as such they have been studied intensely for the past few decades as one of the fastest growing areas of scientific research.¹⁵ As illustrated in figure 1.1 it is seen that in this millennium there has been a sharp increase in at least the word “nanoparticle” being used in scientific publications, alongside this we can see that chemistry and related subjects such as electro-chemistry take the lions share of these publications. This shows that conceptual understanding and chemical knowledge is vital to research in the nanoscience field, and to harnessing the novel properties due to the atomistic control that can be performed using a “bottom-up” approach. However, looking at publications using the terms “nanocrystal” and “nanorod” their increased use in the literature has been more gradual over the years, but do find more comparable use in total when considering the field in which they are mentioned such as chemistry, material science and physics among others.

The definition of a “nanoparticle” is a material which usually has at least 2 of 3 dimensions in the region of 1 nm - 1 μm .^{1,2,16} Typical nanoparticles have all their size vectors in the nm range but exceptions have been made for nanowires and rods who’s longest vector can extend into μm lengths, as these particles can still exhibit novel properties not observed of the material in bulk.

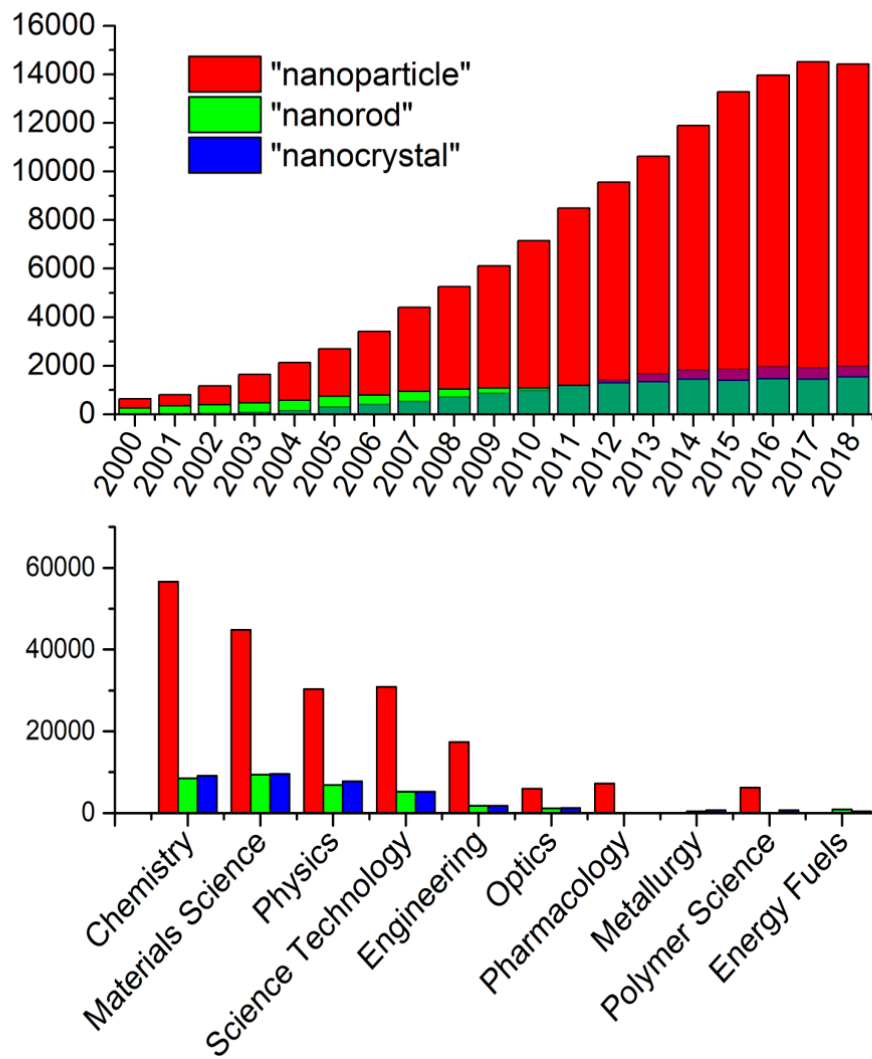


FIGURE 1.1: Histogram plots with data acquired from webofknowledge.com literature search function. The top graph shows the number of publications for the labelled search term over an 18 year period from the millennium. The bottom graph relates to the same 18 year period counting the number of publications in certain research areas for the same search terms

The field of nanoscience can be traced back to origin with the works of Michael Faraday in his Bakerian lecture in 1857.^{17–19} Notably his discovery and discussion of colloids of gold; that being nano-particulate gold dispersed in a fluid, owning different optical properties to the bulk material. This was the first time that it was not just observed that this form of the material having the same chemical make-up as the bulk material exhibited different properties, but that a reasoning behind this difference was discussed and attributed to the particles' size.

Great attention was also brought to this field from a famous lecture given by the physicist Richard Feynman, titled “There’s Plenty of Room at the Bottom: An Invitation to Enter a New Field of Physics” given in 1959. Although his talk didn’t kick-start the field immediately, it was the themes in his talk about future application of miniaturisation and control at the atomic scale that came to pass in the 1980s that gained the talk widespread acceptance and status. In the talk he mused that when individual atoms could be manipulated and designed mechanically then existing processes such as chip design could be greatly condensed, and a greater resolution of surface analysis techniques could be gained, which was realised with the inception of Atomic Force Microscopy (AFM) and other techniques subsequently. In the talk he also set out two prized challenges: one was to produce a tiny motor of micro or nanoscale which could turn potential energy into movement, and second to suitably develop a scaled down way of patterning a material, so that the Encyclopædia Britannica could fit on to the head of a pin. Both these challenges were met and the \$1000 prizes claimed by 1985. The first challenge was satisfied by a talented craftsman William McLellan in 1960 who crafted a minuscule motor, but he used only conventionally available tools so didn’t substantially develop the field. The second challenge was met by Tom Newman who met the task by patterning a chapter from the book by Charles Dickens: *A Tale of Two Cities*, at a scale of 1/25,000 using an electron beam which matched the requirement for claiming the prize.

In the literature it is talked about the importance of surface to bulk atoms in the context of nanoparticles as when we look at smaller and smaller dimensions the materials start to approach the size of atoms themselves, which are the constituents of any material.^{16,20} As we approach the size of atoms, our particles necessarily have greater and greater proportions of surface atoms as opposed to bulk atoms.¹⁵ A simple demonstration of

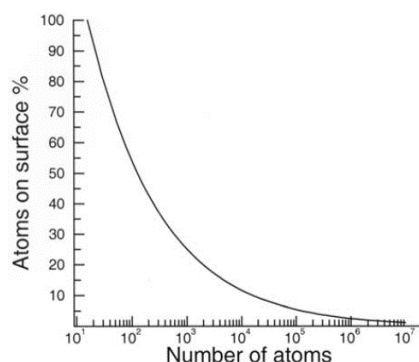


FIGURE 1.2: Plot of surface atom percentage to total number of atoms for nanocrystals¹

this is picturing a cube of given atoms shrinking in size, with edges of 1 cm then 1×10^{-5} atoms will be surface atoms. As the cube's dimensions are decreased to 10 nm then 10% of atoms are surface atoms, and further when the cube has 1 nm edges, every atom will exist at the cube's surface.² This relationship is presented in the case plot in figure 1.2.¹ This is an obvious conclusion as bulk atoms form the internal part of a particle with no external face, and the surface atoms are those which are present at the surface or outside of the particle, which are inherently less stable and easier to interact with an external force or chemistry.^{21,22}

1.1.1 Optical Properties

The optical properties of nanoparticles are one of the most widely known effects of taking a bulk material down to nanoscale vectors.^{15,20,23} These effects were the first recorded novel properties of nanoparticles as discussed in the section above, where Michael Faraday discussed the varying optical properties of various gold colloids, which were found to deviate from the colour of gold in bulk which affords its precious metal status.^{17,18,24} This size effect is also responsible for the use of nanoparticles; preceding their understanding or theoretical conception, in historical artefacts such as the Roman made Lycurgus cup seen in figure 1.3.



FIGURE 1.3: Images of Lycurgus cup showing the difference between transmitted and reflect light through the glass.

The Lycurgus cup is an interesting item in that it displays simply the phenomenon of optical dichroism, where depending on the direction of light the glass with embedded nanoparticles displays as a different colour.^{15,24–27} So in the case of this item when light is shone at the cup from an external point the cup appears a pale green colour via reflected light, when the light source is placed inside the cup and we observe the transmitted light a strong red colour is seen.

Since the 1950s and the Lycurgus cups' transfer from private owners to the British Museum several studies have looked at the cup to determine how it holds such intriguing properties. Early studies with X-Ray Diffraction Crystallography (XRD) confirmed that the cup was indeed a glass rather than jade or another material, and with qualitative analysis gold, silver and other trace elements were seen. Later studies found the presence of gold and silver was primarily responsible for the optical dichroism, but in an effort to recreate the effect it was found that simply adding metal nanoparticles to glass didn't initially work, so how the colloid was formed was proved to be of import. Metal colloidal particles were later observed with Transmission Electron Microscopy (TEM) with sizes ranging from 50–100 nm of typically spherical morphology, and it was stated that the gold should be responsible for the red transmitted colour and silver the green reflected colour.^{26,27}

In another pre-modern example, metallic nanoparticles were commonly embedded again

1.1. *Unique Properties of Nanoparticles: the Importance of Surface vs. Bulk Atoms* 7

in glass to design vibrantly coloured stained glass windows.^{18,20,28} When these samples were studied using modern analytical techniques like TEM and XRD, it was found that specific morphologies and sizes of nanoparticles were responsible for the strong colourations, covering a broad visible spectrum. It must be re-iterated that the glass-smiths and crafts' people were not aware that they were using nanoparticles in particular, as they had no means or reason to conclude such.

Mie theory allows calculations of the wavelength of light that will be resonant with any particular Localised Surface Plasmon Resonance (LSPR) of a nanoparticle, pioneered by the originator of the method, Gustav Mie in 1908.^{2,19,20,29–34} Mie's theory takes an approximation of Maxwell's equation to describe the interaction of incident electromagnetic radiation with solid particles and their charged electron particles. The LSPR of a metallic nanoparticle describes the in time oscillation of free electrons from the particle, in phase with the incident radiation.^{33–35} This is shown diagrammatically in figure 1.4 a. Metallic nanoparticles measuring tens of nm typically can be resonant with visible wavelengths of light and can show large absorbency in this range. As the particle increases in size, it becomes resonant with longer wavelengths of incident radiation, so a red shift is observed as seen in figure 1.4 b.^{2,34,36,37}

Not only is the size of the nanoparticle linked to the optical properties of the colloid: the shape and context of the particle also will tune this attribute.^{35–43} Particularly smaller sized nanoparticles <10 nm, or quantum dots, are able to form as a larger number of morphologies, however above this size a select number of morphologies are preferred as being energetically favourable.³⁵ Returning to the small sized nanoparticles, strong resonances are able to be made with specific incident energies due to the confined dimensions, and slight changes in morphologies can tune these resonances. Moreover with further growth to larger nanoparticles resonances tend to broaden and diminish in intensity,³⁶ as seen in figure 1.4 b. It is important to recognise that the Mie approximation for LSPR is for spherical morphologies, and must be adjusted for other particle morphologies.

When considering elongated or rod shaped particles a clear change in optical resonance properties is observed, where two resonance peaks are evolved from the single case of spherical particles. Gans theory is an adaptation of the Mie approximation of LSPR for spherical particles, and predicts these two resonance modes of a rod shape relative to the

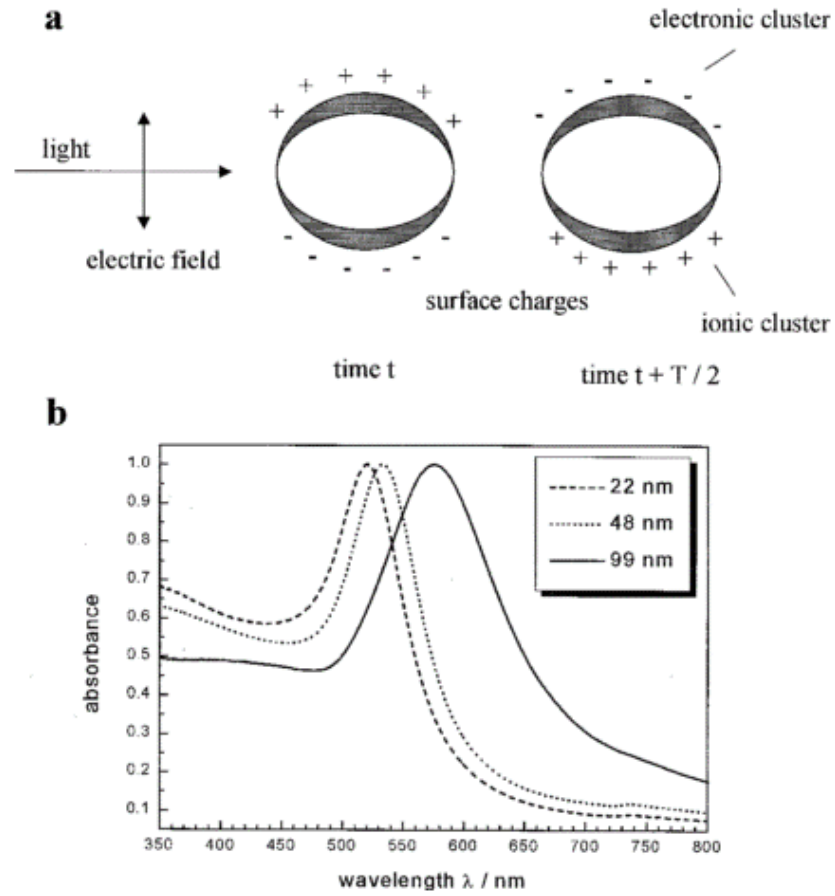


FIGURE 1.4: Part a. diagrammatically demonstrates the principle of LSPR, where part b. shows optical absorption spectra of spherical gold nanoparticles of the noted diameters.²

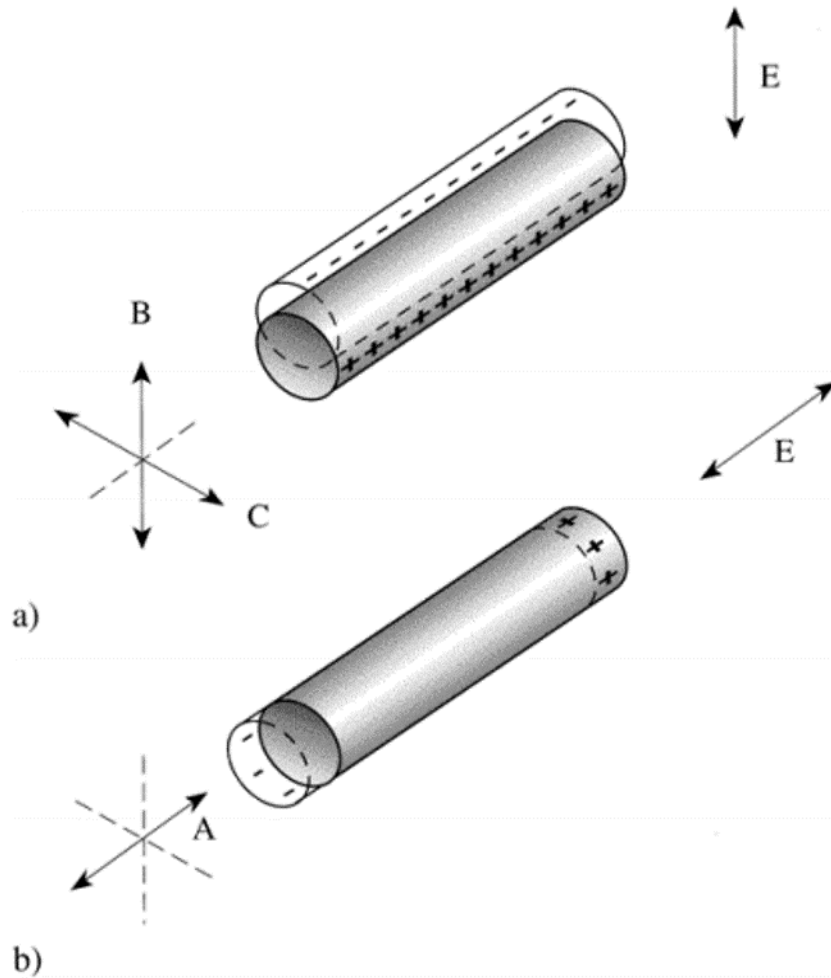


FIGURE 1.5: Diagrammatic representation of the two separate resonance modes of a rod-shaped particle. Part a. shows transversal resonance mode while part b. shows the longitudinal resonance with incident electromagnetic radiation³

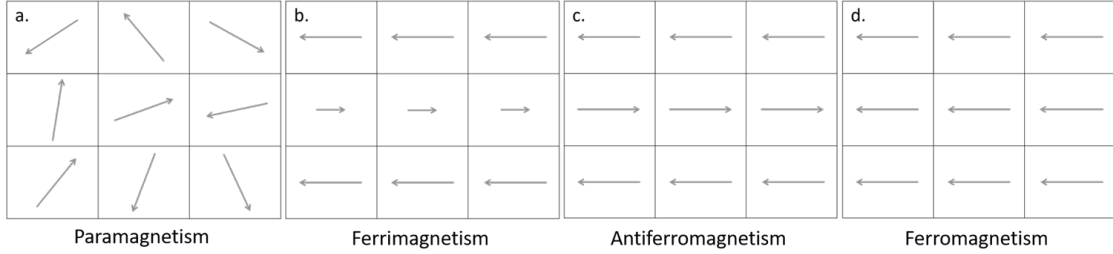


FIGURE 1.6: Diagrammatic representation of magnetic spin moments in zero external magnetic field

incident electromagnetic radiation.³ These two modes are demonstrated in figure 1.5, where plasmon oscillation with the field results in a dipole through temporary charge separation.

1.1.2 Magnetic Properties

The magnetic properties of particles are also subject to the size and structure of the particle, and we can see the rise of new magnetic classes that are not seen in bulk materials. Individual isolated atoms of all types will typically have some magnetic moment, which can be derived using Hund's rule where degenerate electronic states are first filled with single electrons before pairing, usually resulting in some net magnetic moment as discussed. This is in contrast to only a few chemical elements in bulk retaining some significant magnetic property.^{1,44}

There are four main classes of magnetism to be concerned with in this project: Paramagnetism, Ferrimagnetism, Anti-ferromagnetism and Ferromagnetism. These classes can be briefly described diagrammatically by the relative moments of magnetic spins within that material, and is shown in figure 1.6.

Paramagnetic materials are made up of atoms or ions with magnetic moments or spins which are arranged irrespective of the magnetic environment they are in, we see in figure 1.6 a. that these spins are arranged randomly. When a paramagnetic material is subjected to an external magnetic field the spins largely align parallel to the direction

1.1. Unique Properties of Nanoparticles: the Importance of Surface vs. Bulk Atoms 11

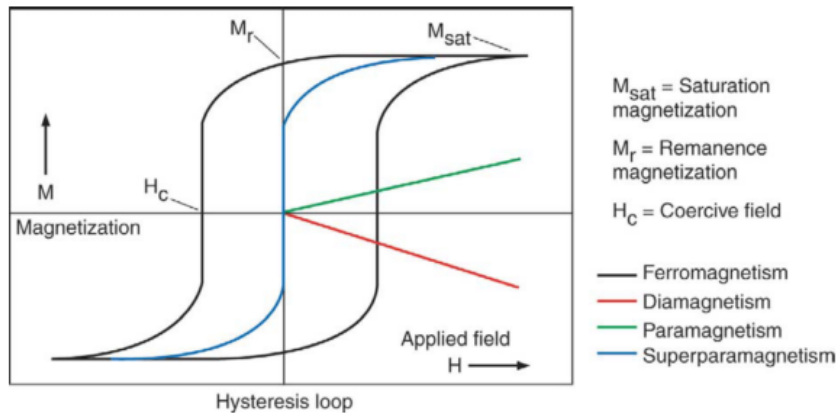


FIGURE 1.7: Hysteresis loops, or magnetisation vs. applied magnetic field plots, of the labelled magnetic classes⁴

of the external field, however the spins do not align uniformly. This results in a slight magnetisation as presented in figure 1.7.

Ferrimagnetism has been given its name derived from ferrite materials,^{44,45} where two lattice sites A and B are occupied by often differing magnetic ions. The spins in the A sites are aligned in one direction, while the spins in the B sites are aligned in the opposite direction but with differing magnitude as demonstrated in figure 1.6 b. The net result of this is magnetisation in a certain direction. As temperature is increased thermal energy agitates the spins, until a point called the Curie temperature, where the spins become randomly aligned and as such the materials spontaneous magnetisation is abolished.

Antiferromagnetic materials have opposing spin arrangements of equal magnitudes seen in figure 1.6 c., and so at low temperatures below the Néel temperature when an external magnetic field is applied the opposing spins are maintained by the influence of a strong negative interaction preventing the spins from aligning. At higher temperatures above the Néel temperature the spins can become randomly aligned and as such as temperature increases further, the magnetic susceptibility of the material decreases as the spins become more agitated.⁴⁴

In the context of Ferromagnetism; magnetic spins are perfectly aligned in respect to one

another by a strong positive interactive force acting between each spin and shown in figure 1.6 d. This results in the material having a spontaneous magnetisation which is temperature dependant, where as temperature increases the arrangement of the spins is agitated by the increase of thermal energy. At a limit called the Curie point the magnetic susceptibility of the material increases linearly with the temperature increase. Although Ferromagnetic spins result in a spontaneous magnetisation, in reality when a bulk sample of a Ferromagnetic material is examined it usually exhibits a zero magnetic moment. This is due to the bulk sample being divided into smaller magnetic domains which have a spontaneous magnetic moment, and will exist in opposite directions to those around themselves, reducing the net magnetic moment of the whole bulk to zero.⁴⁴ The bulk material can then be subjected to an external magnetic field, and the resultant magnetisation taken from zero to the value of the materials spontaneous magnetisation as the material becomes saturated (M_{sat} in figure 1.7) and the many interior domains align.

Another magnetic class is encountered when materials are shrunk down to dimensions of tens of nanometers: superparamagnetism. This is down to the isolation of the magnetic domains present in the material to possibly just a single domain. When we see just a single magnetic domain present in a particle there is no possibility of internal domains switching to align with an external field and magnetic saturation of the material occurring. Due to the lack of saturation possible in the material no hysteresis curve is observed, as presented in figure 1.7 where after an external field has been applied, the magnetisation returns to 0 once the external field is removed.^{4,46} Conversely as seen in other magnetic classes where as thermal energy increases to the Curie point and causes spontaneous fluctuations in magnetic spins,³⁹ in superparamagnetic materials as the thermal energy is increased the whole domain can fluctuate its direction, however maintaining alignment of its internal spins.⁴

Changes in magnetic anisotropy energy can also be observed to be linked to the size of the particle in question, this factor is described as the difference in energy between the particle being aligned with an external field in its minimum energy state or “easy axis”, to the particle positioned at its highest energy position in respect to the external field: “hard axis”.¹

1.2 Magneto-optic Theory

There is an increasing interest in the area of magneto-optic biodiagnostic systems as a homogeneous test for a variety of biomarkers, as a homogeneous system eliminates the need for sample preparation and processing prior to read-out of results. This is highly important for a Point of Contact (PoC) system that aims to reduce the amount of time required to detect and diagnose, and to reduce the burden of cost, maintenance and training.^{47–51}

There is several physical phenomena that involve the dispersion of elongated particles in a fluid and their manipulations of light passing through the colloid, causing birefringence which can be subject to the external magnetic field and following alignment of the dispersed particles.⁵²

The Cotton Mouton effect is a long known physical optic effect, being discovered in 1907 by Aimé Cotton and Henri Mouton. The effect describes the birefringence properties of a gas present in a perpendicular magnetic field. As such the state and orientation of the external magnetic field will influence the optical state. It is the magnetic equivalent of the Kerr effect which is found due to changes in electronic environment.^{47,51–55}

The Cotton Mouton effect as related to our project involves elongated anisotropic particles being dispersed in a solution that is subjected to an external oscillating magnetic field, as monochromatic light is passed through the sample it is plane polarised according to the alignment of the particles to the external magnetic field. This polarisation of light can easily be detected by sensor placed in the path of the light exiting the sample solution. This property can be explored at many points around a full cycle of a rotating magnetic field allowing for real-time analysis of any changes in the liquid. As the external magnetic field is rotated around the specimen sample the reporter particles in the sample will rotate following the plane of the magnetic field but with a slight delay called the phase lag.^{5,48}

The phase lag described here is caused by the high-aspect ratio particles not being able to move unhindered in the sample solution. It can be understood that if the particles were to be suspended in a vacuum and subjected to the same external magnetic field that

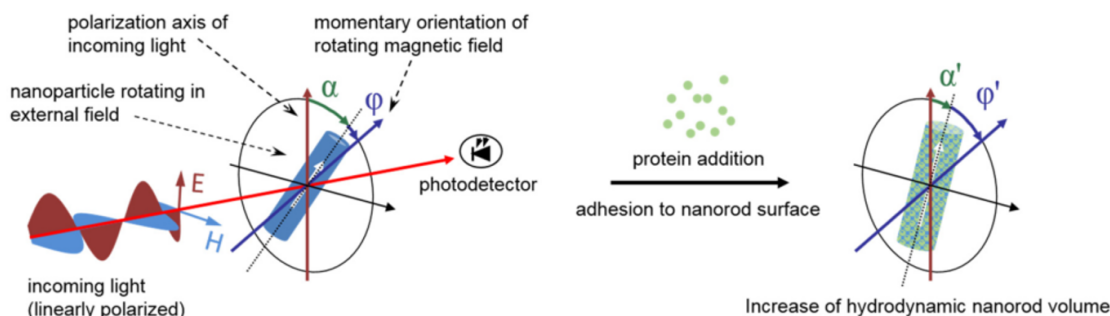


FIGURE 1.8: Diagram demonstrating the principle of this biodiagnostic system with anisotropic magnetic reporter particle, upon protein binding to reporter particle sees an increase in hydrodynamic area and hence phase lag⁵

there would be no or minimal phase lag detected as the particles could rotate exactly in plane with the magnetic field, with no drag or friction to cause the particles to rotate slightly behind the plane of the magnetic field. As such it is apparent that when these particles are suspended in solution, there is a drag or friction energy from the liquid working against the rotation of the elongated particles. From this we can establish that the larger the hydrodynamic area of the particle in the plane of rotation, the greater the drag force will be and hence a larger phase lag (ϕ , figure 1.8) will be found.^{5,49,54,56–58} This property also points to one method of multiplexing the analytical properties of the system as if you have more than one population of particles that are sufficiently different in size, the difference between their individual phase lags may be large enough to differentiate between the populations.

This phase lag generated here by the reporter particles binding to the analyte molecules results in an increase in Brownian relaxation time.⁴⁸ This provides a useful property for use in biodiagnostic systems: elongated magnetic reporter particles functionalised with specified proteins, anti-gens and anti-bodies can be mixed with liquid samples which may contain the desired target molecules/particles. Upon these target molecules binding to the reporter particle an increase in the phase lag can be detected in the output polarised light, caused by an increase in overall hydrodynamic size and mass of the reporter particle and hence an increased drag when rotating in solution,^{5,49,56} and is shown in figure 1.8. This observed overall phase lag increase will be minute upon one

reporter successfully binding to one target molecule, but as more reporter particles bind to their target molecules the phase lag will become more noticeable. As such not only the presence of a certain molecule can be detected, but also estimates of quantity and concentration of the target molecule can be made after process calibration.

Another benefit of using this Cotton Mouton effect to underpin biodiagnostic systems allows for interrogations of multiple reporter particles in one sample by tuning the optical response of the repeater particles so that multiple bands or wavelengths of monochromatic light can be used and detected independently in one system. This will allow for multiplexing of the system so that one liquid sample can be tested for multiple target molecules simultaneously.

The optical properties of an anisotropically shaped nanoparticle can be altered subtly and scalably by a couple of routes. Primarily the optical resonance of a particle is down to its inherent elemental properties, such as gold and silver. But over a few decades many publications have pointed to the size of particles and their direct effect on the optical properties, especially in the nanometer scheme it is found that the size and morphologies of the particles have great influence.^{35,36,38-40} This is mainly thanks to changes in availability of free conduction electrons resulting in a LSPR, as the particles are extended anisotropically in one direction the LSPR develops two modes; both a longitudinal and transversal mode are found.^{36,38,41,59} This property of nanoparticles allows the optical property to be directly changed by altering the length or width of the particle, and as such different length reporter particles could plausibly be used in one sample for detection of multiple analytes simultaneously. As the length of the nanoparticle is increased the longitudinal mode resonance tends to get further red shifted from the initial resonance of a sphere of the same material. Another way of altering the optical resonance of the reporter particle is to change the material that is being used for the optical function, either by replacing with a similar behaving material or to alloy or mix with a similar material; one good example of this is alloying gold with silver or copper.

The benefit of using the optical properties of the reporter particles to study the sample over the average magnetic properties of reporter particles in solution allows for sensing of multiple analytes in one sample, and should also mean that a lower concentration of the

reporter particles themselves are required owing to more sensitive optical responses to change.⁴⁸ This reduction in total number of reporter particles in the sample also allows for a lower limit of detection of the analyte present in the sample, aiding in diagnosis.

These anisotropically shaped nanoparticles inherent in their structure results also in a magnetic anisotropy, showing a clear directional dependence of their magnetic properties. This involves the magnetic moment of the particles tending to align to an easy axis, which will be the most energetically favourable direction of spontaneous magnetization. This magnetic anisotropy is what describes the alignment of the nanorice particles described above to an externally applied magnetic field, as in absence of this external field the particles dispersed in the liquid should be randomly orientated and of no long range order. This property allows for the analytical set-up to run on pulsed magnetic fields or rotating fields, both being able to show phase lag and as such binding events of reporter particles to analytes.

This process first found direct practical use in a PoC bio-diagnosis machine developed to indicate the presence of malaria in blood samples, this particular system used a rotating magnetic field external to the collected blood sample to align goethite nanorods, which are formed as a by-product in blood plasma by the malaria virus.^{47,51,60} These goethite nanorods take the chemical form of α -FeOOH and are thought to have antiferromagnetic properties, and so can be detected in this system the same way that is described above for designed anisotropic magnetic nanorods; as when aligned by the rotating external magnetic field a phase lag is seen in the observed light that is passed through the sample.

1.3 Crystal Growth

Crystal growth in solutions is often a balance of many factors, where from solvated precursor compounds particle seeds nucleate, grow by addition into clusters and then mature into defined structural forms.¹⁹ The route by which each crystal synthesis proceeds will differ but is often a midway between kinetic and thermodynamic forces.^{16,21,41}

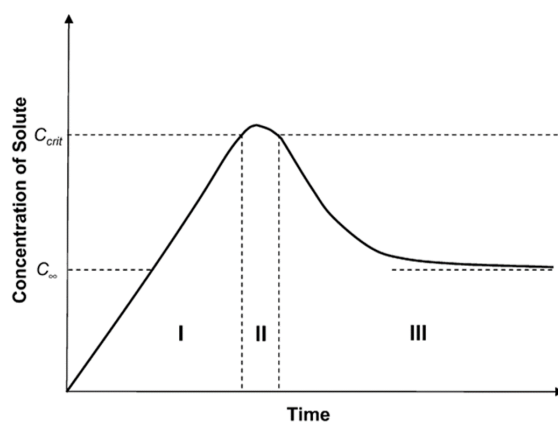


FIGURE 1.9: Graphical representation of the LaMer model of nucleation, where C_{∞} and C_{crit} indicate the equilibrium concentrations of the bulk material and critical concentration for nucleation from solution respectively⁶

In the case of metallic nanocrystals grown in solution, a metal precursor such as metal halide, nitrate, acetate etc. is dissolved in an appropriate solvent. To this precursor solution a reducing agent is added, or in some cases just heat is applied. At any rate, something is done to initiate the reaction.³⁷ The LaMer model has been adopted as the principle theoretical explanation for nanoparticle nucleation from precursor reagents in solution and is described as the following and demonstrated as a plot in figure 1.9.^{6,21,61–64} As metal ions are liberated from the precursor compound, their concentration in the solution increases (phase I, figure 1.9). The metal ion concentration increases to a crucial supersaturated point (C_{crit}) where that number of free metal ions can be no longer supported in the given solution volume (phase II, figure 1.9). At this supersaturation limit metal ions overcome the repulsive electrostatic forces (being positively charged) to nucleate and form very small clusters or seeds. Often large numbers of seeds or clusters are formed when the supersaturation limit is broken, resulting in a steep reduction in the concentration of metal ions in solution and no more nucleation occurs as concentration drops below the critical point (phase III, figure 1.9). It is on these formed seeds that further free metal ions form and agglomerate from solution, growing the seeds in size. When the particles become of a certain size the materials form into their native lattice structures which hence directs the crystal growths into certain shapes and forms,

reflecting aspects of their crystal structure. It is at this point in a crystals' development that other outside variables can be used to direct the growth of the crystal to other forms.^{12,65,66}

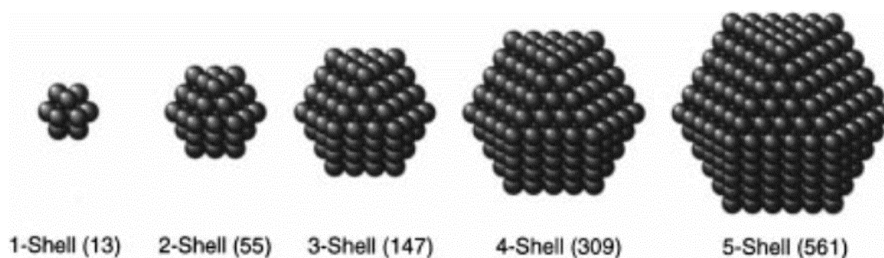


FIGURE 1.10: Diagram of nanoparticles of subsequent shells on one central atom, with labelled total atom numbers⁷

It is interesting that when particles are growing from these minute nucleating seeds that there exists certain “magic numbers” relating to the number of atoms present. These can be imagined starting from one central nucleus, that grows subsequent shells of atoms around it. These magic numbers to name a few are 13, 55, 147, 309, 561 and onwards and are shown in figure 1.10.⁷ Nanoparticles have been caught and observed at these sizes such as Au561, Au309 etc. and proves the process of addition by which these crystals grow.¹⁹

1.3.1 Capping agents / Surfactants

While controlled crystal growth can result in small nanoparticles of defined morphologies, the smaller the particles are the higher potential for agglomeration from solution can be. This is explained as the nanoparticles having a high relative surface area and hence surface energy, so to find a reduction in interfacial energy between solid and solvent the nanoparticles can often agglomerate into a larger mass and as such reduce the net interfacial area. To prevent this effect, the use of various surfactants or capping agents is common, and may be introduced for the purpose or are otherwise merely reaction by-products. These stabilisers can be found to either bond directly to nanoparticle surfaces, or protect the surface by the formation of charged electrical double layers where ionic

species in solution arrange themselves around nanoparticles carrying a slight charge themselves.^{67,68}

1.3.2 Structure Directing Agents

The use of structure directing agents or surfactants has become common in nanoparticle synthesis when certain morphologies or crystal faces of particles are desired,⁶¹ and are often dual use improving the dispersibility of the resulting particles as described above. These surfactants are present in solution and typically work through displaying some preference over which crystal faces of a material they will bind to, resulting in the further growth of the crystal along the least or un-protected faces.

1.4 Synthesis Processes

In the next few sections a brief overview of the synthesis processes and methods that have been used in this project will be given, where their history in the literature will be summarised, and secondly how they have found recent use and application in nanoparticle synthesis.

1.4.1 Forced Hydrolysis

Hydrolysis has been a term used in chemistry and related disciplines for a long time, deriving the meaning from greek “**hydro-**” for water, and “**lysis**” meaning to break or cut. So the term has been used to describe different processes; either unbinding of water molecules themselves, or to the breakdown of a larger particle by cutting it apart and water binding to one or both of the constituent parts, facilitating the division process by providing stable reaction products.

When applied to this project specifically the term “Forced Hydrolysis” represents the heating of an iron precursor compound solvent in water for varying time lengths, which through a slow process of hydrolysis the iron compound is broken down and various

$\text{Fe} x \text{H}_2\text{O}$ compounds are formed.^{69,70} These aquo compounds undergo further reduction resulting in several iron oxides and oxyhydroxides. The presence of phosphate and chloride ions in solution from added reagents forces the hydrolysis reaction to ultimately form hematite particles of a controlled morphology.^{71–73}

1.4.2 Noble Metal Coating

This process isn't necessarily known as a method in its own right, but the aim of the process can be met by a few routes and find common results. For certain applications of nanoparticles a noble metal coating over some other material is desired due to the hard wearing properties, novel optical and electrical properties, and inertness. This has been achieved in studies over the past few decades by physical deposition processes where films of metal are deposited at a precise thickness over a whole substrate via the gas phase, or via several wet chemical processes where a material is deposited or grown directly onto a particle dispersed in a solution or at phase boundaries.

In the research presented here the coating steps typically proceeded by an initial seeding step, with then further deposition of noble metals on to the seeds resulting in a noble metal coating on a differing material core. We also found that adequate coats could be attained without a seeding step, where noble metals were deposited directly onto functionalised cores.

1.4.3 Digestive Ripening

Digestive ripening was first discussed in the late 1990s with the work of Klaubunde et al. looking to use the process to tune the size dispersions of the nanoparticles being produced.^{10,74–77} The issue to be solved was that many solution processes for synthesising nanoparticles were resulting in particles of several sizes being made concurrently. Digestive ripening allows, via the use of many possible digestive ripening agents,^{78–82} more monodisperse populations of nanoparticles to be attained. The process also showed its applicability to producing alloyed nanoparticles of two or more metals.^{83–86} A digestive ripening agent is able to first bind and then scavenge metal clusters from the largest

particles in solution, and then adds these clusters to the smallest particles in solution resulting in growth. This has the effect of narrowing the size distribution of particles in solution until a near monodisperse population is attained. The process proceeds in contradiction to the more well studied Ostwald ripening process, which describes the free energy driven aggregation of the smallest particles in solution resulting in larger and fewer particles; typically which are monodisperse also.⁸⁷

For this research the digestive ripening process was used to try and produce more uniform coatings of noble metals on a core, due to starting with more uniform and monodisperse particles, and by which to give an alloyed metal coat.

1.4.4 Interface Coating

The interface between two liquid phases or a gas and liquid phase has in recent years found increasing use for synthesising nanoparticles as thin films, or as a system by which to isolate and trap the particles when formed. The interface of air and a liquid can support many types of particles and as the film present at the interface is compressed we can produce large amounts of the material, in a technique known as Langmuir-Blodgett films.^{88,89} Similarly the interface of two immiscible liquids can trap solid particles and has been used to produce thin films of particles, via reaction of precursor compounds.^{90,91}

In these studies the process of forming metallic nanoparticles at the interface of two liquids was applied to again attempt to form a noble metal coating on a nanoparticle core.

1.4.5 Polyol Reduction

The Polyol process is a novel synthesis that has been used to make metals, their oxides and various other compounds. The process was first discussed in the late 1980s, primarily in the work of Fievet et. al. where they identified its potential in producing “finely divided” metal particles.⁹²⁻⁹⁴ This process is different in that using an organic solvent: a polyol, which itself or its decomposition products reduce the precursor compounds. The

use of these organic solvents also allows for reactions to be run at higher temperatures without the use of expensive equipment due to the higher boiling points.

The Polyol process has been shown to be capable of producing highly monodisperse and shape-controlled nanoparticles,⁹⁴ particularly with the case of silver nanowires,⁹⁵ when a surfactant is introduced to the reaction conditions. During this research it was attempted to simultaneously produce silver nanowires with a nickel constituent, providing for both the magnetic and optical properties required in the research brief.

1.4.6 Hydrogenation Reduction

The reduction of compounds by hydrogen gas has been well known for a long time. The use of hydrogen as reducing agent allows for non-aqueous environments to be studied, as such oxygen or water sensitive materials can be produced. In recent years publications have shown that reduction of cobalt precursors by hydrogen gas, with the presence of a surfactant can produce precisely controlled cobalt nanorods or other nanoparticles.^{96–99}

Briefly this process of producing cobalt nanorods via hydrogenation reaction has been looked into; as to whether alternative cobalt precursors could effectively be used, and to test the effect of greater amount of surfactants within the reaction on the particulate product morphology.

1.4.7 Pickering Emulsions

The general term of *emulsion* refers to a mix of two immiscible liquids, containing droplets of an opposing phase in the other, stabilised by some surfactant. Typically emulsion surfactants are large molecules usually with opposing functional ends; where a “head” is hydrophilic and a “tail” is lipophilic, as presented in the left hand diagram in figure 1.11. Pickering emulsions differ in that a solid particle acts as the surfactant to stabilise these droplets in the opposing phase.^{8,100} A Pickering emulsion is seen in the right hand schematic of figure 1.11.

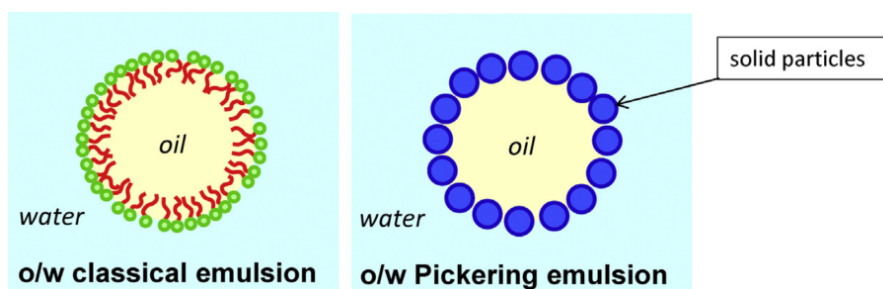


FIGURE 1.11: Schematic comparing emulsions stabilised with molecular and solid particulate surfactants⁸

A short time in the project was spent exploring the possibility of synthesising gold and silver nanoparticles in-situ of producing a Pickering emulsion stabilised by the same nanoparticles. By adapting a method of synthesising nanoparticles at the interface of toluene and water, their long-term stability at the interface allows for their application as a surfactant in making Pickering emulsions.

1.5 Biphasic Fluid Interfaces

The interface of two immiscible liquids is an interesting system to consider when discussing nanoparticle synthesis or processing.^{101–104} This system underpins the idea behind the synthesis processes outlined in the previous subsections 1.4.4 and 1.4.7. It can briefly be explained by the presence of an interfacial tension between two liquids that will not mix, a simple example of this is how oil will sit on top of a volume of water along-side the presence of a meniscus between these two layers, just as we see between water and air which is similarly a phase interface. Particles can be seen to adsorb to the interface when certain criteria are met and a net reduction in the Gibbs interfacial energy is ensued;^{8,100,104,105} the mathematical justification for this is discussed further in chapters 6 and 9. The criteria for the adsorbing particles include size, cross-sectional area, wettability amongst others.

1.6 Analysis Techniques

A full suite of both commonly used techniques and more niche equipments have been used to characterise the particles produced over the duration of this project; the range of techniques available to us have allowed us to observe and measure their optical, morphological, magnetic, structural and chemical properties.

1.6.1 Electron Microscopy

Electron microscopy has had a huge impact on the research and study of nanoparticles, as it has allowed the researcher to observe the morphology and sizes of particles down to the nano and sub-nanoscale. These nm scale images are not possible to acquire using conventional optical microscopes and theory, this is down to the manipulation of light and hence the highest resolution of an optical microscope being of the order of the wavelength of light used. Optical microscopes use visible light radiation with wavelengths of several hundred nm and as such cannot be trained to features of a particle in just tens of nm or smaller.

Electron microscopes avoid this issue by; as the name suggests, using a beam of electrons to look at the sample, with two divergent types of electron microscopy arising from whether the image of the sample is built from transmitted electrons through the sample, or electrons collected from above the sample where the electron beam is incident from. To direct a collimated, accelerated beam of electrons at a sample the use of electromagnetic lenses are required, making use of the tiny magnetic moment of single electrons a series of electromagnets arranged in sequence can direct the beam of electrons and ensure they are moving in a controlled path.

All this could not have been possible without a series of inventions in the early 20th century, first came electromagnetic lenses in 1926 developed by Hans Busch. Ernst Ruska a physicist developed and built both the first prototype electron microscope and the first electron microscope to achieve resolution greater than an optical microscope in 1931 and 1933 respectively. Since then subtle changes have been made to result in greater resolution and applicability, but the theory and build of electron microscopes are

very much similar to Ruska's first instruments. The main changes in today's commercial and research microscopes are the source of electrons, number and configurations of electromagnets and filters, and modern digital sensors for image capture.

The two types of electron microscopy have inherent advantages and disadvantages when compared to each other and are better used for certain applications, such as need for high resolution, imaging of conductive material, or to minimize damage to delicate samples or to collect elemental mapping data.

SEM

Scanning Electron Microscopy or SEM is a method of electron microscopy where a focused electron beam is passed over a rectangular area of the sample to be imaged in a raster pattern. This is where the beam is traced across the width of the area, then moved down one line and back across the width of the area until the whole area has been covered. At each point or pixel at which the scanned beam passes over in the image area, a change is observed in energy between the incident electron beam and what is resulting from its interaction with the sample. This change is manifested as high-energy back scattered electrons, low-energy secondary electrons, heat, and also as x-ray emission, all of these energies provide information on the sample be it topography or composition. Typically back scattered or secondary electrons are detected and used to build up an image of the sample over the area scanned, building up an image with data gained from when the electron beam is focussed at each pixel of the image.

This interaction of the electron beam with the sample allows for SEM to make use of a by-product: x-ray emission, to build up an elemental map over the image scanned. This means that at each pixel a reading can be made of the x-ray emission from the sample and specific elements can be judged to be at this point. As the SEM output is an image of the interaction of the electron beam with the surface of a sample, thick and bulky samples can be imaged, at least showing topography or features of the surface of the sample.

SEM has lent itself well to being used to image cells, biological structures and in general samples of a more delicate nature. This is due to the process by which an image is compiled where the beam is focused and passed over the sample, due to this focusing of the beam a relatively low accelerating voltage is applied to the electron beam, resulting in less potential for damaging the sample. It is this property of relatively low electron energies required that mean that many table-top SEMs have been produced with reasonable imaging resolution.

TEM

Transmission Electron Microscopy or TEM is a form of electron microscopy which typically offers greater resolution than SEM. The principle difference in TEM to SEM is that the image built is from electrons that are transmitted through the sample. Due to TEM working on transmittance, only relatively thin or samples with good conductance can be imaged.

Images of the sample are created in a different manner to SEM also, where the incident electron beam is not focussed to a small point of the image area, rather it is a wider collimated electron beam whose focal point is matched to the surface of the sample. As the electron beam passes through the sample conductive materials transmit the greatest number of electrons, with denser or electrically insulating materials hindering the beam and at which point a snapshot is taken of the sample area from an advanced digital camera. In the past the transmitted electrons would be incident with a phosphorescent screen underneath the sample, which with greater electron density a brighter image would be attained. From this difference in numbers of transmitted electrons a picture is given of the sample.

An issue with TEM is that due to using a wider beam passing through a large area of the sample, higher accelerating voltages must be used so the potential to damage the sample is increased. It is then usual that a TEM will incorporate something like a field emission gun as the source of electrons with high energy.

Associated Techniques

STEM or Scanning Transmission Electron Microscopy incorporates both methods above, where typically an electron beam in a TEM will be focussed to a point and scanned in a raster pattern over the sample as in SEM. This allows for TEM equipments to function as an SEM and can hence be used for elemental mapping from x-ray emission, complementing the high resolution of the TEM electron source.

3D-topography is a process by which stacks of images taken typically in TEM but possibly in SEM, are layered atop each other resulting in a 3D visualisation of the sample. With the correct computer package it can allow the observer to get a feel for the full morphology of an individual particle and its positioning in space, rather than seeing just a slice through one plane of the particle.

EDX or Energy Dispersive X-ray spectroscopy can also be known by the acronyms EDS, XEDS and EDXA. This technique is a commonly used method added on to SEM and TEM equipments. EDX simply takes a reading of any x-ray radiation given off from the sample as the electron beam is incident on it, the resulting x-rays and their inherent energies are characteristic of certain elements. This means that sample composition can be evaluated or complete elemental maps can be made to overlay an image taken in SEM or STEM modes.

EELS or Electron Energy Loss Spectroscopy works by knowing that the beam of electrons present in an electron microscope is of a given narrow range of kinetic energies, as the beam is incident on the sample being imaged then a loss of energy is seen as the electrons interact with the atoms in the sample. This loss in energy can be measured and losses of certain energies can be assigned to certain interactions of an incident electron and the type of material being imaged. EELS and EDX are often used in conjunction with each other as through analysing EELS spectra oxidation state, chemical bonding and conduction band properties can be resolved. When both spectroscopies are used together a more complete picture of the samples' chemical properties can be given.

1.6.2 UV/Vis Spectroscopy

UV/Vis spectroscopy is a common type of analysis in a variety of chemical research and industries, due to its relative low instrument cost and ease of use. This technique works by passing light on the ultra-violet to visible range of wavelengths, that is typically from <200 nm to ~ 800 nm and above, with more modern instruments reporting up to the near-infrared wavelengths. A cuvette with the sample is placed in the path of the light, then a diffraction grating separates the wavelengths from the incident light where a CCD sensor records the image. The light that has passed through the sample cuvette is then compared to the incident light prior to passing through the sample, and any absorption of specific wavelengths by the samples is presented in the spectrograph.

Materials of different kinds are able to be studied by UV/Vis spectroscopy, where samples are for the most part solutions however it can be applied to solid and gas samples also. The development of UV/Vis spectroscopy first originated from the knowledge that certain vitamins strongly absorb UV light, and so the spectroscopy was first commercialised in the early 1940s to indicate levels of vitamin in a sample. The molar amount in solution would result in a certain absorbance signal in the spectroscopic data. UV/Vis spectroscopy can also give us information on certain compounds, as certain chemical bonds can resonate as such with matching wavelengths, with the potential for stimulation of electron and photon emission as-well. The theory of UV/Vis spectroscopy is underpinned by Beer-Lambert's law, which is summarised by the following equation 1.1, where absorbance (A) is the product of a molar attenuation coefficient (ϵ), concentration of sample (c), and the path length of light through the sample (l).

$$A = \epsilon c l \tag{1.1}$$

UV/Vis spectroscopy; most importantly for this work, has also found recent uses in studying colloids of nanoparticles of metals, as the LSPR of certain nanoparticles can equally show absorbance signals in the UV/Vis range. As light of certain wavelengths will resonate with the de-localised sets of electrons on the particle, and this is highly dependant on surface chemistry, size, morphology and more properties of the particle,

we can thus see some clear scaling effects of changes in the particle properties and the spectrograph. Beer-Lambert's law and Mie Theory allow for the calculation of spherical metal particle sizes from the absorption of UV/Vis light, and has been adapted for modelling of particles of different shapes and structures.

1.6.3 Powder X-ray Diffraction Crystallography

Powder x-ray diffraction crystallography is just one technique of using x-ray radiation to resolve the crystal structure of a material, amorphous materials or those without a long range order will not provide useful data from crystallography methods. Known as XRD, single crystal or powder samples can be analysed, and the theory on which the technique is based is Bragg's law which is presented in equation 1.2.

$$n\lambda = 2d\sin\theta \quad (1.2)$$

In basic terms an x-ray source is positioned next to the sample, the x-rays are tuned into a narrow beam incident onto the sample, the x-ray source is then moved through a range of positions relative to the sample surface for example from 10° through to 60° . At the same time as the x-ray source is moved so is the x-ray detector moved at the opposite side of the sample and at the same angle as the source respective to the sample.

The intensity of detected x-rays at the detector will depend on the crystal structure and the angle of incidence, meaning the crystal structure can be established from the data.

1.6.4 Raman Spectroscopy

This spectroscopic technique has been in practice since 1928, where the principle was first demonstrated by the Indian scientist Sir C. V. Raman by looking at organic liquids exposed to intense sunlight, and observing spectroscopic shifts in the light. The phenomenon studied by Raman spectroscopy was proposed theoretically earlier in 1923 by Adolf Smekal. The theory of this process is explained by the inelastic scattering of light by a compound, to which the shift in energy relates to rotations or vibrations of specific

bonds and lattice structures. The scattered light measured in Raman spectroscopy is in opposition to the Rayleigh scattering of light.

Raman spectroscopy can be used in complimentary fashion with other techniques such as infrared spectroscopy which demonstrates the presence of dipole moments in the analyte, whereas Raman spectroscopy demonstrates polarisability of the analytes' bonds. It has been a useful analysis technique for this work to characterise synthesised materials by comparing their spectra to other standard spectra found in the literature.

In practice these days a Raman spectrometer is typically attached to a microscope, with a monochromatic laser light source. The sample is placed under the microscope which is then focused on the surface of the sample, the laser light is passed through the microscope optics and is thus also focused on the sample. Scattered light is collected by a sensor somehow out of line with the incident laser light and the shift in the scattered light energy is plotted against intensity.

1.6.5 Thermo-gravimetric Analysis

This simple technique can provide some basic information about the sample material and using informed conjecture or theory further assumptions about the sample and its interactions can be made. It incorporates a high precision balance on which the sample is placed, which can then be heated to high temperatures (1500–2000°C). The analyser then continually weighs the sample as the heat is varied, usually at a constant rate. The material usually will lose some mass at certain temperatures which can be attributed to drying, loss of certain chemical groups or surfactants and other chemical events. The heating of the sample can be conducted under a variety of conditions such as different gas atmospheres, so chemical events such as oxidation can also be more accurately quantified.

1.6.6 Nuclear Magnetic Resonance Spectroscopy

This widely used spectroscopic facility (NMR) can help to qualify the molecular structure of compounds. Through the use of a large external magnetic field and a smaller near-field oscillating magnetic field, within the sample certain atoms can be observed, and

depending on their local environment their resonance with the oscillating field will vary. As such when resonance with certain frequencies are observed the molecular structure can be inferred. Each element to be studied is observed independently, and commonly when working with organic molecules ^1H and ^{13}C NMR is performed, as the difference in environment such as double bonds, functional groups with varying electromagnetic values will shift the resonances of the atoms.

1.6.7 Vibrating Sample Magnetometry

This material analysis technique is useful for measuring some magnetic properties of a material. It can show the user which class of magnetic materials the sample is from the output data by providing information on hysteresis, magnetic saturation point and the magnetic hardness of the sample.

The system works relatively simply by using an electromagnetic set-up where two poles are separated by a gap, in this gap the magnetic flux lines will flow from one pole to the other, fairly evenly right in the centre of the two poles. The sample under study is then placed in to the centre of this gap between the poles, where the sample holder is then vibrated sinusoidally. This movement of the sample will cut across the flux lines between the poles, this will result in an induced current in the electromagnet, proportional to the magnitude of magnetism in the sample. Data can be collected under a certain magnetic field, or the electromagnetic poles can be set to sweep through a range of magnetic fields, which will provide the hysteresis measurements and so on.

1.6.8 Magneto-optic Test Setup

Some data had been gained from a hand built prototype system, that was designed and built for testing the applicability of certain nanoparticle materials for use in the aimed biodiagnostic system. Important criteria for these reporter particles can be measured with this equipment such as phase lag, oscillation amplitude and values, with a variable external magnetic field placed around a sample cuvette holder.

1.7 Project Aims

Cotton Mouton Diagnostics Ltd. (sponsoring company) currently use an established protocol for producing size defined iron oxide nanoparticle cores, and to subsequently coat these cores with a shell of gold particulates. These composite core-shell particles are then functionalised with bio-active adducts, which can bind selectively to their complementary analyte marker. These nanoparticles perform as reporters in the system attaching directly to the targeted analytes in solution and by producing a readable signal through their diagnostic system: α -CMD. It is anticipated that through designing similar elongated particles of either a different size, or of different optical and magnetic properties that the biodiagnostic system's capabilities can be improved. By increasing the number of finite reporter particle populations which can be detected individually; the system can then be used to detect multiple analytes simultaneously. Additionally, these reporter particles can sense changes in solution such as viscosity changes through coagulation etc, and so if a synthesised particle could improve the sensitivity of the system for detecting changes in viscosity that would also be of benefit.

The particles prepared from the work of this project are expected to meet the requirements of the above mentioned biodiagnostic application and to be able to act as reporter particles within the system.

The aims of this project were: to synthesise anisotropically shaped nanoparticles, with control over both magnetic and optical characteristics. To this end we have systematically looked to tweak and control the two main properties of critical importance to the diagnostic system; to affect changes in these properties five separate syntheses have been explored. Two of such methods were endeavouring to provide alternative routes to coating the same core magnetic particles already used in the target diagnostic system, with gold and with silver, with a hope to control the surface density of the noble metal coating, hence shifting the optical response. A third process explored was to dope the core particles with different metals with the intention of influencing the magnetic properties of the core. The final two methods explored were started from scratch, attempting to build complete alternative reporter particle morphologies and constructs using more modern synthesis methods to the ones already employed.

In the following chapters it is hoped that to some extent it can be proven that each briefed aim has been met in some way, and that it is possible to develop controlled populations of nanoparticles, suited to use as reporter particles in such a diagnostic system with discreet optical and magnetic properties.

Chapter 2

Hematite Nanorice Core Synthesis

2.1 Introduction

The iron oxide cores used in the majority of this research project and studied by various other research groups globally, have been prepared following a method first published in 1984 by Ozaki et al.⁷³ who demonstrated a simple, well controlled route to producing well defined hematite nanoparticles, whose shape and size are controlled easily by reaction time and reactant concentration ratios.

2.2 Forced Hydrolysis Synthesis

The synthesis proceeds by a forced hydrolysis reaction, where the iron precursor is dissolved in a large quantity of high purity water which at high temperatures liberates the Fe^{3+} ion and forms a variety of iron oxides and iron oxy-hydroxides. Forced hydrolysis has been used as such to produce a wide variety of oxides and oxyhydroxides of metals from a range of origin precursors.^{71,72,106,107}

2.2.1 Original Published Method

The process originally described and developed by Ozaki et al. is a forced hydrolysis synthesis where aqueous solutions of FeCl_3 and NaH_2PO_4 are aged for 2 to 7 days at 100°C in a sealed reaction vessel.^{73,108} Depending on the ratio of iron precursor to phosphate, and the length of ageing, the aspect ratio is controlled of the resultant particles.^{73,108–112} Of all populations produced there is high control with very little deviation from the mean morphology found in each sample. There is a general transition of shape moving from slightly elongated spheres or truncated potato shapes, through to rice or spindle shapes via a much larger increase in the longest vector of the particle, relative to the increase in width.

2.2.2 Influence of Co-precipitating Agents

Some studies have explored the effect of various co-precipitating agents in this forced hydrolysis process.^{71,113} The most prominent publication of this is by Reeves and Mann,¹¹² where the addition of simple anions such as phosphate and sulfates result in complete iron oxide formation with preferred adsorption to certain crystal facets, whereas more complex organo-phosphate additives can result in favoured formation of oxy-hydroxy iron compounds with less selective binding of crystal facets hence less shape control. The effect of various anion binding to iron compounds is dependant on solution pH as detailed in the paper.¹¹²

In the case of phosphate as is used in our synthesis, it is not a specific binding of phosphate to certain iron compound crystal faces that is observed. However, the mono-disperse nature of the resulting particles can be explained by stereochemical and geometric properties of certain faces that encourage strong phosphate binding.^{110,112–114} Bi-dentate binding of phosphate can bridge two surface iron atoms by substituting two O^{2-} sites when the spacing is close to 2.5\AA which is the O-P-O distance in phosphate itself. We see that the faces of hematite parallel to the c-axis have a distance of 2.7\AA between surface O^{2-} atoms, meaning a relatively strong binding of phosphate is possible and further growth generally along the c-axis is observed. The distances of 2.5 and 2.7\AA do present a small mismatch and this can explain the presence of a rough surface and curvature seen in the resulting particles such as in figure 2.4; from this forced hydrolysis process when using phosphate as the structure-directing agent.

The paper further relates the reduced shape control from the use of sulphate rather than phosphate due to an increased mismatch in binding spacings, with the O-S-O distance being 2.4\AA which is a worse match to the 2.7\AA distance between surface O^{2-} atoms available on the parallel face to the c-axis of hematite lattice.^{112,113}

A publication by Hu et al. who were discussing a microwave induced hydrothermal decomposition of iron precursors in the presence of phosphate ions discussed further the structure directing affect.¹¹⁰ In their experimentation they similarly found, that with a key starting molar ratio of Fe^{3+} to PO_4^{3-} that spindle shaped hematite particles were produced. In their explanation of phosphate's role they discuss that from hematite's

lattice structure there is crystal faces that exhibit either singly or doubly coordinated surface hydroxyl groups, and that in the case of the doubly coordinated hydroxyl on the (001) face they probably prevent adsorption of phosphate to that face. This sits with other publication's assertion that the hematite is preferentially elongated along its c-axis.

In a more recent publication by Frandsen et al. a new crystal growth mechanism is proposed.¹¹⁵ The forced hydrolysis method from Matijevic et al.'s paper was duplicated and samples at several occasions were analysed by varied processes. They found that in the early stages of reaction, or up to 56 hours, the solid formed is solely; or mostly the akaganeite (β -FeOOH) phase of iron complex. At this stage the akaganeite crystals are present as rod shaped particles or loosely defined particulates varying between several nms up to 100 nm longest vector. After 56 hours reaction time an increasing presence of hematite is seen, at the expense of akaganeite.

The growth mechanism in this paper hypothesises that the akaganeite rod shapes crystallographically orient themselves into agglomerated structures. The akaganeite particles were seen to typically arrange on their (100) and (001) crystal faces, then when the agglomerated particles are of a large enough total size a favourable transition to hematite structure is seen.^{115,116} This agrees with the reduction of akaganeite's presence in solution as the presence of hematite increases, while allowing for the appearance of the final hematite nanorice particles to be that of a single crystal even often diffracting as so. Irregularities in the crystal structure and also the surface roughness of the final hematite particles also adds to the theory of the nanorice particles being formed from akaganeite sub-units which transition to hematite with further hydrolysis.

It has been noted in the past that phosphate is also able to strongly adsorb to akaganeite's surface usually as a bi-dentate form, as presented in figure 2.1.^{107,117} Due to the crystal structure of akaganeite the hydroxyl units on its surface which will be exchanged for phosphate adsorption are present as one, two and three co-ordinate configurations,^{107,118} meaning the preferential binding of phosphate to certain faces will again result in preferential growth in a certain direction, resulting in these nanorod shapes.

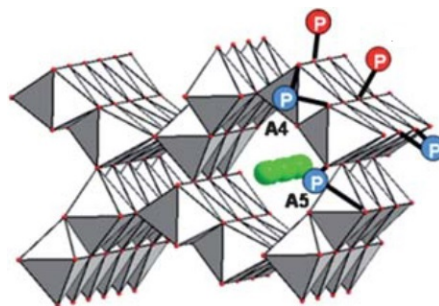


FIGURE 2.1: Crystal structure of akaganeite (β -FeOOH) showing preferential bi-dentate binding of phosphate (blue balls) over mono-dentate binding positions (red balls), green balls indicate position of chloride ions commonly found in akaganeite

The desorption of phosphates as smaller sub-units aggregate could be driven by the decrease in the reaction solution's pH as the hydrolysis mechanism proceeds.¹¹⁴ This then allows the primary sub-units to perform inter-particle sintering forming Fe-O-Fe bonds between the particulates.¹¹⁶ It has also been shown that heating the resulted particles up to 800°C we find a decreasing value of the c parameter of the observed crystal lattice by x-ray diffraction studies, from a value larger than which is observed for single crystal reference hematite sample, down to a value close to the reference value when heated to 800°C.¹¹⁶

2.3 Hematite Structure and Other Iron Oxide Phases

The hematite form of iron oxide and others have been highlighted as a desirable material from which to design magnetic nanoparticles for use in bio-diagnostic or for treatment purposes due to their relative stability in standard conditions along with typically being un-reactive.^{119–122} However some research does point to unexpected toxicity of specifically magnetic nanoparticles when used within the body, so for internal use these proposed particles should be subject to similarly stringent testing as for new drugs for example.^{123,124} This present cytotoxicity challenge can be met by further surface engineering or coating of the magnetic particles with a more suitable material.^{40,58,125}

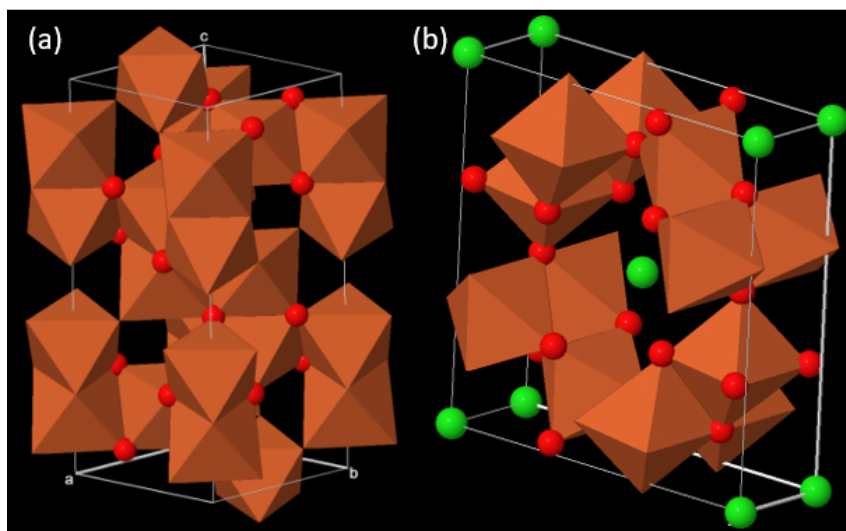


FIGURE 2.2: Crystal structures of: (a) hematite and (b) akagenite. Brown shapes represent iron valency, red balls; oxygen atoms and green balls; chloride ions

The structure of hematite has been resolved by various means as having a typical corundum structure as Al_2O_3 , assigned with the space group $R\bar{3}ch$. The unit cell is often computed with oxygen atoms forming a geometry of hexagonal close packed, with the iron atoms subsequently filling 2/3rds of the trigonally distorted octahedral interstitial spaces. From this it can be seen that each iron atom is valent to six oxygen atoms, three of which form an equilateral triangle above the iron atom as presented in figure 2.2. The other three oxygen atoms are arranged similarly in an equilateral triangle, which is staggered in respect to the opposing three oxygens, and this lower three oxygens are positioned relatively closer to the central iron atom and hence form a larger triangle arrangement with longer O-O distances.^{126–128}

Hematite in bulk is only ever weakly either antiferromagnetic below the Morin transition which is placed at 260 K, or slightly ferromagnetic between the Morin transition and Neel temperature at 960 K.^{44,120,128–132} However in the case of nanoparticles below a certain size, hematite tends to superparamagnetism.^{128,132–137} This is due to approaching the size at which a particle will take the form of a single magnetic domain which is actually

of a lower total energy than to be split into multiple magnetic domains, which is the approach we find of bulk magnetic materials to minimise contained magnetic tensions.

Akaganeite is a similarly important iron oxy-hydroxide phase in this study, in that it is an intermediate compound formed in the synthesis of hematite.¹¹⁵ Akaganeite is typically described as the β -FeOOH phase of iron oxy-hydroxide, in that oxygen and hydroxide groups are present, however chloride ions are known to be a common constituent of akaganeite.¹³⁸ Its structure is also presented in figure 2.2, where the unit cell falls into the monoclinic $I2/m$ crystal class. Iron in akaganeite is also arranged in an octahedral geometry, valent with 3 oxygen and 3 hydroxide groups. An interesting feature of the structure of akaganeite is large tunnels through the iron oxy-hydroxide structure which is where chloride or water ions are commonly found to reside, and so hydroxide groups are thought to mostly reside around the inside of these tunnels to balance charges.¹³⁸ Akaganeite is well known to be a very weak (negligible) magnetic material, but the classification of its magnetic properties are debated in the literature, with presented evidence of ferrimagnetic,¹³⁹ ferromagnetic, anti-ferromagnetism¹⁴⁰ and superparamagnetic¹³⁹ properties, with clear size and temperature effects on its properties.¹³⁹

2.4 Experimental

Following suite from more modern publications who also use the hematite nanorice core on which to deposit noble metals,^{59,111,116} we chose to use KH_2PO_4 as co-precipitation agent, as it was shown to act in an identical manner to NaH_2PO_4 resulting in morphologically controlled populations. The involvement of a small ratio of phosphates as a complexing agent, relative to the iron precursor, is stated to be integral to the development of the anisotropic shapes as the reaction proceeds.^{109,110}

The synthesis route used to produce all the hematite nanorice cores used throughout this project is as follows: A 50 mL aqueous solution of FeCl_3 (0.1622 g, 20 mM) and KH_2PO_4 (0.0027 g, 0.4 mM) is mixed in a fully sealed vessel, and aged at 100°C for 72 hours in a pre-heated oven. Over the duration of the ageing and heating process the solution transitions from an initial transparent rust-orange solution, deepening over 24 hours to a

dark brown, and finally the solution thickens to a deep opaque red solution. Following the 72 hours heating at 100°C the glassware is withdrawn from heating in the oven and left to cool to room temperature. When the vessel is able to be handled easily the contained deep red solution is subjected to ultrasonic bombardment in a water bath to disperse the solid precipitate, at which point the solution is quickly transferred into centrifuge tubes. The produced precipitate is then washed by repeating centrifuge regimes as detailed in table 2.1. After each centrifuge step the supernatant is decanted from the centrifuge tubes leaving behind a rust-red precipitate. Each eliminated supernatant should contain extraneous ions, un-reacted precursor and smaller particles. The remaining precipitate is then dispersed in fresh solvent by ultrasonic bombardment as prior, and subjected to the next centrifuge step. With each supernatant removed the colour of the supernatant transitions from a translucent orange to clear, indicating the amount of unwanted ions, particles and precursors is reduced. After the final centrifuge step the supernatant is removed and the dried precipitate is dispersed in 12.5 mL of fresh Industrial Methylated Spirits (IMS) for structural, spectroscopic and optical analysis, and for further use.

TABLE 2.1: Centrifuge washing regime followed with a centrifugal force of 2400 xg / 4500 xrpm

Solvent	Time (minutes)	Repetitions
Reaction solution	20	1
Deionised water	20	2
Industrial Methylated Spirits	20	2

2.4.1 Results and Discussion

The synthesis process used throughout this research was conducted only as described above, i.e. only hematite nanorice were precipitated after a heat treatment of 72 hours. And so the results presented below are obtained from that synthesis condition only and typically labelled as “72 hours”, unless stated otherwise.

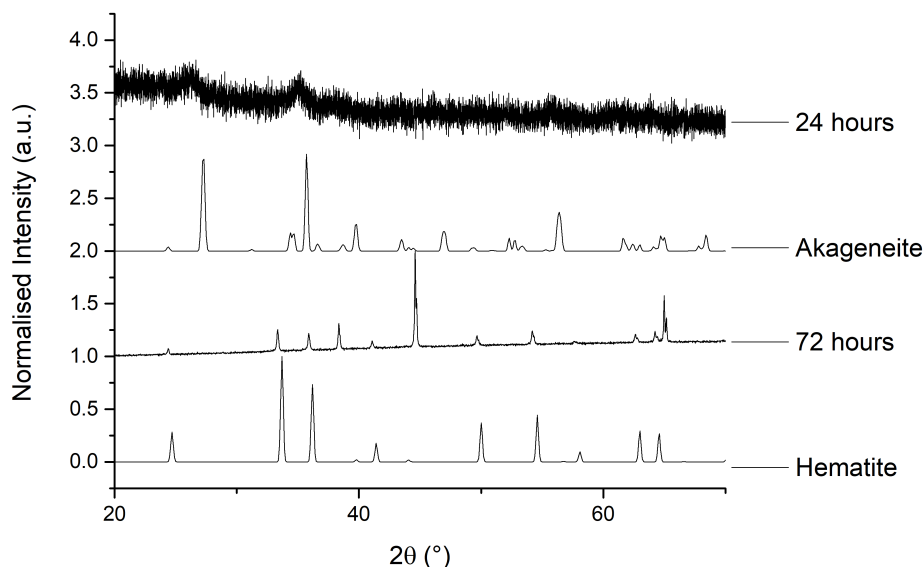


FIGURE 2.3: XRD plots of nanorice particles sampled at 24 and 72 hours of heating, and reference data of hematite and akaganeite

XRD

After centrifuge cleaning the red precipitate was dried in air at 80°C to a powder and analysed on a Philips X'Pert Powder X-Ray Diffractometer with a Cu K- α x-ray source with a wavelength of 1.541 Å. It was found that after 72 hours of heat treatment in solution the diffractogram of the precipitate strongly correlates with that of hematite (α -Fe₂O₃). We see this in figure 2.3 where peak position and heights of particles produced after 72 hours match those of standard data.^{115,126,127,141} Some additional peaks are observed here that are not present in standard hematite diffractograms with peaks at ≈ 38 and 44.5 and a group of peaks at around 65°, which can all be attributed possibly to remnant akaganeite or some lamellar structure; possibly surface bound phosphate.

A sample taken from solution after 24 hours of heating shows some similarities to standard akaganeite β -FeOOH data, which agrees with the mechanism of formation proposed

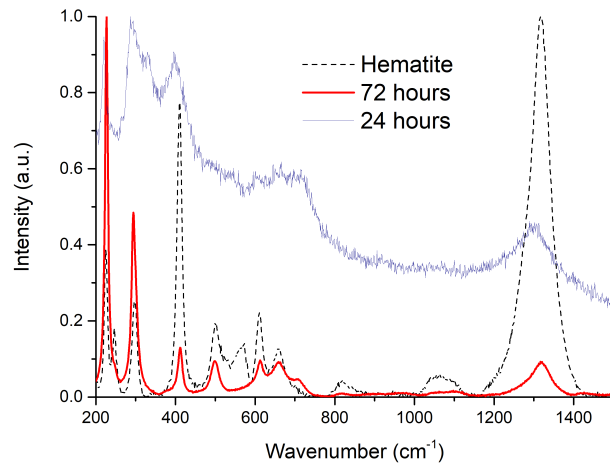


FIGURE 2.4: Raman spectroscopy data of samples prepared at 24 and 72 hours of heating, alongside a reference hematite spectra

by Frandsen et al.^{72,115} Although, the spectra as a whole in this case has given less intense peaks than the sample heated to 72 hours, indicating a less crystalline powder.

Raman

TABLE 2.2: Peak positions and phonon assignments of Raman spectra in figure 2.4

Raman shift position	Phonon assignment
227 cm^{-1}	A_{1g}
246 cm^{-1}	E_g
294 cm^{-1}	E_g
300 cm^{-1}	E_g
412 cm^{-1}	E_g
499 cm^{-1}	A_{1g}
612 cm^{-1}	E_g

Similarly prepared samples as studied by powder-XRD have been studied through a Model 1000 Renishaw Ramascope with a 633 nm laser source, attached to an Olympus

optical microscope. Agreeing with the XRD analysis we find that our nanorice particles produced after 72 hours of heating show strong correlation with standard Raman data of hematite.^{72,130,131,141–145} We can assign 7 typical peak positions of hematite in our data which is presented in table 2.2 with phonon assignments. The weak signals at 660 - 700 cm^{-1} have been described as lattice disorder in hematite in several studies,^{130,144} especially present in nanoparticles over bulk hematite samples.¹⁴⁶ However the samples produced from 24 hours of heating again shows some similarities with published Raman data of hematite, but with some additional peaks that can be attributed to akaganeite presence, seen at ≈ 310 and 730 cm^{-1} .¹⁴⁷ Overall the 24 hour sample has resulted in less intense raman peaks than the 72 hour sample which can be explained from the non-concise nature of the sample.

Some difference is observed when comparing our 72 hour heated sample to the hematite reference, as the reference data was attained using a 532 nm laser source. As the laser wavelength is changed we see the relative peak heights vary but the peaks stay largely at the same positions (wavenumber).

Electron Microscopy

Using various electron microscope techniques it was found that this synthesis is highly controlled in terms of morphology of the resulting particles and a narrow distribution of sizes.

By measuring a total of 593 individual particles seen on both the images below in figure 2.5; the distributions in length, width and aspect ratio of the particles were plotted and can be seen in figure 2.8. Over the total 593 particles measured, the average width, length and aspect ratio was found to be 112 nm, 564 nm and 5.07 respectively. The presence of some larger poorly shape defined particulates has had the effect of increasing the average particle widths while at the same time pulling down the average aspect ratio. Meanwhile the presence of some smaller observed particles also have decreased the average particle aspect ratio, length and width.

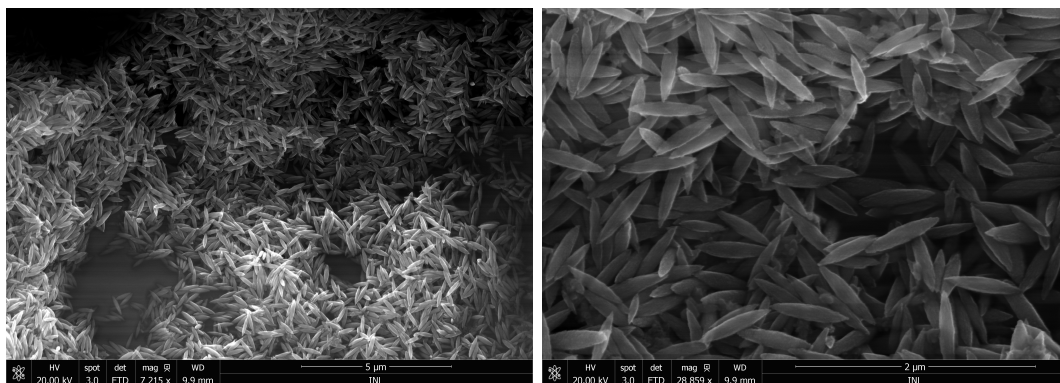


FIGURE 2.5: SEM images of hematite spindles resulting from 72 hours of 100°C heating in forced hydrolysis of FeCl_3 with KH_2PO_4

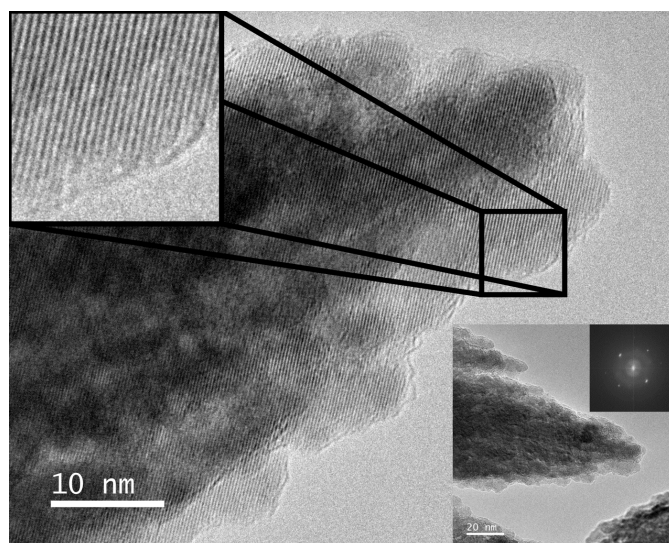


FIGURE 2.6: HRTEM images of hematite spindles resulting from 72 hours of 100°C heating in forced hydrolysis of FeCl_3 with KH_2PO_4 , with inset electron diffraction patterns and expanded lattice interference

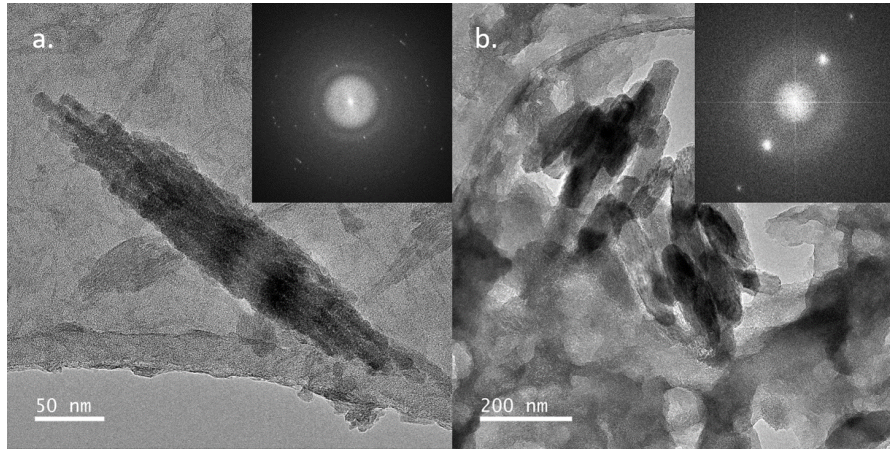


FIGURE 2.7: TEM images of precipitates at: image a. 24 hours, and image b. 48 hours of heating, with inset electron diffraction patterns

It must also be understood that due to the shape of the rice particles and the method of imaging, we have to consider improper length measurements due to the angled position the particle adopts in relation to the imaging plane. Due to the rice shape, the widest point can be assumed to be spherical, meaning that no matter the angle of the particle from $0 - 180^\circ$ relative to the image plane the width will remain the same. Conversely as a rice shaped particle rotates from $0 - 180^\circ$ relative to the image plane the length measurement taken will fluctuate almost sinusoidally from the true length - to the true width - back to the true length. It has been assumed that largely many particles will be present aligned with length axis of the particle in plane with the image, but any deviation from this will result in a decrease in the measured length, and as such the measured lengths will be skewed to a lower value.

The calculated interplanar distances of hematite as displayed in table 2.3 were arrived at through the use of equation 2.1, where the Miller Indices are assigned h, k, l , while a and c are lattice constants. The $R\bar{3}ch$ space group of the hexagonal unit cell of hematite requires the use of this equation, if the unit cell was cubic or tetragonal or other; a different equation would be required.

TABLE 2.3: Calculated interplanar distances of hematite lattice planes

Crystal structure	Lattice plane	Calculated interplanar distance
$\alpha\text{-Fe}_2\text{O}_3$, $R\bar{3}ch$	(112)	0.3689 nm
	(211)/(121)	0.1637 nm
	(011)/(101)	0.1133 nm
	(111)	0.2478 nm

$$\frac{1}{d_{hkl}^2} = \frac{4}{3} \left(\frac{h^2 + hk + k^2}{a^2} \right) + \frac{l^2}{c^2} \quad (2.1)$$

Through analysis of the inset electron diffraction pattern in figure 2.6 the (211)/(121), (011)/(101) and (111) lattice planes of hematite have been identified. The lattice spacings of such are seen to be 0.162, 0.123 and 0.247 nm accordingly. While the (112) plane of hematite has also been identified in another HRTEM image not presented here (included Appendix D.1), to be 0.365 nm. These are analogous to the calculated lattice spacings for hematite presented in table 2.3.

Thermo-gravimetric Analysis

The dried powder of samples produced after 72 hours have been analysed by Thermo-Gravimetric Analysis (TGA), and it was found to concur with auxiliary tests showing the particles to be the hematite ($\alpha\text{-Fe}_2\text{O}_3$) phase of iron oxide. This data is presented later in section 4.4.1, labelled as “bare core” in figure 4.5.

Vibrating Sample Magnetometry

Through the use of Vibrating Sample Magnetometry (VSM) the magnetic properties of our naked hematite core particles have been studied briefly, and were found to concur with properties that would be expected for hematite particles of several hundred nanometers, or bulk. That is that at room temperature we expect for hematite to be very weakly ferromagnetic with all spins aligned, being above the Morin transition temperature.¹³² Below the Morin transition hematite is known to go through a “spin-flop”

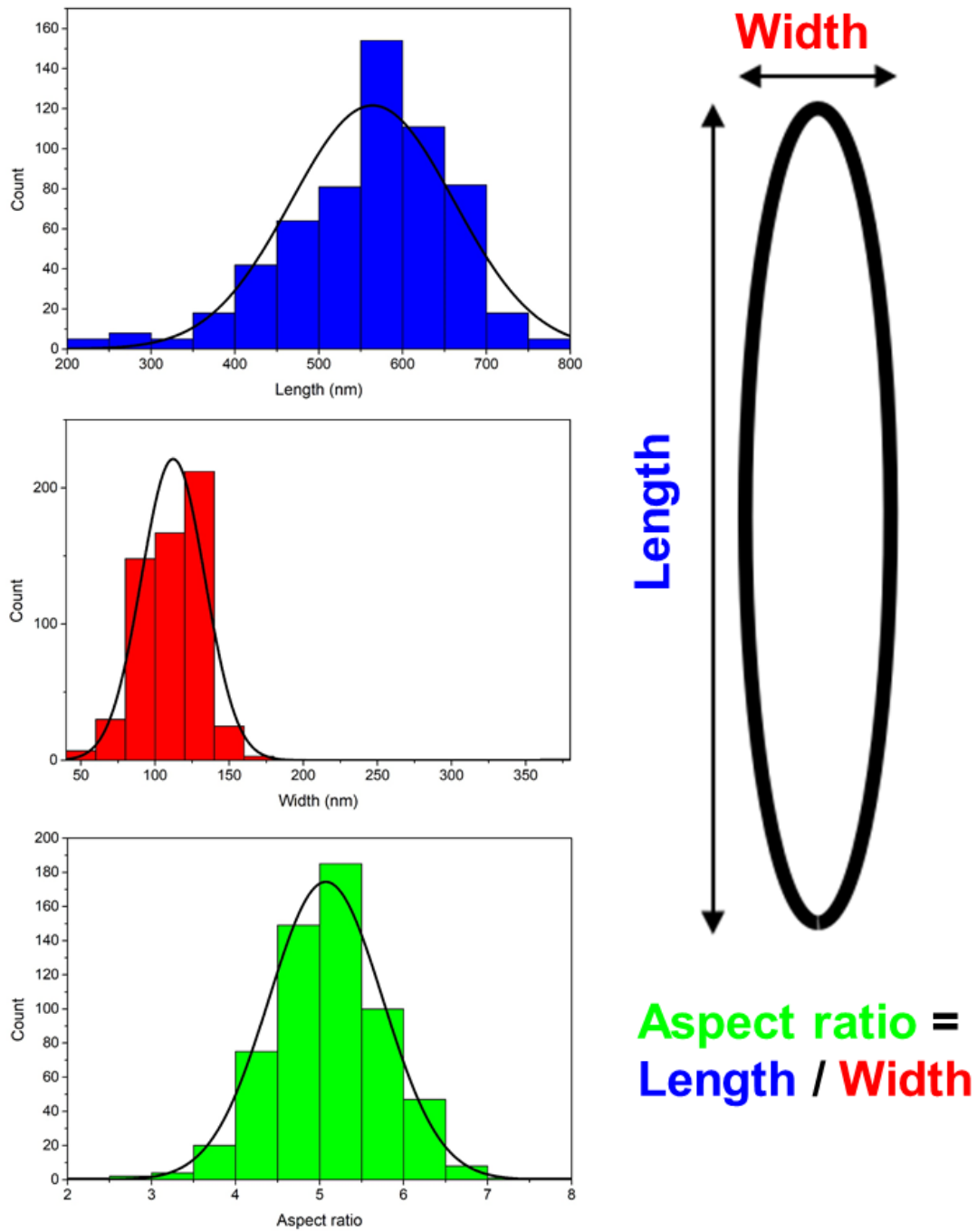


FIGURE 2.8: Histograms with fitted distribution curves compiled from measurements of 593 particles seen in figure 2.5

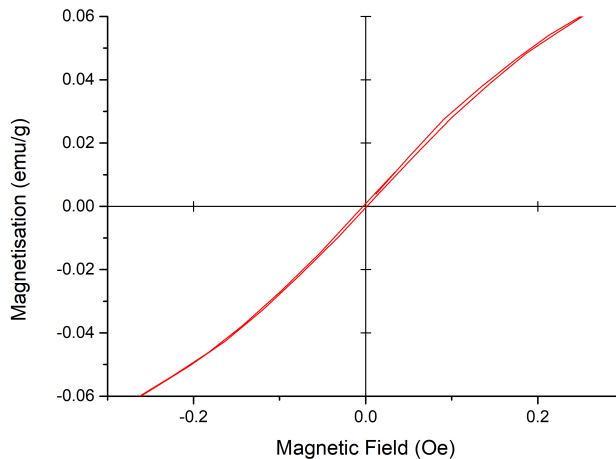


FIGURE 2.9: VSM of hematite nanorice formed after 72 hours of heating

transition 90° adjacent to the c-axis of the crystal structure and spins facing opposite directions in equal number, resulting in an antiferromagnetic property.

We see in the VSM data in figure 2.9 that indeed our particles are weakly ferromagnetic as the external magnetic field is varied from zero to positive, magnetisation of the particles increase to saturation as the relationship becomes less steep. As the field is reversed through zero and to negative values and back to zero, we see a symmetrical pattern emerge, with a very slight gap between the external field being either increased or decreased. This is due to magnetic hysteresis in the hematite particles resulting from the ferromagnetism, if the particles were of smaller size; <50 nm or so, there would be no hysteresis present in the cycle as the particles would be superparamagnetic, which would mean no remnant magnetisation when the external field is zero.

2.5 Conclusions

Through these varied studies we find after 72 hours heating of aqueous solutions of FeCl_3 and KH_2PO_4 at 100°C spindle or rice-grain shaped particles of $\alpha\text{-Fe}_2\text{O}_3$ with

little variation in size dimensions. We also found that after just 24 hours of heating an agreement with other studies whereby akaganeite is the primary phase present.^{115,148} Akaganeite has been noted in the past to be reliant on the presence of chloride ions to form which is the case in this synthesis upon decomposition of FeCl_3 .^{72,138,147} Chloride ions penetrate the iron oxy-hydroxide lattice resulting in the akaganeite structure as seen in figure 2.2, rather than resulting in formation of goethite or lepidocrocite (other phases of iron oxy-hydroxides). These smaller akaganeite rod particles or sub-units align along their long axis where with further aged heating the phase transition to hematite is undertaken. Electron microscopy studies have been able to image lattice interference patterns of the formed hematite nanorice after 72 hours for the first time, which appear as single crystalline particles, but are actually formed of smaller sub-units as described prior. The magnetic properties of these particles as a dried powder has also been introduced here, and characterised as weakly ferromagnetic, confirming assumptions.

Chapter 3

Doping of Hematite Core with Transition Metals

3.1 Introduction

As discussed in section 1.1.2, the magnetic properties of particles are something that can be seen to change when particles are of the nanometer regime, and when the morphologies and structure of the particles are altered.^{120,128,132–136,141,149} To meet the aim of this project of producing differing reporter particles for a biodiagnostic system we also aspired to influence the magnetic properties in some way; either a slight strengthening or weakening of the magnetic strength would be sufficient. While changing the magnetic class of the designed particle would not necessarily exclude them from application in this biodiagnostic system, the property of the particles was most important, with a low magnetic hysteresis being the most desirable property. It was however also important that the magnetic strength of the particle wasn't increased to too great an extent, as the application requires the particles to disperse easily in aqueous solutions for several minutes, and with minimal agglomeration.

In an attempt to manipulate the magnetic properties of our hematite core nanoparticles, we have explored the option of doping the hematite lattice with various transition metal ions. Doping of materials involves the insertion of an impurity element (dopant) which differs from any elements in the lattice in to which the dopant is being inserted.¹⁵⁰ The inserted dopant is typically in relatively low amounts in respect to the majority make-up of the material, so that small changes in the materials properties are affected; if the dopant was the majority constituent of the material the properties and hence our consideration of the material would be that of the dopant itself.

Doping of materials has been explored extensively to alter their electrical and optical properties, a ubiquitous example of this is for n-type and p-type semiconductors used in modern electronics and computer components. To highlight the relative low levels of dopant and use of the term "impurity",¹⁵⁰ in doping of semiconductor materials it is considered a high level of doping when there is one dopant atom per 10,000 atoms of the bulk material and low doping of one per 1,000,000 atoms. These dopants are introduced in order to influence a shift in band gaps of the material.

Use of hematite and its doping with various other metals has been explored over the last

10 years quite extensively for their efficacy as photoelectrodes and catalysts.^{151–154} The purpose of doping hematite with other metals is often to overcome the poor conductivity of hematite, while the implementation of different metal ions with higher carrier capability meanwhile limiting electron-hole recombination that is standard in the un-doped material.¹⁵³

Knowledge of the lattice structure of $\alpha\text{-Fe}_2\text{O}_3$ is important to understand its magnetic properties and how this can be influenced by doping with other metals. Hematite has only Fe^{3+} ions present in its lattice as opposed to other iron oxides which often have a combination of Fe^{3+} and Fe^{2+} ions due to iron's flexibility and stability in changes in its d-block electrons.¹²⁰

3.2 Doping to Influence Magnetism

The doping of a lattice with a minority dopant is also known to affect the magnetic properties of the resulting material, often in an greater magnitude relative to the dopants quantity in the material. This means that the alteration of the properties results not just from the intrinsic magnetic property of the dopant being present, but that the dopant alters the material on the whole to result in changed magnetic properties. This is manifested by not just an increase in; or diminishing of magnetic strength, but with changes between various magnetic classes occurring. Changes between magnetic classes ferments changes in hysteresis, blocking temperatures, saturation limits and remnant magnetisation, among others.

It has been shown in various publications that the magnetic properties of $\alpha\text{-Fe}_2\text{O}_3$ can be influenced by its doping with a variety of transition group metals.^{150,155–160}

3.3 Experimental

Our method of doping the hematite core particles involved a slight further modification of the method described in section 2.4. We elected to simply co-precipitate our transition

TABLE 3.1: Table of ionic radii¹⁴ discussed in this chapter

Ion species	Ionic radii (pm)	low spin / high spin
Fe ³⁺	69	ls
Fe ³⁺	78.5	hs
Co ³⁺	68.5	ls
Co ³⁺	75	hs
Co ²⁺	79	ls
Co ²⁺	88.5	hs
Ni ³⁺	74	ls
Ni ³⁺	70	hs
Ni ²⁺	83	hs
Cu ³⁺	68	ls
Cu ²⁺	91	-
Sn ²⁺	69	-

metals studied with the iron from their respective precursors in a one-pot synthesis route. Refer back to section 2.4 for the method of producing the hematite nanorice, and prior to heat treating the solutions we added calculated amounts of SnCl₂, CuCl₂, CoCl₂ · 6 H₂O and Ni(CH₃CO₂)₂ · 4 H₂O. The amounts of dopant precursor added was either calculated by percent weight fraction of the iron precursor used in the synthesis, or as a percent molar fraction of Fe³⁺ ions to dopant ions. The amount of doping is relatively much more than is discussed above in typical doping synthesis for electronic purposes with the maximum by weight fraction at 10%.

3.3.1 Results and Discussion

Using the various analytical means discussed below we have monitored the doping of α -Fe₂O₃ with cobalt, nickel and copper ions. Attempts to dope with tin ions was unsuccessful in this study. The ionic radii of the relevant ions are of importance when considering the effect the dopant will make upon the lattice it is being inserted into. Hematite (α -Fe₂O₃) is made up of only Fe³⁺ ions, and so the relative size of our dopant ions will cause the lattice to either contract or expand in some way. The dopants' ionic radii must also be closely matched to the origin ion it is substituting for, otherwise the

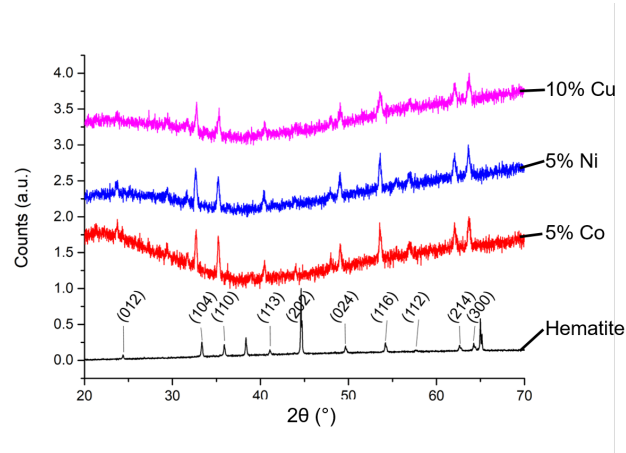


FIGURE 3.1: XRD plots of $\alpha\text{-Fe}_2\text{O}_3$ nanorice doped with 3 different transition metals: cobalt, nickel and copper. The bottom data plot is that of undoped $\alpha\text{-Fe}_2\text{O}_3$ nanorice particles, with labelled lattice indices

ion does not constitute as a favourable dopant. From table 3.1 we see the low spin Fe^{3+} ion has an ionic radii of 69 ppm, with Co^{3+} and Cu^{3+} ions in low spin showing very closely matched ionic radii both slightly smaller than the Fe^{3+} . Sn^{2+} does match very well with an ionic radii of 69 ppm, but is however the wrong oxidation state to substitute directly with Fe^{3+} . Conversely Ni^{3+} displays an ionic radii larger than Fe^{3+} both in low and high spin, and so may be more difficult to substitute into the lattice, likely causing an expansion of the cell volume.

XRD

Through the use of x-ray diffraction the doping of hematite nanorice cores with several transition metal ions of varying proportion is monitored. In all cases we see the ability of these metal ions to replace iron ions in the lattice structure of $\alpha\text{-Fe}_2\text{O}_3$ as we see mostly the same lattice peaks evident in the diffractograms in figure 3.1. The same additional peaks discussed in section 2.4.1 are present here, and can be neglected when considering the affect of doping. However, the presence of a shift in the peak positions

with incremental addition of the dopant ions, alongside a relative broadening of the peaks confirms the successful doping of the hematite lattice.

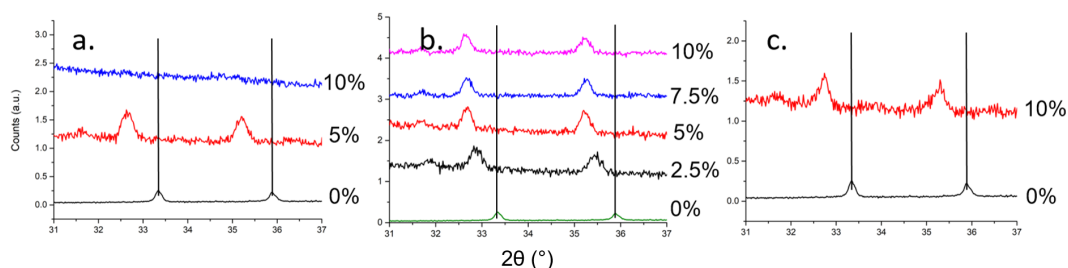


FIGURE 3.2: XRD plots focussed to 31–37° of particles doped with; nickel, cobalt and copper in images a., b. and c. respectively with increasing proportions of up to 10%

Nickel In the case of nickel doping, it is seen that the hematite structure is preserved when the dopant is present in 5% quantity seen best in figure 3.1. Per contra when the nickel dopant is increased up to 10% a very weak to no XRD signal is observed. In graph a. of figure 3.2 we can see the down shifted presence of peaks (104) and (110) in the 5% doped sample with no peaks for the 10% nickel doped sample. From this we can assume a very poorly crystalline sample, and that the doping of Nickel into hematite lattice has a low limit, possibly derived from Ni^{3+} having a less well matched ionic radii for doping of hematite, when compared to that of Co^{3+} and Cu^{3+} .

Cobalt Equally in the case of doping with cobalt, the hematite lattice structure is maintained. Moreover we again observe a similar down-shift of the peak positions as cobalt is incorporated. Seen in graph b. figure 3.2, the (104) and (110) lattice peaks shift increasingly as doping is increased, from 2.5 to 5%. It is to be noted that from 5 through 10% doped samples no further peak shift is observed, likely indicating that the potential of hematite to be doped with cobalt reaches saturation at the 5% condition.

Copper The doping of hematite nanorice with copper in this process has resulted in similar XRD data as the doping with nickel and cobalt discussed above. A down-shift is again observed as seen in figure 3.2, whereby a sample doped with 10% copper sees the (104) peak shift -0.6° and the (110) peak shift -0.6° also.

Raman

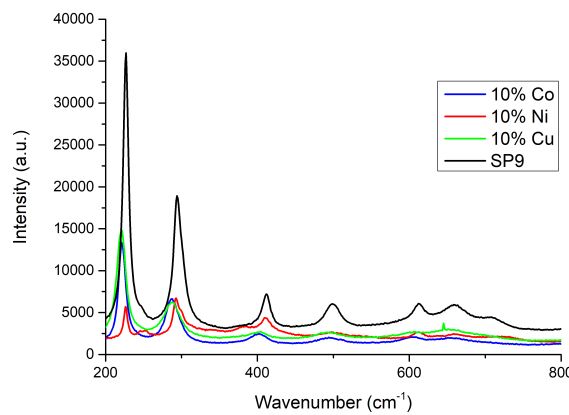


FIGURE 3.3: Raman spectra of hematite nanorice core, and 10% doping of cobalt, nickel and copper

Similarly to using XRD to monitor doping, we can observe changes in lattice structure due to doping with Raman spectroscopy. As is seen in figure 3.3 we see a significant down shift of peak positions for 10% doping with cobalt and copper while the general pattern for hematite is maintained. For example the first A_{1g} peak, seen in figure 3.4, placed at 227 cm^{-1} for our standard hematite particles is shifted to lower wavenumbers of 221 cm^{-1} for both samples doped with 10% doping with cobalt and copper. However, the sample doped with 10% nickel is placed slightly below that of hematite at 226 cm^{-1} . It is also of interest that a reasonably good Raman spectra of the 10% nickel doped sample is achieved matching a hematite lattice structure. However, this same sample did not result in a good XRD plot; this could be due to some sampling error in the XRD analysis, or, in addition, due to only a small yield of crystalline precipitate.

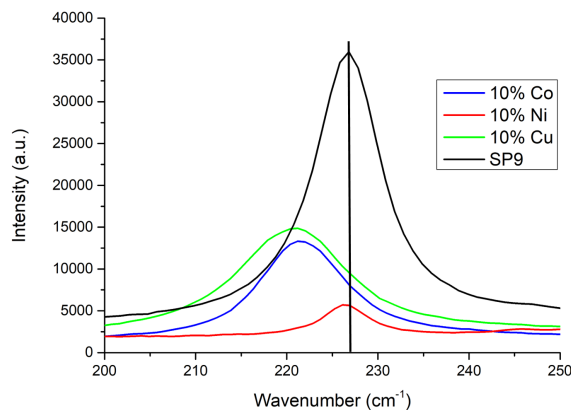


FIGURE 3.4: Raman spectra of hematite nanorice core (SP9 - prepared in chapter 2), and 10% doping of cobalt, nickel and copper, focussed on the A_{1g} peak between 200–250 cm^{-1}

Electron Microscopy

Through the use of electron microscope studies we have qualified that the doping of hematite with cobalt, copper and nickel ions has minimal affect on the overall morphology of the resultant particles. As these dopants have a similar ionic radii to Fe^{3+} species in hematite; only a small change of the lattice is resulting, and as such the controlled synthesis of nanorice morphologies with phosphate presence is maintained. This is demonstrated in figures 3.5 & 3.6, where electron micrographs show nanorice morphologies are maintained upon doping with cobalt and nickel.

However, it does seem that there is more size dispersity in the resulting particle: while the spindle shape is still evident among all particles seen; there is a larger variation in length of the particles when compared to the undoped hematite synthesis. This could point to unequal doping of particles, maybe the substitution of dopant ions into the hematite lattice does effect the lattice structure to such extent that further growth of the nanorice particles is hampered, and so some particles grow preferentially grow larger with pristine hematite structure.

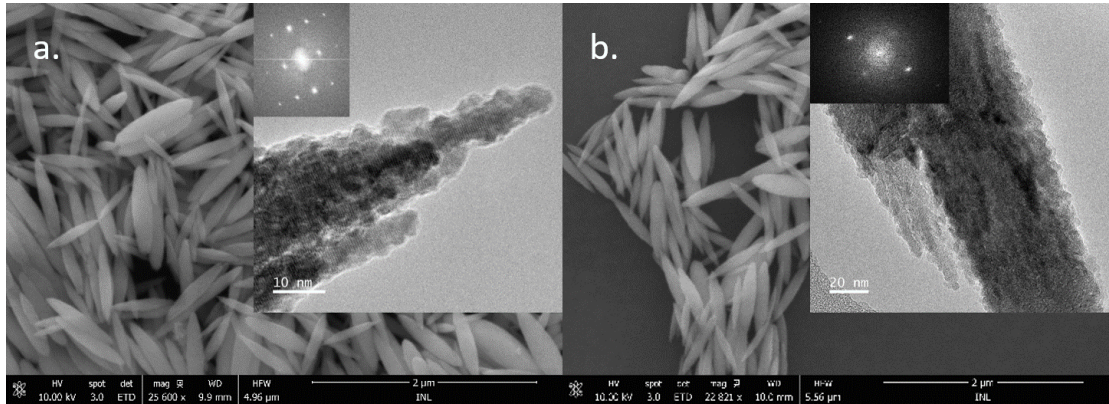


FIGURE 3.5: SEM and TEM images of nanorice particles doped with cobalt, image a. is of 5% cobalt and image b. 10% cobalt

The calculated interplanar distances of hematite presented in table 2.3 were then compared to the values attained through analysis of the electron diffraction patterns from HRTEM images. In general, the introduction of the dopants studied here resulted in smaller observed values of interplanar distances for the (111) and (112) lattice planes, a slight increase in (011)/(101) plane and no trend seen in the (211)/(121) plane. Overall with these observed interplanar distances decreasing upon doping, and with XRD data showing a lowering of peak positions; the insertion of low spin Co^{3+} and Cu^{3+} into hematite, as they are relatively smaller than Fe^{3+} , is resulting in a lattice contraction with the lattice slightly expanding along the (011) plane to compensate. The unequal interatomic distances of Fe-O atoms in hematite crystal structure will result in doping occurring preferentially at certain Fe sites, hence why we observe contraction of the lattice in certain planes for all dopants, even Ni^{3+} which is the only dopant ion to have a slightly larger ionic radii than Fe^{3+} .

In the case of doping with nickel, we noticed some difference not with the morphologies of the particles or their size, but how they arranged themselves in respect to others. The samples of 5% nickel doped hematite nanorice seen in figure 3.6 appear to show the particles closely packed together in clusters. This would agree with previous publications of nickel doped hematite increasing the magnetic strength of the particles,¹⁵⁶ resulting in the particles more likely to be agglomerated in solution. As such the closest packing of

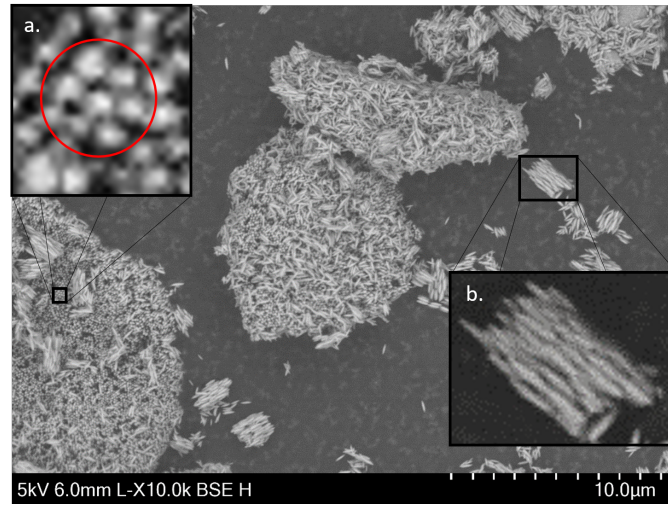


FIGURE 3.6: SEM image of 5% nickel doped hematite nanorice, with expanded areas of interest. Inset image a. shows the close packing arrangement of spindle particles, with inset image b. showing a cluster of these agglomerated particles along the opposing axis

the spindle shaped particles is of the shortest axis of the particle being closest together.

Magneto-optic System

Some of our doped hematite nanorice particles were studied in the magneto-optic test system at CMD Ltd. (the underpinning principles of the test have been described in section 1.2), where through variation of the external magnetic field oscillation frequency the reporter particles were subject to, and by varying the viscosity of the solution they are dispersed in, certain properties of the particles could be gleaned.

All doped samples presented in figure 3.7 indicate a larger amplitude of oscillation with the external magnetic field than sample IC50 with just an undoped hematite core (synthesis method described in section 6); both when particles are dispersed in just DI water and in a 25% /w glycerol solution. However, of the three doped samples analysed, the 10% cobalt sample has the largest amplitude over the whole frequency range studied.

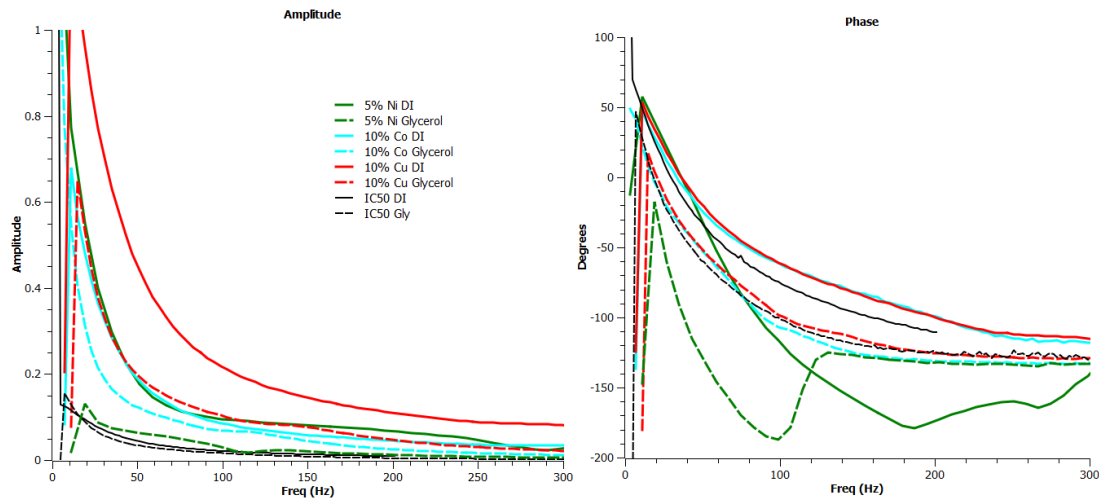


FIGURE 3.7: Plots of amplitude against frequency, and phase against frequency for nanorice particles doped with 5% nickel, 10% cobalt, 10% copper, and sample IC50 for reference (chapter 6)

These results could be linked to the fact that no shell-deposition method has been undertaken (when comparing to IC50) and so it is only the spindle shaped particles in solution providing a large amplitude of oscillation with no scattering from other dispersed particles. The phase against frequency plot is not as clear cut and so each sample is discussed below.

The sample with 5% nickel doping quickly sees a drop down in its phase value as frequency is increased, while the difference between these two curves when the particles are dispersed in DI water or 25% /w glycerol solution is markedly large in comparison to other prepared particles. The difference between these two curves at 50 Hz is 95.9° . For this reason the nickel doped particles have highlighted themselves as much more sensitive to changes in viscosity in solution, as it is around 4x more sensitive to viscosity changes than sample IC50 with an undoped hematite core. Some issues are seen with this data set when the values of phase go below -180° , as it is impossible for the system to resolve between 0 and 180° . The values of phase are seen to increase after reaching this minimum value of -180° in both samples in DI water and 25% /w glycerol solution, more work would have to be undertaken to study this phenomenon whether it is a bug

in the analysis technique, or an attribute of the doping with nickel.

The sample of 10% cobalt doping appears at closer values to undoped core particles than the nickel doped sample. At 50 Hz this difference is 28.2° which is very similar to the undoped hematite, however the difference between samples in DI water and 25% /w glycerol solution is greater at higher frequencies.

The sample of 10% copper doping appears very similar to 10% cobalt in the plot of phase against frequency, where the difference at 50 Hz between particles dispersed in DI water and 25% /w glycerol solution is 32° which is slightly larger than undoped hematite values. The difference doesn't however vary as much as frequency is increased, providing a more reliable sensitivity to viscosity changes over a range of frequencies.

3.4 Conclusions

To summarise, in this chapter the doping of hematite nanorice particles with cobalt, copper and nickel by a co-precipitation method has been explored. The previous process for forced hydrolysis of FeCl_3 in aqueous solutions was amended to add in portions of the dopant precursors, while maintaining all other variables such as reaction time, temperature and ratio of phosphate structure directing agent.

This adaption was shown to successfully produce still shape controlled particles of spindle morphology, while doping to a certain extent with these other metals. This doping was demonstrated by observed shifts in XRD and Raman data, while the general $\alpha\text{-Fe}_2\text{O}_3$ lattice structure was preserved. The behaviour of these doped particles was also observed to change when studied in the magneto-optic diagnostic system depending on the dopant metal, with significant increases in sensitivity to solution viscosity changes for doping with nickel. However much more detailed studies of the magnetic properties of the doped particles should be performed, through VSM, or more sophisticated and sensitive techniques.

Chapter 4

Noble Metal Coating

4.1 Introduction

As discussed in chapter 1 our produced particles must have a strong optical component to them, which is not significantly strong enough when using the hematite magnetic cores by themselves. To meet this requirement we have looked to coating our magnetic cores with noble metals; primarily with gold and silver. These metals as nanoparticles are renowned for their strong optical resonances that are intrinsically linked to the morphology and size of the particles, this is labelled in theory as an aspect of LSPR. This quality of nanoparticles has been covered in section 1.1.1.

This section covers the previous work completed in the area of seeded growth of noble metal shells on iron oxides and other core particles, and the various methods that can be used to perform this. In the results section the method used in this study to deposit gold and silver seeds on hematite nanorice cores is discussed.

4.2 Simulated Optical Resonances

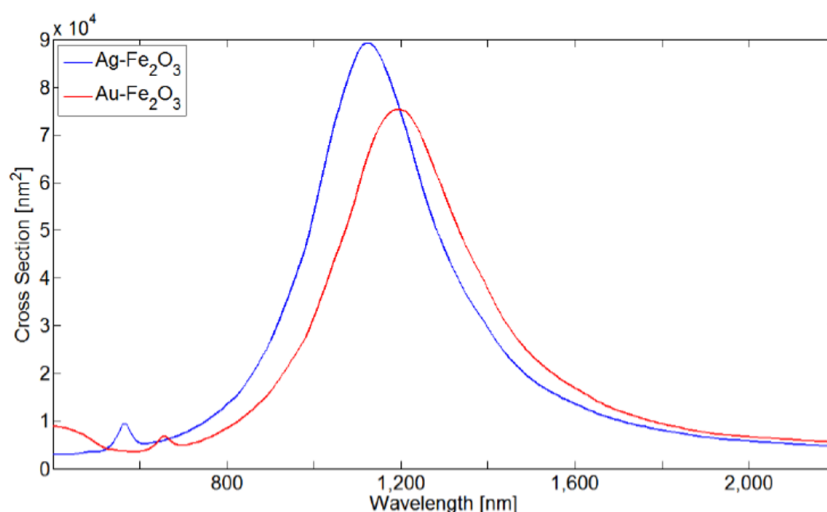


FIGURE 4.1: Graph showing simulated longitudinal resonance of α -Fe₂O₃ nanorice coated with 10 nm of either gold or silver

As a proof of concept it was found to be beneficial to simulate the optical resonant properties of the core-shell particles which were aimed to be produced through this process. The simulations presented in figure 4.1 were prepared in CST simulation software using a numerical full wave electromagnetic solver, the program used a Finite Difference Time Domain (FDTD) solution with a boundary size set to three times the particle radius. The solver wavelength ranged from 400 to 2500 nm measured using a discrete set of far-field monitors using a linear 10 nm step size to calculate the absorption, scattering and extinction co-efficient. The optical properties of gold and silver used in this simulation, namely the refractive index was taken from an experimental study.¹⁶¹ Setting up the simulation with similar parameters to another study,⁵⁹ the core rice shape was set to dimensions of our standard particle dimensions, which are detailed in section 2.4.1. Then in the case of our simulations, a 10 nm shell of gold and silver with their standard optical properties is formed around the whole core morphology.

The study by Wang et. al.⁵⁹ studied only the resonances of these core-shell morphologies with gold forming the shell layer. They saw that with increasing shell thickness a blue-shift of the longitudinal resonance was observed, moving to longer wavelengths progressively. The published method also was simulated using core particles with smaller dimensions than our standard core particles (340 nm x 54 nm), but with a relatively larger aspect ratio, at 6.3. The longitudinal resonance was demonstrated to be the much stronger resonance with incident light, as opposed to the transversal resonance, so we found it most relevant to simulate this response.

For our simulation of a gold coated core, the longitudinal resonance is blue-shifted in relation to the simulation in the previously mentioned publication, at 1,200 nm.⁵⁹ This is likely down to the increased length of our core particles being about 200 nm longer. We similarly observe a small resonance peak at about 650 nm which is attributed to a high order longitudinal plasmon mode.

This project has strived to coat the hematite core particles with both gold and silver and different compositions of such. In our simulations a clear blue-shift of resonance peak was observed when the shell was changed from gold to silver, positioned at 1,110 nm with a slightly more intense resonance than the gold coating.

It is planned that between these two longitudinal peaks of gold and silver coatings at 1,200 and 1,110 nm, we can incrementally scale between these two resonances by varying the composition of the shell between gold and silver.^{36,37} These simulated resonance peaks also fall within the near-infrared window of 650-1350 nm, which has minimal absorbance from water and blood in biological sample fluids. This is important to consider for the intended application.

The application of our reporter particles uses them dispersed in solution in a relatively low concentration, and so the influence of plasmonic particles in close proximity to each other or in an array can be neglected,¹⁶² meaning that the simulated optical properties of just one particle should be true to the intended application.

4.3 Published Methods to Formation of Metal Coats

The coating of hematite (and other iron oxides) particulates with noble metals has been the focus of intense research from various approaches; of which some are presented here.^{59,109,120,163–165}

4.3.1 Linker Group Functionalisation

Gold and silver are not able to directly complex or alloy with iron oxides, so the use of a linking group is required to combine these two components; magnetic and optical. This bridging function has fallen to several established routes, such as utilising organic compounds with known bonding to metals and oxide surfaces, or to an intermediate layer of another oxide material which can provide a surface layer which is easier to decorate with metals.¹²⁰ A few routes to this end are discussed below.

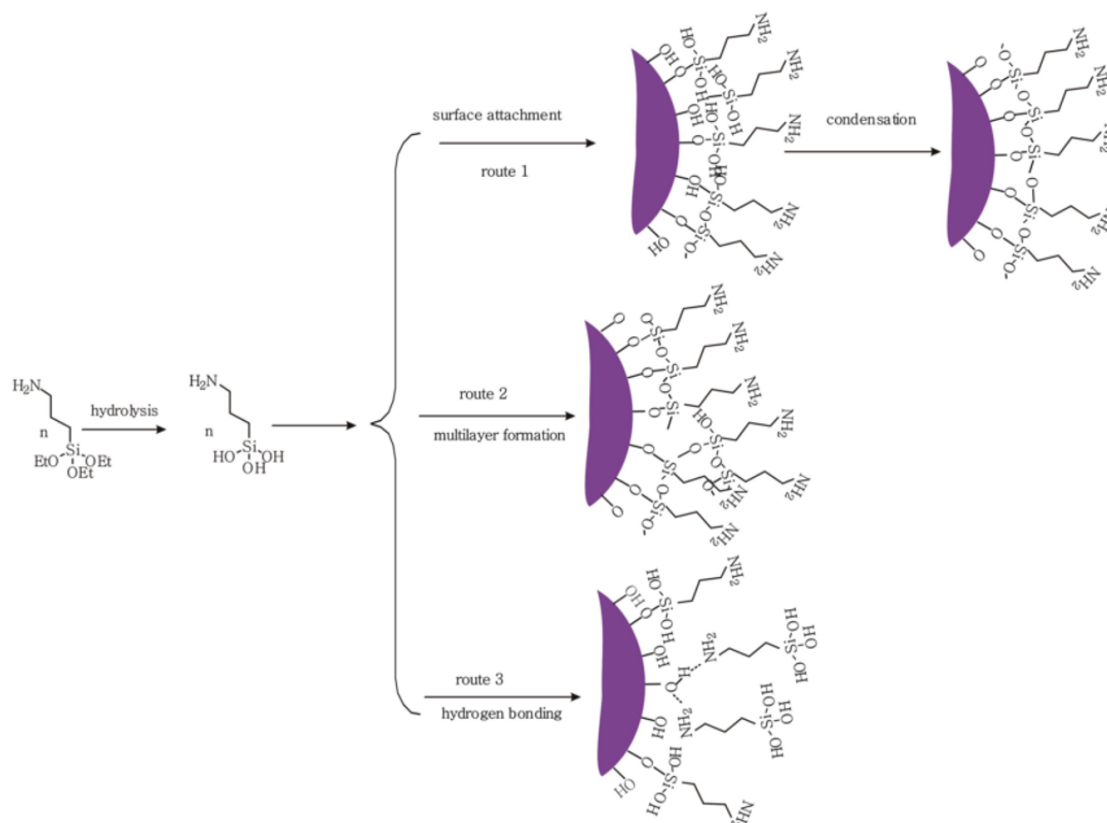


FIGURE 4.2: Scheme detailing the various possible attachments of APTES to iron oxide via surface hydroxyl groups⁹

APTES / APTMS

APTES and APTMS or (3-aminopropyl)triethoxysilyl and (3-aminopropyl)trimethoxysilyl are commonly used linker groups in various core-shell or layer-by-layer deposition processes and their interactions with materials are quite well understood. These chemicals can be utilised for binding to many metal oxide or oxide materials in general.^{9,59,109,111,163}

The paper by Liu et al. provides a very detailed kinetic study as to how APTES can functionalise the surface of Fe_3O_4 nanoparticles,⁹ which we can assume as broadly similar to the functionalisation of our hematite ($\alpha\text{-Fe}_2\text{O}_3$) nanorice particles. APTES which is

seen in figure 4.2 on the left, undergoes hydrolysis in solution with the ethane groups being stable leaving groups, leaving a tri-silanol group exposed. The silanol groups can then covalently bind to the material surface by substituting the hydroxyl groups present on the surface. The preferential arrangement is seen in route 1 in figure 4.2, where the APTES is directly bound to the material surface, the best case scenario for this attachment is that all three silanol groups bind to the surface. Any unbound silanol groups can undergo a condensation mechanism with neighbouring silanol with the eviction of one water molecule, we can also see an unwanted attachment in route 2 where via condensation reaction a free APTES molecule in solution will bind to an APTES group that is already bound to the material surface. In route 3 we see a possible arrangement where by hydrogen bonding an amine end group of APTES can bind to the material surface, or can also proceed with hydrogen bonding to any unbound silanol group.

So to this end route 1 from the figure presented (4.2) is the far preferred arrangement of attachment, as the amine group is the functionality that is needed to further bind with noble metal nanoparticles, and in this binding mode the amine is most available.

An alternative to silyl functionalisation of iron oxide spindle cores has been published, using lysine as a linker group.¹⁶⁴ This amino acid can bind to the iron oxide surface by bi-dentate bridging coordination, or in ionic coordination to surface hydroxyl groups, again leaving a free amine group to secure metal nanoparticles to the iron oxide core.¹⁶⁶

Polyelectrolyte

Polyelectrolyte polymers have also been investigated as an intermediate linking group between iron oxides and noble metals. These polymers arranged around the core have been used in pairs of one negative, and one positively charged. These can act as linking groups in that they arrange in a smooth fashion around the core, and via electrostatic attraction, can pull particles with slight charges to the surface.

In the paper by Zhu et al. they discuss that the strong electronegative charge of the initial AuCl_4^- reagent strongly adsorbs to the polyelectrolyte poly(styrenesulfonate) -

poly(allylamine hydrochloride), or (PSS - PAH) surface, where through further reduction these act as seeds for further growth of gold into nanoparticles.¹⁶⁷

The study by Liz-Marzan et al. also used PSS but with poly(diallyldimethylammonium chloride) or PDDA as the positive component of the polyelectrolyte pair. In this study they hypothesise that gold is deposited to the iron oxide surface by electrostatic attraction between the positive PDDA and the negatively charged citrate-stabilised gold nanoparticles as they are introduced.¹⁰⁸

The paper by Yeap and others use various polymer groups to stabilise gold nanoparticles to the surface of their magnetite nanorods, but also as a route to improve the colloidal stability of their rods for biomedical applications.¹⁶⁵ Alternatively Wu et. al. functionalised the surface of β -FeOOH nanospindles with polyethylene amine (PEI) to deposit silver seeds,¹⁴⁸ on which further silver growth was performed. The PEI can secure metal nanoparticles through amine groups similarly to APTES.

Ultimately these polyelectrolyte intermediate layers seem to increase the general size of the composite particle as a whole, more than can be seen with directly bound linking groups such as APTES. But these coatings can be also seen to improve the surface density of the noble metal coating due to the smooth, complete coatings of the polyelectrolyte on the core, in affect homogenising the surface for attachment.

Silicate

Some studies have explored the use of a silicate intermediate layer to coat the iron oxide core, which can be seen to have a similar result as discussed above. Through using the Stöber method a silicate layer is grown on the core resulting in a much smoother surface than the core which has quite substantial surface roughness, this then can facilitate a more complete coating with a metal.^{109,168}

The silicate layer in one study has been sensitised with a tin compound, which can act as seeds for preferential growth of noble metal coating on top of the silica intermediate layer.¹⁶⁸ Tin has been used in other studies to help with complete coatings of noble metals as its lattice spacing is close to that of the noble metals desired.¹⁶⁹

The silicate layer can subsequently be functionalised again with silyl linking groups, but is possibly more effective in this process with better deposition likely, such as route 1 in figure 4.2. The silanol groups of the linking molecule can bind to the silicate surface in the same mechanism as it does to an iron oxide surface as cited above.¹⁷⁰

Both the silicate and polyelectrolyte intermediate layers do result in a greater overall increase in the size of the composite particle, with greatest vector increase seen in the width as opposed to the length of the particle, resulting in a decrease of aspect ratio. Thus for applications where the optical resonance is of importance this approach may not be appropriate to use.

4.3.2 Growth of noble metal shells

As mentioned in chapter 1 and section 4.1, it is often desired to coat magnetic or iron oxide nanoparticles with noble metal shells, either for their superior plasmonic properties or as a passivating-inert protective shell, or for two-fold purpose.⁴⁰ In this section a few published methods for creating a noble metal shell on specifically iron oxide nanoparticles with various intermediate linker groups are presented in brief, to indicate the breadth of options available to perform this task.

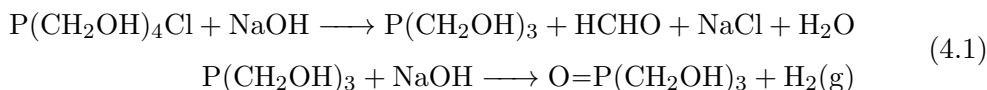
Duff's gold seeds

Many published methods for coating iron oxide nanoparticles with gold initially use gold seeds deposited on the oxide surface by some linking function described above, on which complete shells are grown due to preferential growth of metals on kind rather than freely in solution. Many studies have used so called Duff's gold seeds for this purpose, referring to the publication by Duff and Baiker in 1993.^{59,109,163,165,171–176}

Duff's process for synthesis of gold seeds is known as a reliable procedure for making tightly controlled gold nanoparticles of 2-4 nm in size, which the size can be tailored by reaction time and reactant concentrations.^{173,177–180} However if it is not fully required to differentiate the exact size in this range, and the particles are used as seeds for further growth as discussed in this work and other publications, the solution can be allowed

to age and be added to a colloid of core particles with linking group functionalities on which to attach the gold seeds.

The Duff's gold seeds are produced by mixing aqueous solutions of THPC and NaOH at room temperature. Then to initiate the reaction, under constant stirring an aged aqueous solution of HAuCl_4 is added. This is not a direct reduction of the initially added reagents, but it has since been theorised that THPC in basic solutions is partially hydrolysed.^{90,180,181} From equation 4.1 it can be seen that when THPC undergoes hydrolysis formaldehyde, tri(hydroxymethyl)phosphonium oxide (THPO) and hydrogen are produced which are all capable of reducing many precursor metal salts such as HAuCl_4 , AgNO_3 and others.



The oxidation of THPC and the resulting compounds are responsible for stabilising the as formed gold nanoparticles in solution, with THPO and other molecules being weakly bound to the metal surface.^{181,182}

Turkevich gold seeds

Some other publications utilise the small gold particles produced via the Turkevich method to be attached to the core particle, and subsequently act as seeds for further deposition of metals to form a shell.^{111,148}

These seeds are prepared using sodium citrate as reducing agent in solution to reduce HAuCl_4 , resulting in a tightly size controlled colloid,^{183,184} of similar size to those prepared by the Duff method. Unlike the Duff method gold particles are stabilised by citrate ions in solution through the particles' electrical double layer, negating the relative charge of the particle.^{68,181}

Gold Seeds by NaBH_4 reduction

Alternatively NaBH_4 has been utilised as a strong reducing agent by which to produce small gold or silver nanoparticles as seeds for further growth.^{108,148} This reduction method can again produce gold particles (2-5 nm) that are applicable for this purpose.¹⁸⁵ This process similarly stabilises formed gold nanoparticles with ionic groups in solution from NaBH_4 negating the charge of the particle by forming an electrical double layer, and hence increasing the stability of the colloid.

Shell Deposition with Formaldehyde

Some studies have utilised the addition of formaldehyde to solution as reducing agent,^{59,111,168,172} this is sufficiently strong a reducing agent to reduce metal salts like AgNO_3 and HAuCl_4 in the presence of metal seeds of a similar lattice structure. It has been described as a “seed catalysed reduction”,^{111,168} similar to that of other shell deposition processes.^{59,148}

The paper cited here used direct addition of formaldehyde as reducing agent, but in a buffered solution of ammonia to ensure the stability of the metal shell solution over the length of the deposition process, allowing for complete shells to be attained in one growth step.¹⁶⁸

Shell Deposition with Formaldehyde - via THPC

As mentioned above in the subsection 4.3.2 the hydrolysis of THPC in basic solutions results in formaldehyde amongst other reductants being produced. To this end the further growth of noble metals on attached gold seeds can be implemented by addition of further THPC and noble metal precursor salts, along with a basic pH. Ultimately resulting in similar produced shells as the noble metal growth process of adding in pure formaldehyde to reduce a metal precursor, although the kinetics of the reaction will differ from the direct addition of formaldehyde as the hydrolysis of THPC yields other molecules capable of reducing the metal precursor.

Shell Deposition with Hydroxylamine

Hydroxylamine reduction has been touted as another possible route to coating iron oxide nanoparticles with gold,^{108,111,186} along with other core particles.¹⁷⁶

The paper authored by Ma et al. compared the use of formaldehyde (as above) and hydroxylamine chloride as reducing agents for forming gold shells on hematite core particles.¹¹¹ This again proceeds by gold seed catalysed reaction with gold deposition forming on gold seed particles attached to the hematite surface by thiol based linker molecules.

The method of hydroxylamine reduction is as follows: a solution of seed-coated particles and hydroxylamine chloride is added to a pre-aged gold precursor solution of HAuCl_4 and K_2CO_3 and subject to sonication for 2 hours.^{108,111}

It was found that the hydroxylamine reduction formed a more complete gold shell on the core particles than the reduction with formaldehyde, with less bulky gold growths forming, and the greater prominence of an absorbance peak at 586 nm after the reaction is complete.¹¹¹

Shell Deposition with Ascorbic Acid

Previous work has also used ascorbic acid to deposit noble metal shells on iron oxides,^{174,187,188} and other core particles.¹⁸⁹

Two papers showed its applicability to producing gold shells from HAuCl_4 solutions, onto Fe_3O_4 particles. However most applicable to our study the paper by Kartseva et al. showed the distinction between the use of ascorbic acid and formaldehyde to reduce AgNO_3 to form a shell on gold-seeded hematite particles. It was demonstrated that in this case ascorbic acid reduction resulted in a less uniform coating of the core with silver metal coating, and that with increasing deposition the particles attained close to spherical morphologies and as such the presence of discrete longitudinal and transversal resonances were not obvious.¹⁷⁴

Shell Deposition with CO

In the Cai paper where a gold shell was grown on gold seeds attached to a silica shell on top of an iron oxide core, the HAuCl_4 reagent was reduced in the presence of CO in solutions. The shell growth solution was prepared 24 hours in advance of deposition, where HAuCl_4 and K_2CO_3 were combined in solution, then when aged were introduced to the iron oxide - silica - gold seeds in solution, where complete shells were formed in 5 minutes by a gold seed catalysed reduction.¹⁰⁹

Shell Deposition with Sodium Citrate

Both gold and silver shells on iron oxide cores have been formed by reduction of their precursor salts with sodium citrate.^{148,190} One publication used sodium citrate to reduce AgNO_3 , resulting in further growth of silver on silver seeds situated on the $\beta\text{-FeOOH}$ core surface. With subsequent steps of reducing silver precursor with sodium citrate complete shells are formed around the core.¹⁴⁸

Shell Deposition with NaBH_4

One study has used NaBH_4 to form a complete gold shell but in this case on a core of silica, gold seeds are present on the silica core via an amine-thiol linker, which catalyse further growth of gold to form a shell.¹⁷⁵ Similarly to a process discussed prior,^{108,111} an aged solution of HAuCl_4 and K_2CO_3 is introduced to the seeded-silica particles, and a solution of NaBH_4 as reducing agent.

4.4 Experimental

The linking group function in our studies followed most closely the paper by Halas et al. where hematite is functionalised with APTES,⁷² which can be decorated with noble metal nanoparticles. It was elected to use APTES rather than APTMS which is used in the above mentioned publication, but when the APTES or APTMS undergoes

hydrolysis prior to binding to the surface, the resulting surface ligands are the same. The hydrolysis mechanism is probably more favourable with APTES as opposed to APTMS as the ethane leaving group is more stable than methane, but apart from this both linker groups attach in the same way to the same affect; leaving an amine group available for binding metal seeds to the oxide surface.

In short, to every 5 ml solution of nanorice (containing 1.4 gL^{-1} of hematite particles) in IMS, $600 \text{ }\mu\text{L}$ of APTES solution is pipetted, and the mixture left at room temperature under constant stirring for 12 hours. This step is performed in polyethylene beakers, as APTES will readily bind to the silicate surface of glassware. Following this time the solution is washed by centrifuge following the regime in table 2.1, to remove any excess APTES not bound to the core particles. The nanorice-APTES particles were then re-dispersed back into the same original volume of IMS (5 mL) for the next stage.

The nanorice core was then deposited with gold seeds fabricated following Duff's method, which initiate the seed catalysed reduction of noble metal salts to produce metal coating of the hematite core. Briefly, under constant mixing to 45.5 mL of DI water 1.5 mL of 0.2 M NaOH (*aq*) solution is added, along with a diluted solution of the reducing agent THPC (1 mL of a 1.2 mL 80% THPC stock solution made up to 100 mL), and finally 2 mL of the aged chloroauric acid solution (25 mM (*aq*) solution prepared at least 15 minutes prior to its use).¹⁷⁷ This process is known for its quick reliable production of tightly size controlled gold nanoparticles of around 2 nm diameter.^{59,175} Nanorice-APTES particles were introduced to aqueous solution of the gold nanoparticles, and left under stirring for several hours to ensure optimal coverage of the seed nanoparticles over the nanorice cores. Following further centrifugation any un-bound gold nanoparticles and excess reagents could be separated from the nanorice-APTES-Au seeded particles.

We also tested whether silver nanoparticles produced by THPC reduction could similarly be attached to the nanorice core using the APTES linking groups. Silver nanoparticles were prepared in a similar fashion to the gold seeds and a published method.¹⁷⁹ From this study the silver nanoparticles are claimed to be of less than 4 nm in size and so should also act to facilitate the deposition of further metal clusters on to the nanorice core.

It was subsequently explored how to deposit further noble metals onto the metallic seed particles, by two processes: digestive ripening and interface coating. These methods are discussed in the following chapters 5 and 6.

4.4.1 Results and Discussion

It has been found to concur with the literature that through the use of APTES linker groups it is relatively simple to deposit both gold and silver nanoparticle seeds onto the hematite core particles. A good coverage of the core particle surface is observed, however this could be improved by developing the process of functionalising the iron oxide with APTES. APTES is known for its multiple possible configurations of attachment to oxide surfaces as demonstrated in figure 4.2, so if care was taken in this step an optimised coverage could be attained.^{9,191,192}

Electron Microscopy

The hematite spindle shaped cores were analysed by SEM above in section 2.4.1. The addition of APTES linker groups to the hematite surface can not be observed using electron microscopy techniques due to the organic molecules being largely transparent to the high energy incident electron beam. Following the deposition of gold and silver seeds to the nanorice core the resulting composite particles can however be studied, and the contrast difference between the oxide core and noble metal seeds provides rapid confirmation of attachment.

It can be seen in figure 4.3 that the deposition of gold nanoparticle to the hematite core has been successful, and provides a satisfactory coverage of the core particles, on which further metal is to be deposited to complete the shell morphology. It can be seen in figure 4.3 that indeed many gold particles are of around 2 nm diameter consistent with Duff's method and subsequent studies using his process for this function. However, it must be noted the presence of larger gold crystallites of up to 15 nm diameter. The presence of lattice interference patterns in these images has also been used to confirm the materials present in the image. From the images an electron diffraction pattern is computed as a

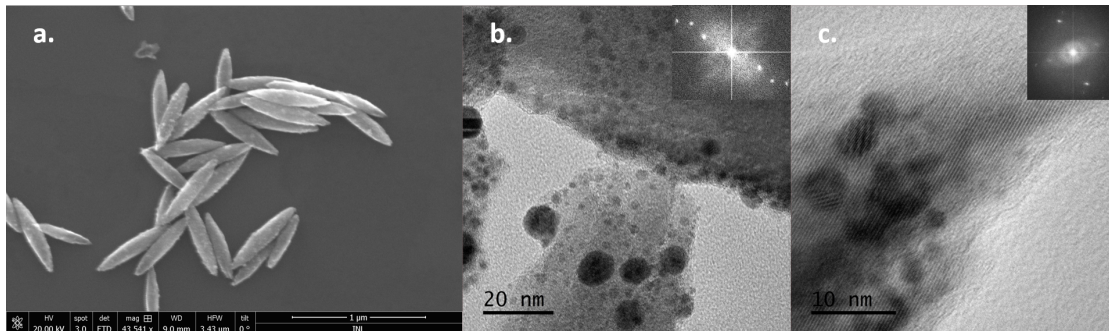


FIGURE 4.3: SEM and TEM images of gold seeds deposited on hematite nanorice cores via APTES linking group. Image a. shows an SEM image of a group of these particles, whereas b. and c. are TEM images with inset electron diffraction patterns

Fast Fourier Transform (FFT), from which lattice spacings can be measured and cross-referenced with the literature values, and then assigned Miller indices to the observed lattice planes. From the images b. and c. in figure 4.3 the lattice planes (111), (112) and (211)/(121) of hematite have been observed, alongside the lattice planes (111) and (110) of gold.

The addition of silver nanoparticles to the nanorice cores has likewise been imaged, as seen in figure 4.4. In these images we have utilised Energy Dispersive X-ray (EDX) mapping to show the distribution of elements of interest in the HRTEM image. In image b. of figure 4.4 the HAADF image shows us the morphology of the particle in question, with the images labelled Fe and Ag corresponding to the presence of these elements where the colour is present. As expected the core strongly displays the presence of iron, while deposited nanoparticles on the surface display as silver as well as a faint display of colour relating to silver over the whole surface of the core. Overall the deposition of silver nanoparticles to the cores is completed to a similar standard as the gold seeds, with many small (1-4 nm) silver seeds dispersed over the whole surface of the hematite core, again via APTES linking groups. Similarly we see the presence of larger crystallites of silver, just as seen in the case of gold, of up to 20 nm diameter deposited on the hematite surface.

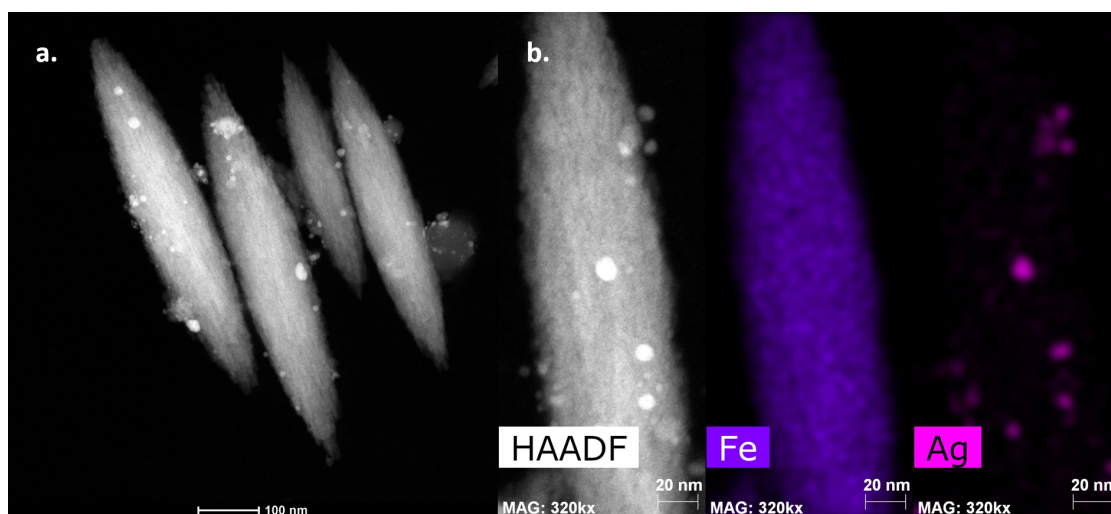


FIGURE 4.4: HRTEM images of silver seeds deposited on hematite nanorice cores via APTES linking group. Image a. shows a group of these particles, whereas b. shows HRTEM-EDX mapping images, showing the spatial data of certain elements

TGA

These stages of coating the hematite nanorice cores with the linker group APTES, and then the deposition of gold nanocrystal seeds has been monitored by the prepared materials' thermal degradation, using TGA.

We can see in figure 4.5 that in the case of bare hematite nanorice particles (as produced in chapter 2 after 72 hours heating), the weight percentage of the material declines very little up until 1400°C. If a substantial amount of akaganeite (β -FeOOH) were to be remaining in the sample we would expect some greater loss of mass at lower temperatures as the iron compound underwent phase transition, ultimately to hematite when heated above 200°C.¹⁹³ If there was presence of other iron oxides such as magnetite (Fe_3O_4) then we would again expect reductions in the sample's mass as the iron compound underwent phase transformations at 200 and 400°C.^{130,144} Slight mass loss in this region could be attributed to exposed faces of particles possibly presenting as these other iron oxide structures, and adsorbed surface water and other groups being vaporised. The sudden

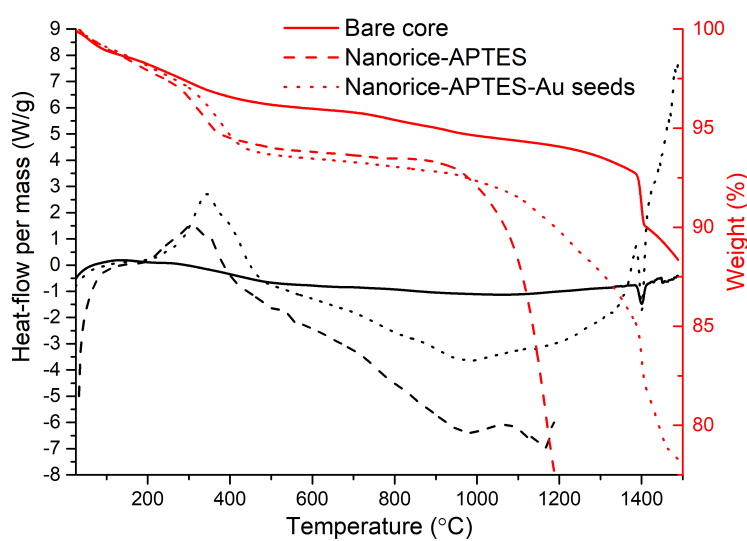


FIGURE 4.5: Thermo-gravimetric analysis data plot of hematite nanorice, nanorice functionalised with APTES and of nanorice with deposited gold seeds via APTES group

mass loss at 1400°C of around 3% of the mass fits with calculated mass loss values for phase transition of hematite to magnetite and the loss of oxygen. A sharp trough at 1400°C in the plotted heat transfer against mass is also indicative of this endothermic phase transition.¹⁹⁴

When the functionalisation of hematite cores with APTES is performed, we see an increased loss of mass at lower temperatures, from R.T. and increasing in rate between 300 and 425°C. This coincides with an exothermic peak in the Wg^{-1} plot, and this is attributed to the APTES molecules bound to the surface of the hematite nanorice being burnt at the elevated temperatures and being lost into the gas phase, hence a reduction in sample weight. Above 425°C this sample echoes closely the sample of pure hematite, where little loss of mass is observed up until $\approx 950^\circ\text{C}$. Between 950 and 1200°C (as can be seen in figure 4.5) a large, gradual mass loss ($\geq 15\%$) is observed, with a corresponding slight exothermic peak (1080°C) in the Wg^{-1} plot. This observation can not be confidently explained or justified from the available literature, however the exothermic nature suggests some loss/burning of surface bound organics or functionalities, rather than a phase transition such as hematite-magnetite which is endothermic.¹⁹⁴

A further difference can be observed as our hematite nanorice cores are decorated with gold seed nanoparticles, attached to the cores via amine interactions on the surface bound APTES. The initial loss of mass due to organic compound burning between R.T. and 450°C occurs at a slightly slower rate, than the sample without gold seeds attached. The data then again shows an almost horizontal plot with limited mass loss up until around 1100°C. Conversely the gradual loss of mass after 1100°C could well be linked to the sublimation of the attached gold nanoparticles. A sharp loss in mass ($\approx 3\%$) is again observed in this plot at 1400°C with the corresponding trough in Wg^{-1} coinciding with the sudden phase transition from hematite to magnetite of the core particle.

4.5 Conclusions

This chapter has provided a broad base of the existing literature that discuss linking groups and other means by which to establish a core-shell structure or to coat a substrate

with another material. Specifically to be applied to this work it was of more importance to highlight methodologies for coating iron oxide materials with noble metals by an intermediate molecule or material. This review of the literature was separated into the component providing the linking function between core and shell, and the method for producing the metal shell. It has also been explained in this chapter why it is wanted for us to form a noble metal shell, and what benefits this provides for the application.

Experimentally it has been shown that APTES functions sufficiently for this linking group function, immobilizing noble metal seeds to the core, which can provide nucleation points for further metal growth from ions or small clusters in solution. The addition of smaller Duff's gold seed nanoparticles was found to be more evenly distributed over the hematite core particle surface when compared to that of silver nanoparticles similarly prepared by reduction with THPC. However, the discovery of attachment of silver to hematite through APTES in the same way as gold is in itself a revelation. It was also discovered that the coating of hematite with APTES linker groups, and then subsequent deposition of gold seeds improved the thermal stability of the particles, with weight loss occurring at higher temperatures in TGA analysis, while the reduction of hematite to magnetite occurs as expected at around 1400°C again confirming the core crystal structure.

Chapter 5

Digestive Ripening for Shell Deposition

5.1 Introduction

In this chapter discussed is the particle processing method called digestive ripening, which has been the subject of nanoparticle processing publications over the last 20 years.⁶⁷ We were inspired by previous work with this method as a potential route to depositing gold and silver onto our previously prepared hematite core particles.

5.2 Size Focussing

As more and more effort and focus is placed on nanomaterials and particles to answer problems in electronics, environmental and chemical processes; a high control over the particle size or shape is required.^{10,85,195} Control over these factors need to be more accurate and reliable than for the production of other non-nano materials, due to the rapid change in properties observed for any change in dimensions of the particle, the very reason that these desired particles are to be made for. Particles and crystals in the nanometer size regime start to neglect the properties displayed by their bulk counterparts as the surface effects become relatively more substantial, these special scaled size-dependant properties hold from hundreds of nm down to around 1-10 nm where individual difference between these atomic clusters or nuclei are many and large.^{20,23,196,197}

These size dependent properties that change much more rapidly at the 1-10 nm range, will display an average property when these particles are present in a polydisperse sample. This can be acceptable for certain uses where the average property of the colloid is sufficient, but may not be applicable to other applications as the whole population includes particles of other size and properties that may interfere with the results.^{10,85}

Digestive ripening has provided an atypical low temperature process by which shape, size and composition of noble metals can be altered through heating in the presence of a digestive ripening agent, which facilitates an exchange of metal atoms between metals of differently sized nanoparticles resulting in a more monodisperse product than the particles found in the initial colloid.^{10,84,87} This process also has an advantage over size separation methods for gaining a monodisperse sample as inherently size selection

results in waste material whereas digestive ripening is an equilibrium point at which the total mass of metal in the solution is divided into equally sized particles. This process is a fairly modern conception spearheaded by the work of Klaubunde and others from the late 1990s onwards. While the mechanistic properties of the process have not fully been uncovered there has been many controlled studies to try and provide an accurate description for the process.^{10,77,85,198}

There has been several theoretical papers published on how the digestive ripening process can work on producing a monodisperse product and the process by which two metals may alloy from a polydisperse binary system to a monodispersed alloy colloid.^{76,77,84,198} These theoretical papers also highlight how the size and number of particles that will be used in digestive ripening also have to be in a certain range otherwise the process will not yield a monodisperse product, and this seems to agree with results from experiment with bulk gold powders.⁷⁶

It is thought that digestive ripening occurs in complete contrast to the more well understood and established technique called Ostwald ripening, where over time in a polydisperse colloid sample, the smaller particles present are sacrificially destroyed and the larger particles will grow in size. This proceeds until ultimately only one particle is left with a mass equal to the initial total solid mass of the colloid particles.^{77,87} The process of Ostwald ripening is directed by a reduction in interface free energy, explaining why we find a reduction in particle numbers as Ostwald ripening occurs.¹⁹⁸ Digestive ripening works by a different mechanism whereby the smallest or molecular particles in solution will grow at the expense of any larger particles.^{84,87}

These larger particles will be broken down by a digestive ripening agent, pushed back into solution as smaller particulates to then aggregate and grow on other small particles equally. This process has been presented schematically in figure 5.1 resulting in a highly ordered super-lattice of monodisperse particles. As digestive ripening is at odds to Ostwald ripening another force must be present in the reaction to counter any reduction in interface free energy and force a resulting increase in particle number. It is thought that electrostatic forces are responsible for this as strain force is the alternative, and it is assumed that these solid particles in a liquid phase will have no appreciable strain energy.^{83,199}

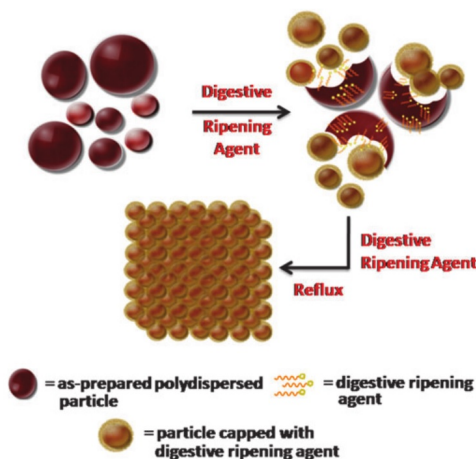


FIGURE 5.1: Diagram showing the role of digestive ripening agent in this process¹⁰

5.3 Digestive Ripening Agent

The use of a digestive ripening agent must be used as a method to reduce the interfacial free energy by reducing the electrostatic potential between metal and the solvent phase. These digestive ripening agents act as simple surfactants placing themselves between the solid particles and the liquid phase thereby reducing the interfacial free energy allowing for transfer of metal ions through solution from the larger particles present in the solution to the smaller. It has been shown that many different surface active agents with different ligand groups can be used, resulting in differing crystal sizes.^{10,78,81,82}

The choice of which surfactant to use in the process of digestive ripening must be based on the desired size of particle to be attained, as each surfactant will result in varying sized particles. This is due to a myriad of factors with each ripening agent being able to reduce the interfacial free energy between particle and solvent to different extents, partially due to steric properties, charges and other energies. These ripening agents can be loosely placed in groups mostly named on the group that has most affinity to the metal being processed, e.g. amine, silanes, phosphines. These surfactants usually have a highly electronegative atom or group of atoms with typically a carbon chain. An

appropriate agent must also be chosen based on the solvent that is being used, as this ripening agent will also act as a surfactant to decrease agglomeration of particles given the correct conditions.

As was mentioned previously much early work on digestive ripening was completed by Klaubunde et al. where digestive ripening was demonstrated to work as a homogenising process for gold and silver nanoparticles, taking them from polydisperse colloids with a particle diameter range from 2-40 nm and turning into particles with diameters 4-5 nm with low poly-dispersity.⁷⁵

Much work has been advanced on using digestive ripening as a process by which to alloy noble metal nanoparticles, now the addition of a secondary metal with which to ripen may throw up issues that were not present when ripening just one metal. As such metals of a similar composition are typically used to minimise these problems; things are made simpler if just one digestive ripening agent / surfactant can be used, or similar experimental conditions such as temperature and solvent are utilised for the two metals.^{77,83-85}

The introduction of two digestive ripening agents has not had as much attention in this area and the use of more than one may result in size focused particles but of possibly two or more distinct populations, or the process could completely fail in its aim and produce a polydisperse product. When mixing two metals in solution and employing the digestive ripening technique to produce an alloy it has often been found that a small or negligible reduction of particle sizes is often found over the whole sample population, this points to the proposed mechanism of surfactants reducing the interfacial tensions of the largest particles in the sample, releasing small atomic clusters or ions into solution to attach to smaller particles growing on the established crystal structures.^{84,200} The overall reduction in size points to a total increase in number of particles. The LSPR properties of the produced alloy particles can easily be monitored by UV/Vis during the reaction, as it has been seen that over the length of the procedure two discrete λ_{max} for each metal will shift to each other and integrate into one peak when the process of alloying is complete.^{83,84}

SEM and TEM images of particles produced in this method provide data of average

sizes of a large sample population, these particles are often formed into superlattices of regular distribution partially due to the monodispersity. These images are also of importance when working with alloys or core/shell morphologies, as it can be seen the alloys tend to have excellent atomic ordering within the particle with no areas of contrasting density.^{77,84,200} This points to the uniform mixing of atomic level components throughout all particles.

In summary, size focusing, digestive ripening or inverse Ostwald ripening has allowed for precisely controlled production of a range of noble metal and other metal particles and their corresponding alloys, with a variety of metals and digestive ripening agents to be used in conjunction with each other. This method has shown that it is possible to create monodisperse nanoparticle populations of a set size and can conceivably also provide routes for synthesizing more metal particles.

Digestive ripening has been of interest to us as a chemical process resulting in monodisperse particle populations in the hope that we can translate this high control to the deposition of noble metals onto magnetic cores. By preparing concise populations of nanoparticles with digestive ripening it was theorised that we could make more uniform coatings on the core particles than had been prepared before in published methods. We also saw digestive ripening's potential to alloy two noble metals as a positive aspect for us to use in that we could then tailor the optical properties of the resulting core-shell particles.

5.4 Experimental

For this area of study, a process that can be linked to the digestive ripening of nanoparticles has been applied to form coatings of mixed noble metals on a core with good surface density. THPC reduction in basic solution was used with gentle heating to reduce both gold and silver precursors, proceeding via the path presented in equation 4.1. With the extended heating times of up to 5 hours, THPC and other in-situ formed reaction products may act as digestive ripening agents.

Experiments were conducted with the reagent concentrations and volumes as logged in table A.1 (Appendix A), where all solutions were dispersed in a sealed vessel with THPC

solution being introduced last as the reducing agent. Then the vessels were placed into a laboratory oven already heated to the noted temperature. After the reaction time had been met the samples were removed from heating and allowed to cool to room temperature. The thus formed core-shell particles were retained and separated from un-reacted reagents and smaller particles by following the centrifuge regime as described in table 2.1.

The synthesis products were stored in IMS and then analysed by the methods discussed below after being prepared in a manor relevant for the analysis technique.

The gold shell growth solution referred to in tables A.1 (Appendix A) and 5.1 is a precursor solution used in several other studies on forming gold shells,^{108,111} whereby an aged solution of HAuCl_4 (5.55 mM) and K_2CO_3 is used. This is a modification of Zsigmondy's method for preparation of gold sols. The gold seeded nanorice solution used in this process and in section 6 were standardised to have a dry mass of precipitate particles corresponding to 1.4 g per 1 litre of the dispersed particles in IMS. The preparation of these seeded particles were kept the same each time to ensure continuity throughout the following experiments.

5.4.1 Results and Discussion

UV/Vis

TABLE 5.1: Table presenting difference in proportion of gold and silver precursors used in synthesis of conditions presented in figure 5.2

Name	5mM AgNO_3 _(aq) (mL)	Au shell growth sol _(aq) (mL)
DR51	1.5	3.5
DR52	2	3
DR53	2.5	2.5

By collecting UV/Vis spectroscopic data for the particles produced through this method of experimentation we can tend to see the relative presences of gold and silver forming

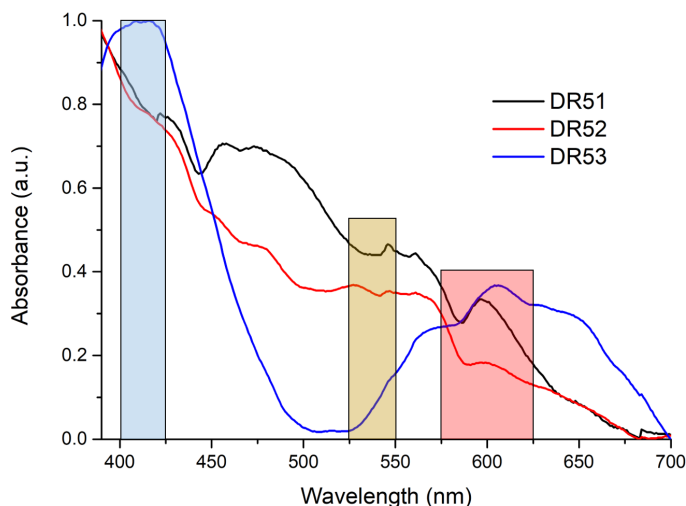


FIGURE 5.2: UV/Vis spectroscopy of samples DR51, 52 and 53

the shell, as well as the degree of completeness of the shell. With a greater proportion of gold a typical peak position for gold nanoparticles at around 550 nm, red-shifting with increasing size, will be more prominent. However if silver nanoparticles are the more prevalent metal, then an absorbance peak at around 410 nm would be marked. The alloying of gold by silver typically results in a blue-shift of the resonant gold peak.

We see in figure 5.2 the UV/Vis spectra of DR51 through 53, which incrementally increases the proportion of silver precursor to gold in the coating step as presented in table 5.1. A relative increase in absorbance at ≈ 420 nm (blue band) reflects this increase in silver presence, while a relative decrease in absorbance of the range 525–550 nm (gold band) indicates a lessening proportion of gold. A peak at 590–610 nm (red band) can be attributed to the noble metal shell being adequately complete so that a resonance over the whole surface of the particle is resulting as discussed in chapter 4. A slight red-shift of this resonance peak is seen, which could be attributed to the fact that increasing silver resulted in bulkier metal growths on the metal core. While a broad absorbance at 500–550 nm can be attributed to the scattering properties of the hematite core itself.

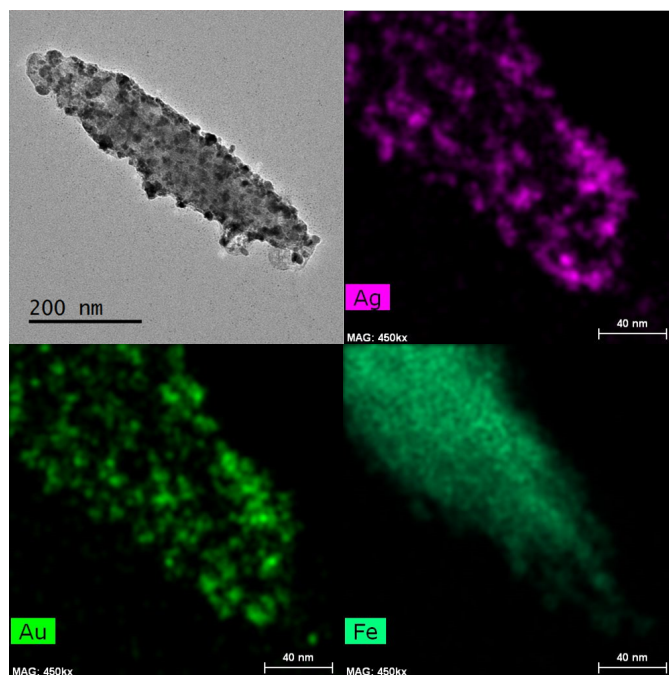


FIGURE 5.3: HRTEM-EDX mapping of sample DR51

Electron Microscopy

From electron microscopy studies it was found that the samples labelled DR51 and DR52 resulted in the best coverage of the hematite nanorice cores with gold and silver, and so are discussed below.

DR51 had the most complete shell formed on the core particle shown in figure 5.3, where the majority of the shell is formed mostly of gold with some silver, as the experimental method used a ratio of 3:7 of silver and gold precursor salts by concentration. The EDX mapping relating to the HRTEM images gained of DR51 allows us to qualify that the growth of gold and silver has proceeded from the previously deposited gold seeds growing into larger islands on the core surface. We also see the presence of silver nanoparticles at the iron oxide surface where gold seeds are not present, indicating that APTES linking groups had not been fully saturated with gold seed particles, allowing for silver nanoparticles formed in the shell growth step to attach to the core themselves.

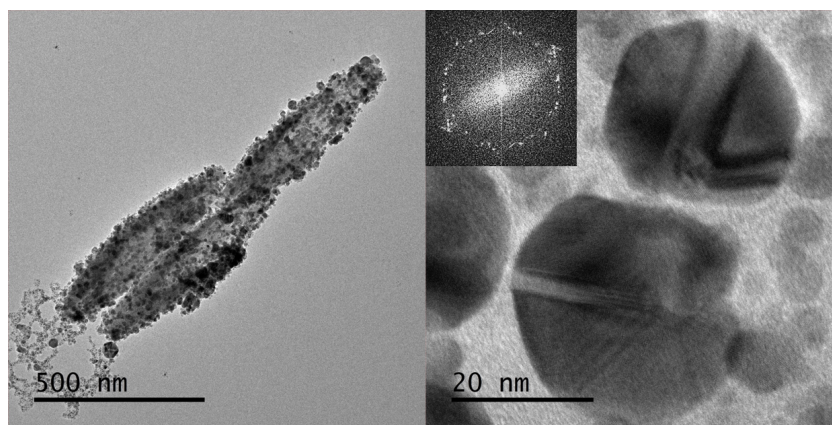


FIGURE 5.4: HRTEM image of sample DR52 with inset electron diffraction pattern

The close proximity of gold and silver in many areas of the elemental mapping indicate either close mixing of the two metals or complete alloying, while in other areas core-shell morphologies are observed (figure D.2 in Appendix D).

The sample DR52 had a similarly complete shell formed as DR51, with a larger proportion of silver precursor in the reaction conditions, resulting in a relative larger growth of silver particles. The almost identical lattice parameters of gold and silver allow for the easy growth and alloying of these two metals with each other. DR52 shown in figure 5.4 displays how the silver has grown epitaxially on the attached seeds, and grown outwards from the iron oxide surface resulting in larger and bulkier growths than was found in figure 5.3. By analysis of the electron diffraction pattern inset in figure 5.4; and of other images, interplanar distances matching to the lattice planes (111) and (200) of gold and silver were identified. It is not possible to discriminate between these two metals, or their alloys by this method due to the close matching of their face-centered cubic (FCC) lattice parameters. The close matching of lattice parameters for gold and silver goes some way to justifying why they can be alloyed in this way with the use of digestive ripening agents.

It was also found through electron microscopy studies that tailoring the relative ratio of hematite core particles to the gold precursor was important for attaining the greater

TABLE 5.2: Table presenting difference in proportion of gold precursor to seeded core particles used in the synthesis of conditions presented in figure 5.5

Name	Au seeded nanorice (mL)	Au shell growth sol _(aq) (mL)
DR42	0.1022	5
DR45	0.073	4
DR46	0.073	3
DR47	0.073	2
DR48	0.073	1

coverage of the core, agreeing with other studies.¹¹¹ Samples DR46, 47 and 42 shown in figure 5.5 had the most disperse coating of gold nanoparticles on the hematite core surface, which meant a reduction of gold precursor quantity, or an increasing concentration of seeded-cores by 50% resulted in better deposition of further gold.

5.5 Conclusions

It was found that through the adaptation of a digestive ripening procedure, that the process could be applied to coating core particles (hematite nanorice–APTES) with gold and silver nanoparticles. The process may not stick true to the original definition of digestive ripening: to focus the size dispersion of the particles, but its use has enabled the deposition and alloying of varying proportions of gold and silver. A mostly complete shell has been attained, giving rise to plasmon resonances from the constituent particle, and not just the individual nanoparticles decorating the core particles. This shell–resonance peak position is then able to be blue or red-shifted by varying proportion of gold to silver deposited on to the core particles.

It is thought that the metal shells could be made more complete in their coverage by multiple iterations of this digestive ripening step, and maybe by varying the ratio of gold to silver reagent in each iteration this process could be further perfected to tune the optical resonances.

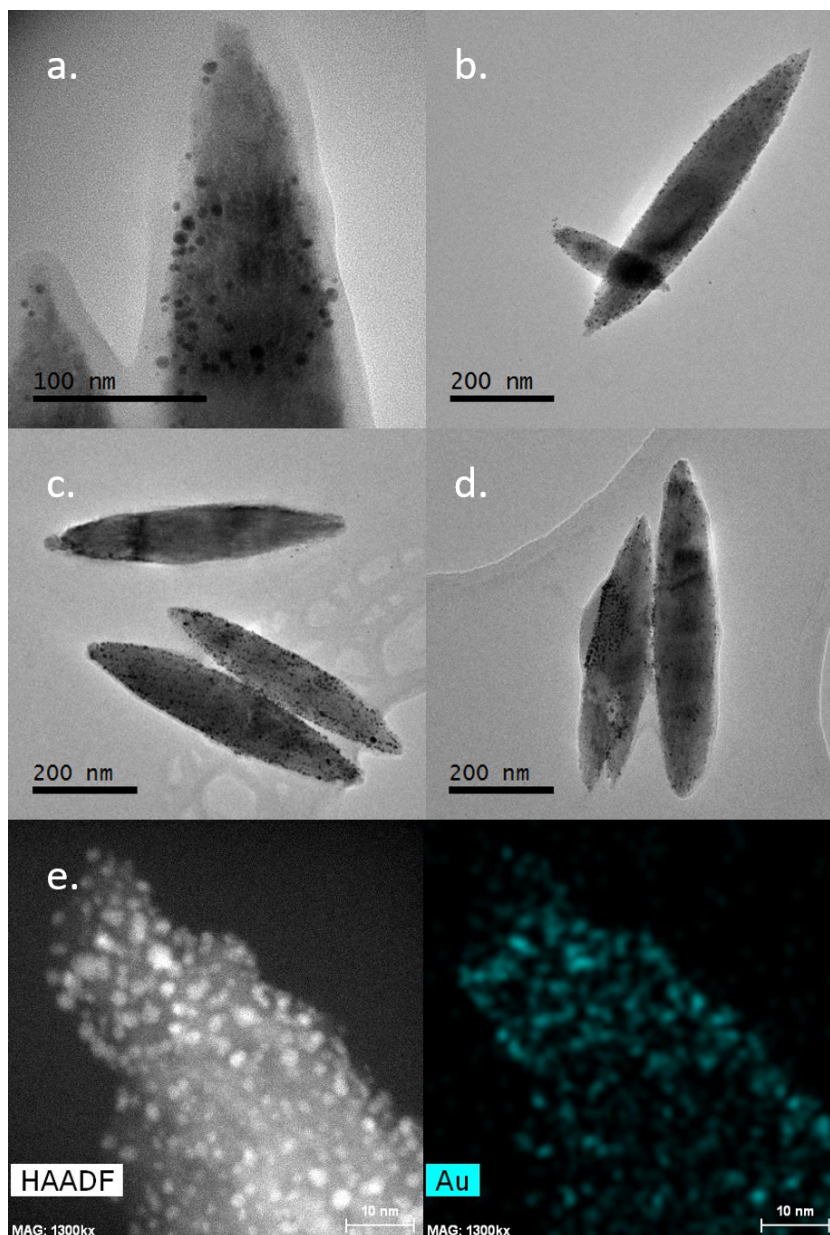


FIGURE 5.5: HRTEM images of cores coated with varying amounts of gold. Images a., b., c. and d. are of samples DR45, 46, 47 and 48 respectively, while image e. shows HRTEM-EDX mapping of sample DR42

Chapter 6

Interface Coating

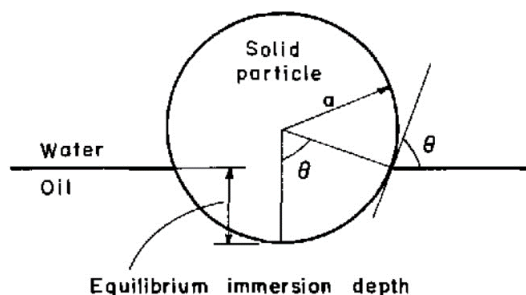


FIGURE 6.1: Diagram showing the equilibrium position of a spherical particle at the interface of two liquids, resulting in a reduction of interfacial tension¹¹

6.1 Introduction

The interface between two immiscible phases was identified in the 1990s as a controlled system at which nanoparticles of various materials and properties can be deposited as a thin film precipitate between the two phases. This arrangement of particles being formed and settling at the interface results from the interfacial tensions between the two phases, with the addition of small enough particles to this boundary resulting in a favourable overall decrease in the interfacial tensions. In this sense these particles are acting as a sort of solid phase surfactant.^{11,201–204} Typically, chemical reagents used to synthesise these thin films are chosen and prepared to be dispersed in both the phases, so that they interact with each other primarily in close proximity to the interface. Due to the reagents interacting close to the interface this in turn helps the crystalline particles formed to be stable at the interface, displaying bi-functional anisotropic properties. The particles are necessarily Janus, or two faced particles, with surface groups often present on the particles of the side of one phase or the other. These surface groups often help to make the particle stable at the boundary by utilising several available forces. The presence of hydrophilic groups by hydrogen bonding or van der Waals etc. can help to improve the wettability of the particle, or otherwise lipophilic groups can be used if the particles are more stable in aqueous phases to maintain the wettability angle (θ in figure 6.1 of the particulate at close to 90°).

As mentioned above the wettability angle of a particle at the interface of two liquids is a crucial term in determining how stable the emulsion will be with the solid surfactant. These balancing of energies to describe a solid sphere adsorbing to the interface is described by the Gibbs free energy equations 6.1 or 6.2 that have been derived for this system.

$$\Delta G = -\pi r^2 \gamma_{wo} (1 - \cos\theta)^2 \quad (6.1)$$

$$\Delta G = -\pi r^2 \gamma_{wo} (\gamma_{wo} - \gamma_{pw} + \gamma_{po})^2 \quad (6.2)$$

These equations represent the interfacial tension energy loss with a particle interrupting the interface with ΔG . The r term is the radius of the solid particle, with γ_{wo} , γ_{pw} and γ_{po} representing the interfacial energies of water-oil, particle-water and particle-oil respectively. The $(1 - \cos\theta)^2$ term stands for the loss of interface area between the two liquids when the spherical particle is at its equilibrium state, with a given θ or contact angle.

6.2 Previous work

Previous publications in this area are centred around the self assembly of nanoparticulate metals, their alloys, chalcogenides and other materials into thin films at the interface of two liquid phases.^{90,101,205,206} This self assembly of synthesised particles to the interface is driven by the resulting loss in interfacial energy as considered above, and explained by the adaptation of Gibbs equation in 6.1.

These studies typically involve reactants being dispersed in both organic and aqueous phases, which upon reaction initiation can diffuse somewhat across the interface and react forming the desired material. Gold and silver thin films of nanoparticles have been studied to a greater extent in this area, whereby varying reaction conditions and reactants the thin film properties can be suitably controlled.^{207,208}

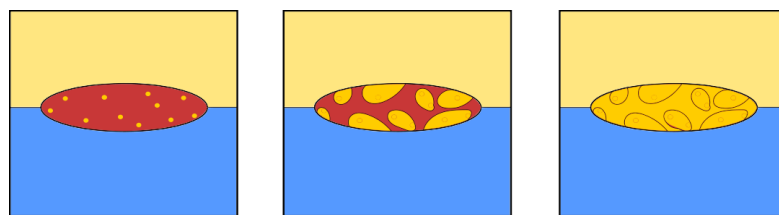


FIGURE 6.2: Diagram showing coating of hematite nanorice core with gold and silver particulates when suspended at the interface of water and toluene phases.

The interface of two liquids has also been studied for the self assembly of pre-synthesised nanoparticles,^{91,209} and how ligand exchange or other adaptations can change the film properties. Other work has looked at ligands that are able to transfer metal nanoparticles across the liquid-liquid boundary aptly described as “phase transfer agents”.^{90,210,211}

Despite the breadth of work in this area concerning nanoparticle synthesis and adsorption to and from the liquid-liquid interface, it has up until now not been utilised for a secondary nanoparticle deposition or growth stage. This potential has been explored in the following experiments and it is hoped to prove that this system can be utilised and is aptly suited for that purpose.

6.3 Interface coating

Work has been conducted into trying to apply this thin-film nanoparticle synthesis method to a secondary particle coating process, in which it was hoped that the hematite nanorice cores discussed prior could be coated with noble metal nanoparticles. In fig. 6.2 we have assumed that the nanorice particles will adsorb to the interface with the longest axis of the particle aligned on or closely to the interface of the two fluids. Extending the equations 6.1 & 6.2 above it is assumed that with the nanorice aligned along the interface that this would result in the largest reduction in interfacial tension, due to the maximum area of the interface being interrupted by the particle.

From the previous work we see that this synthetic process can possess high control over the size of the particles produced, controlled by reagent concentrations, beaker dimensions, protecting groups and reaction temperature. It was anticipated that this high control could be applied to coating pre-synthesised cores settled at the interface with further particles, as when the nanoparticles of controlled size form at the interface, they will attach preferentially to linker groups present on the core, increasing the particle size and increasing the reduction of interfacial energies. The process has also shown its flexibility by producing alloyed materials with tight regulation over the ratios of the amalgam, which could be embraced to manipulate the optical properties of the coating.

6.4 Experimental

Using a published method on producing thin films of gold and silver nanoparticles at the interface of toluene and water,^{90,101} many experiments have been conducted to explore how to adjust this process to coat the hematite nanorice core particles discussed in chapter 2. A summary of all experiments performed are displayed in table B.1 (Appendix B).

Efforts were made to study the effect of alloying with gold and silver deposition on the core particle, changes in reagent concentrations, iterations of deposition steps, and of adding in molecular surfactants to improve the quantitative recovery of the metal coated particles. As this method was an adaptation of a process for synthesising metallic thin films, the resulting precipitate was not of solely noble metal coated core particles, but also of many other noble metal nanoparticles forming as a thin film. To recover our desired core-shell particles the centrifuge washing regime outlined in table 2.1 was used, at each stage collecting the precipitate. For this stage the introduction of the surfactant CTAB proved useful for bringing the as-formed thin film into aqueous solution, as the amphiphilic nature of the interface thin film meant it became difficult to disperse solely in aqueous solutions.

Some parallels here of the difficulty to disperse the resulting particles in one solvent for washing and characterisation/application, and the stability of in-situ prepared Pickering

emulsions discussed in chapter 9 can be drawn. Both processes have used largely similar reaction conditions and precursors, and as such the particles formed at the interface of the two phases are stabilised by hydrophobic and hydrophilic ligands. This property is a slight draw back for this shell coating process, while conversely it underpins the superior emulsion stability discussed in chapter 9. However the use of surfactants to increase the dispersibility of the produced particles in aqueous solutions doesn't pose much issue considering the final applicaiton of the particles; being likewise in aqueous solutions.

6.4.1 Results and Discussion

UV/Vis

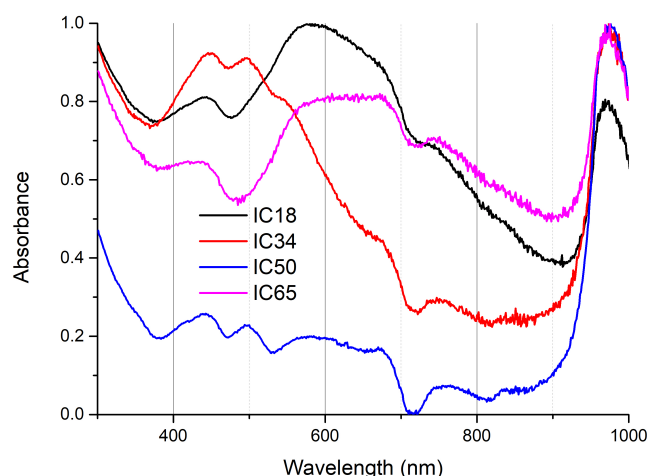


FIGURE 6.3: UV/Vis absorption spectra of four hematite nanorice cores coated at the toluene-water interface; with either gold, or gold and silver.

Through the use of UV/Vis absorbance spectroscopy we can differentiate between bare hematite cores, cores coated with metal seed nanoparticles, and hence the further growth of metal shells on the core. The nanorice particles produced as detailed in section 2.4, exhibit a weak absorbance of ≈ 550 nm as to be expected from the strong red colouration

of the precipitate. With the addition of gold and silver nanoparticle seeds, typical absorbance peaks of these entities are observed in the spectra.

Gold nanoparticles in the range of 1–15 nm tend to have an absorbance peak in the range of 520–550 nm,^{24,177,212,213} so an increased absorbance in this region can be linked to the presence of discrete gold nanoparticles deposited on the nanorice core. However as our gold seeds are prepared by the as named “Duff” process these ultra-small gold nanoparticles of 1–3 nm have very weak absorbance when compared to larger gold crystals,¹⁷⁷ and so an increased absorbance in this region can also be attributed to the growth of gold seeds on the core surface from further reduction of the metal precursor.

Silver nanoparticles of a similar size typically have an absorbance peak in the range of 400–430 nm,^{24,179,213,214} this is again dependant on the size and shape of the particle, the surface groups, the solvent environment and other factors.

In table 6.1 below, when “(A)” is seen in the CTAB column it indicates that this surfactant was added to the reaction vessel after the heating step, and the interface film had been formed.

TABLE 6.1: Table presenting differences in the synthesis conditions presented in figure 6.3

Name	Au(PPh ₃)Cl (mL, mM)	Ag(PPh ₃) ₃ Cl (mL, mM)	THPC (mL @ 50mM)	NaOH (mL, mM)	Au-seeded core (mL, solvent)	APTES- core in toluene (mL)	CTAB (mL, mM)
IC18	10, 1.5	-	0.33	16, 6.25	0.146, toluene	-	-
IC34	5, 1.5	5, 1.5	0.33	16, 6.25	-	0.146	0.5, 25
IC50	5, 1.5	5, 1.5	0.33	16, 12.5	-	0.146	0.5, 25
IC65	20, 1.5	-	0.66	16, 12.5	-	0.146	0.5, 25 (A)

The UV/Vis data presented here seems slightly counter-intuitive when considering the typical absorbance peaks of gold and silver nanoparticles as discussed above. Samples IC18 and 65 had only gold deposited on the core particles, while samples IC34 and 50 had gold and silver deposited in equal proportions, as can be seen in table 6.1. The data shows samples IC18, 34, 50 and 65 presenting an absorbance peak at 450 nm which is

at the high end of the region expected for silver nanoparticles, while samples IC34 and 50 presented an additional absorbance peak at 500 nm which is to be expected for gold nanoparticles. It is asserted that the peak at 500 nm is still arising from the subsequent deposition of silver to the cores, being red-shifted due to alloying with gold or of having larger particle sizes. While the peak at 450 nm is attributed to small gold nanoparticles deposited on the core particle, as this peak is present in each sample, even while silver is no longer present.

We have also observed the presence of an absorbance peak centred at around 580 nm, mainly in samples IC18 and 65, with minor peaks present for samples IC34 and 50. The development of this peak indicates the formation of a more complete shell of gold as is discussed in other publications.^{59,111} As the shell becomes more complete and smooth the absorbance peak would be expected to be further red-shifted which is observed in our data as the minor peak of samples IC34 and 50 present at slightly lower wavelengths, these two samples with only small absorbances in this region have less complete shells of noble metal formed as shown in electron microscopy analysis.

The peak at around 950 nm and upwards in all samples could well be attributed to the transversal plasmon resonance of the composite core-shell particles formed.⁵⁹ While the slight peak seen at 730 nm could be attributed to a 2nd order longitudinal resonance.⁵⁹ Unfortunately as discussed elsewhere the limit of the spectrometer used in this study means that the presence of the main longitudinal resonance peak cannot be identified as this should occur above the wavelength limit of 1100 nm.

Electron Microscopy

Through initial experiments shown in figure 6.4 it was shown that by suspending hematite core particles with attached gold seeds at the interface of toluene and water, along with subsequent reduction of gold and silver precursors, that the growth of these metals was resulted on the attached seeds. By no means was all nanoparticle formation and growth on these core particles, as a thin metallic film at the interface was observed, but through the typical centrifuge washing steps detailed in table 2.1 the larger core shell particles

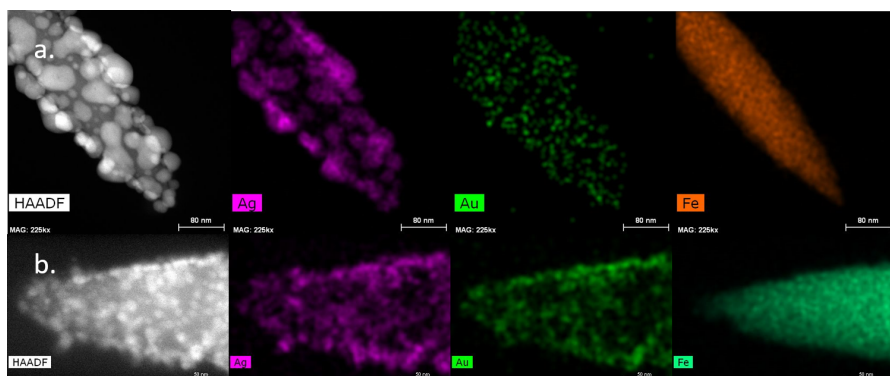


FIGURE 6.4: HRTEM-EDX mapping of hematite cores with gold and silver deposited at the interface, series a. is of silver grown on gold seeds, whereas series b. is of a 50:50 mix of gold and silver grown on gold seeds

could be separated from the smaller gold and silver nanoparticles which remain dispersed in solution.

The HRTEM-EDX maps presented clearly demonstrate the presence of gold and silver growths around a core of iron oxide. The top series a. of images shows the growth of solely silver, presently grown atop of gold seeds, showing the viability of gold seeds for further seed-catalysed growth of both gold and silver. The bottom series b. of images is resulting from the growth of both gold and silver on the gold seeded cores, with a 1:1 ratio of the metal precursors in solution, the EDX data shows that these two metals have an even coverage of the core particles and that alloying of the two metals may have occurred.

One thing to note is that it seems with the further deposition of silver on gold seeds bulkier morphologies are resulting, with growth equally outward in all directions from the core surface. Whereas when gold is deposited simultaneously more of an evenly spread deposition is seen, with more of the cores' surface being covered with the noble metals.

The sample IC18 which is shown in figure 6.5 resulted in a good coverage of the core surface with gold nanoparticles, and as such presented with a UV/Vis absorbance spectra with a reasonably prominent peak at around 580 nm. The inset electron diffraction

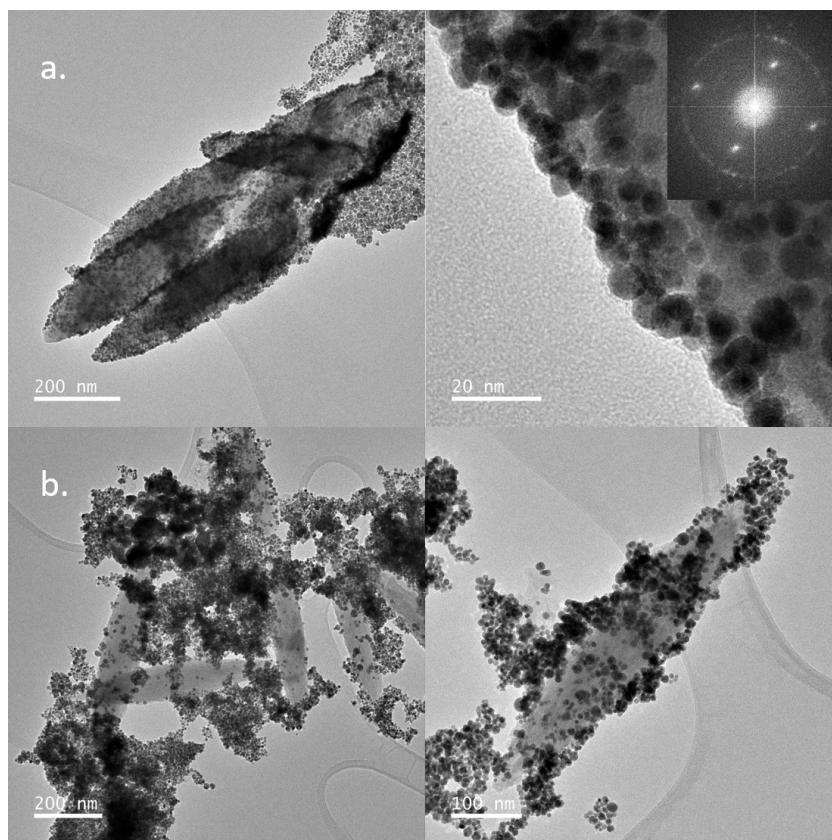


FIGURE 6.5: TEM images of IC18 and IC20 samples: row a. is of IC18 with an inset electron diffraction pattern in the top right corner; row b. is of IC20

pattern in this image has allowed us to identify simultaneously the presence of (112) and (111) crystal planes of hematite and (200) and (211) crystal planes of gold metal, further confirming the deposition of gold on the hematite core surface.

As discussed prior we found that through introduction of the surfactant CTAB that it was easier to disperse the thin film into aqueous solutions, thus allowing for better recovery of our desired particles and separation from reaction by-products. CTAB has been used in many nanoparticle synthesis methods and so it was of import for us to establish whether the introduction of this surfactant prior to metal deposition in anyway

affected the shell growth. Presented in figure 6.5 is samples IC18 and IC20, between which the sole disparity is that IC20 had a small quantity of CTAB introduced to the reaction vessel prior to heating and thin film formation. IC18 instead had the same quantity of CTAB introduced to solution, but conversely this was done after thin film formation and deposition of metal growth on the seeded core particles. Quite a stark difference can be seen between the two images. IC20 has only some regions of further gold growth on the core particles, and many un-attached larger nanoparticles of gold which have been separated from reaction by-products alongside the nanorice are present in the TEM sample. From this contrast it was seen that the addition of CTAB into the reaction vessel was to be performed after shell deposition was complete. This could be explained by the addition of CTAB surfactant to solution prior to reaction initiation meant that growth of gold nanoparticles in solution was more favourable, rather than forming primarily on the core particles as desired.

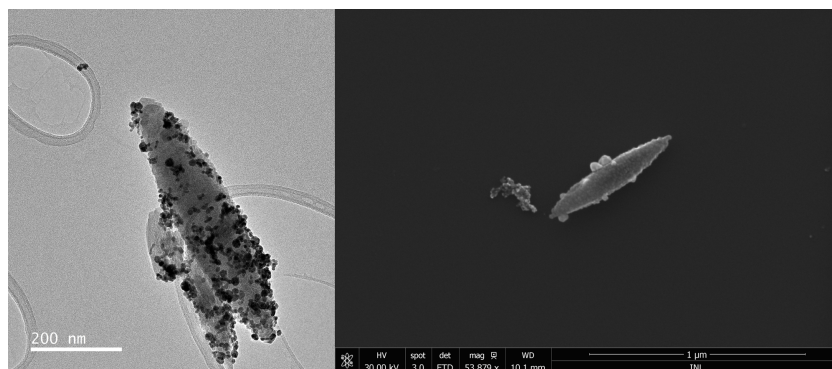


FIGURE 6.6: TEM and SEM images of IC34 sample

Sample IC34 shown in figure 6.6 echoes the reaction variables of the sample presented in series b. of figure 6.4, whereby gold and silver precursors are introduced at a 1:1 ratio, however in this case some CTAB surfactant solution was added prior to metal salt reduction is initiated. The resulting particles show a lesser coverage of the core particle with gold and silver metal, agreeing with the results presented above indicating that CTAB should be added after the reaction is complete. One other difference in the preparation of sample IC34 was that unseeded APTES functionalised core particles were used, so from this we could see that the in-situ deposition of noble metal nanoparticles onto APTES

coated core particles could be performed in this method without the requirement of a pre-seeding step.

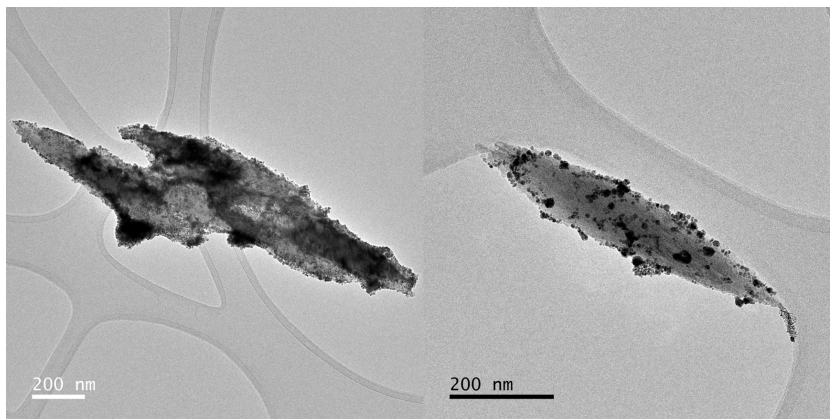


FIGURE 6.7: TEM images of IC50 sample

Following this, sample IC50 was prepared with the introduction of just APTES functionalised core particles without gold seeds. Many core particles in this sample seen in figure 6.7 still attained a better coverage of gold and silver shells than IC34. This is likely down to the increased concentration of NaOH in this experiment, forcing the hydrolysis of THPC to occur at a faster rate, and hence the reduction of metal precursors by formaldehyde and hydrogen occurs at a faster rate stimulating burst nucleation resulting in smaller nanoparticle formation. These smaller nanoparticles can attach themselves more evenly to the free amine groups of APTES due to reduced steric effects, and then more even growth of further gold and silver from solution can occur.

The sample IC65 combined the positive aspects of the above described experiments to provide a good coverage of core particle with a quasi-shell of gold nanoparticles. The increased reactant concentrations allowed for the fast preparation of small gold nanoparticles and their subsequent deposition onto APTES functionalised cores. Increased volume of gold precursor solution allowed for more sustained growth of gold on the in-situ prepared gold seeded cores, and the introduction of CTAB after the reaction is completed allowed for good recovery of the core-shell particles without hampering the deposition process. Again the crystal structures of hematite and gold were established

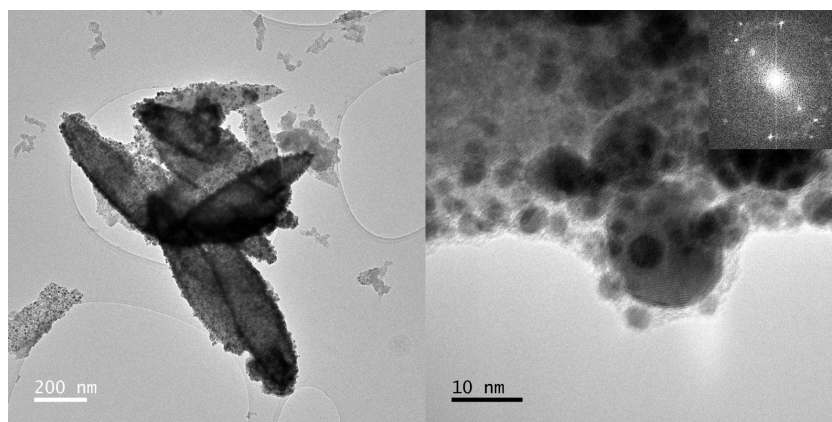


FIGURE 6.8: TEM images of IC65 sample, with inset electron diffraction pattern in the top right corner

present through analysis of the electron diffraction patterns from these HRTEM images shown in figure 6.8.

Initial experiments had gold seeded cores dispersed in IMS added to the two phase reaction system, however it was found that if the core particles were dispersed in toluene instead, they settled and adsorbed to the interface much quicker, and so the reaction could be initiated sooner. This change in method was found to have no negative impact on the coating of the cores, however as the core particles form less stable dispersions in toluene it was important to agitate and mix the colloid thoroughly prior to adding to the reaction vessel.

The addition of PVP as surfactant rather than CTAB was also explored, knowing that it absorbs well to gold and silver surfaces. This was seen to have no affect on the shell coating process, however didn't function as well as CTAB at dispersing the thin film into the aqueous layer prior to centrifuge washing.

Magneto-optic System Testing

Samples IC18, 50 and 65 were tested in CMD Ltd's magneto-optic setup to test their applicability as reporter particles in their diagnostic system as described in section 1.2,

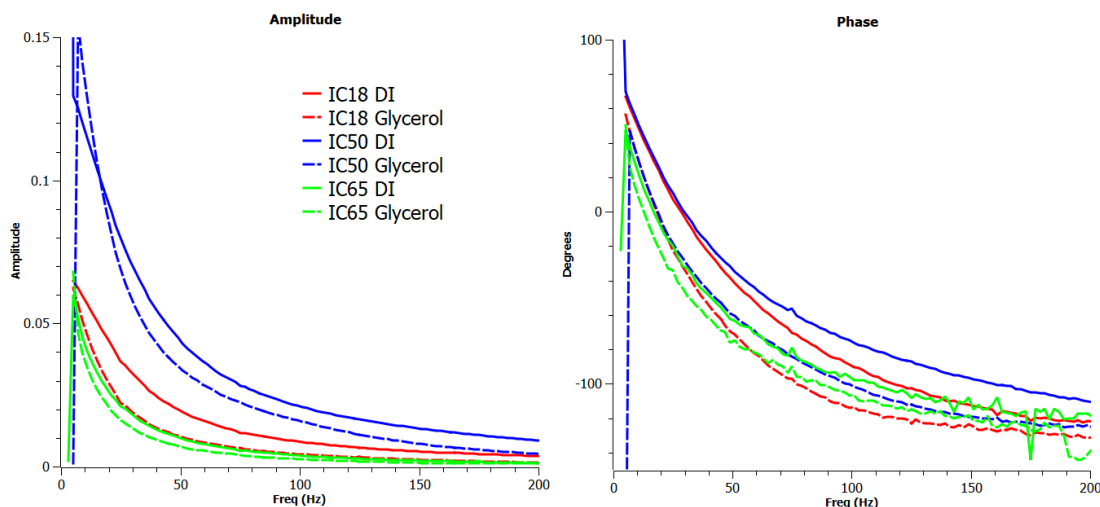


FIGURE 6.9: Plots of amplitude against frequency, and phase against frequency for samples IC18, 50 and 65 in DI water and 25% /w glycerol solutions

with some of the resulting data output is shown in figure 6.9. The particles were tested for their sensitivity for sensing solvent viscosity changes, for this test reporter particles were dispersed in DI water and separately in a solution of 25% /w glycerol in DI water. All three samples were synthesised with the same hematite core particles, so any change in response to varying the oscillating external magnetic field frequency is due to changes in coating deposition, or other particles present in the colloid. The particles are more sensitive to solution viscosity when the phase lag or difference to the oscillating magnetic field is greatest when the solution viscosity is varied a certain amount.

IC50 has been seen to have the least core surface coverage with noble metals, and it is thought because of this the nanorice particles are most able to align themselves in solution with the external magnetic field, due to least surface drag. This sample then presents the highest amplitude value for all frequency values measured, both in DI and in 25% /w glycerol solution. It also provides the highest values of phase lag against frequency for the corresponding solvent environment. Taking values at a frequency of 50 Hz the difference between the particles suspended in DI water and in 25% /w glycerol solution is 25° , making this sample relatively sensitive to solution viscosity changes.

IC18 displayed relatively low plots for amplitude against magnetic field frequency meaning that the measured amplitude of oscillation of optical resonance in the solution is quite low, this could be caused by a larger presence of nanoparticles in solution which are not attached to our core particles, thus wouldn't oscillate with the external magnetic field. This could be improved by more thorough centrifuge washing and processing of the synthesis products. IC18 has also presented with lower values of phase against frequency than IC50, which could in part be due to more complete growth of noble metal shells increasing the drag in solution for this sample. However the difference between DI and 25% /w glycerol solution at 50 Hz oscillation is 29.7° making it the most sensitive to solution viscosity changes of these samples, at this frequency of oscillating magnetic field.

Finally sample IC65 has the lowest values of amplitude against frequency at all points, which could similarly be caused by other nanoparticles dispersed in solution scattering the laser light being used for analysis, thus reducing the overall amplitude of oscillation caused by the core-shell particles induced oscillation. This sample also manifests low values when plotting phase against frequency, with a relatively small difference between the two conditions of particles dispersed in DI or 25% /w glycerol solution. The difference between these two solvent conditions at 50 Hz is only 11.5° , making it less than half as sensitive to viscosity changes as samples IC18 and 50. This could be down to large nanoparticle shell growths on the core particle, rounding out the whole morphology of the particle making the particles' rotation less obvious to this mode of analysis, and the relative drag of the reporter particle is lessened.

6.5 Conclusions

Overall it has been proven through these experiments that by suspending core particles at the interface of two liquids, with subsequent thin film deposition to this interface is an applicable process for coating the core particles with a shell of noble metal nanoparticles. While some issues were met with recovering the core-shell particles initially, this was remedied by the introduction of a surfactant which could negate the dual ligand nature of the interfacially deposited particles.

The interface coating method has allowed a controlled deposition of varying gold to silver ratio on the hematite nanorice cores, while generally more complete shells were formed with a higher fraction of gold. It has also been shown that this process does not require the pre-deposition of gold nanoparticle seeds on the cores to promote further shell growth, while the in-situ generation of metallic nanoparticles is sufficient. The simulated longitudinal resonance responses of core-shell particles of this morphology are out of the scope of the UV/Vis data we have acquired, however with good coverage of the core with noble metal particles we have seen the evolution of an absorbance peak at around 580 nm which matches the observations from other studies forming near-complete gold shells on these hematite spindle shaped particles.^{59,111}

It is expected that with further work and exploration of nucleation factors, and subsequent deposition steps, that better noble metal shells can be formed. This should be possible for both gold and silver shells along with their incremental amalgamation, and as such shifting the optical resonances of the whole composite particles.

Chapter 7

Polyol Synthesis of Silver and Nickel Composites

7.1 Introduction

We have explored an alternative route to producing asymmetric particles with magneto-optic properties without using the hematite nanorice core as discussed in the previous chapters. The process we chose as a candidate alternative synthesis was the previously reported polyol synthesis of nanowires of silver metal, which has been shown to very reliably produce silver wire particles with a width in the order of 50–100 nm and lengths of 1–5 μm .⁶⁷ The polyol process differs from the majority aqueous syntheses described in this thesis in that the solvent used is a polyol which itself or its degradation products performs the in-situ reduction of the metal precursor salt.

The fabrication of asymmetric nanocrystals such as nanowires and nanorods are receiving attention from diverse fields across science due to their unique scalable properties and possible applications. These asymmetric particles are interesting and a desirable synthesis product as new properties of a material are discovered when its dimensions are extended in one plane but not appreciably in the remaining two planes, the aspect ratio describes this feature and the higher this figure the longer and thinner the particle is (as demonstrated in figure 2.8). Asymmetric nanocrystals of noble metals have been studied for their potential applications in electronics, bio-diagnostics and photonics to name a few. These unique properties of nanoscale materials has been well documented for various noble metals and it has become apparent that not just size but morphology and structure of the metal clusters will more often than not alter the optical, magnetic and chemical properties.^{19,41,215–217}

This asymmetry as opposed to symmetrical particles gives a change primarily in LSPR of the nanoparticle,⁴¹ as has been discussed prior in section 1.1.1 and other places in this document. The red-shifted longitudinal resonance is of greatest importance to this study and the intended application, this is best met by high-aspect ratio particles which are still easily dispersed in aqueous solvent.

The polyol system described in this section is a well documented process for producing finely divided particles of many types,¹² primarily of noble metals among others and was pioneered by Fievet et al. in the late 1980s.^{92,93,218}

The polyol process has been demonstrated to be a useful synthesis route for producing metals, metal oxides, chalcogenides and other particles. The produced particles can be in the range of a few nm to μm powders. A variety of polyol compounds have been explored in the publications and the general characteristic of these solvents are that they are viscous, polar and have relatively high boiling points when compared to aqueous solutions. This elevated boiling point when compared to aqueous solutions allows for higher thermal energies to be introduced to the system and thus reduce precursors with higher reduction potentials than is possible in aqueous solution.

Due to the sensitivity of this reaction to multiple variables, temperature of the reaction must be tightly controlled to try and limit variations in the shape and size of the produced particles. Many publications that use the polyol process detail a drop by drop addition of reagents to the reaction vessel, so as to not dramatically reduce the overall temperature of the reaction. Typical injection rates vary between 1–50 mL/hr in an attempt to keep the reaction balanced between thermodynamic and kinetic forces;²¹⁹ it has been demonstrated many times that by changing the temperature of this reaction by 5–10°C will change both the shape of the formed particles, their size and the dispersity of the sample.^{95,219} A highly monodisperse product is often wished and by using slow injection and not reducing the system temperature too dramatically the product is likely more highly coherent.⁴¹ This slow addition rate of reagents also controls the concentration of metal ions in solution, controlling growth.

7.2 Polyol solvent

The polyol solvent used in this process is ethylene glycol ($\text{C}_2\text{H}_6\text{O}_2$) with two alcohol groups positioned on the ends of the carbon chain, that has a boiling point of 197.3°C.

Ethylene glycol is used in this process as both the solvent in which the metal salts and other precursors are dissolved, and as the reducing agent / precursor in the system.^{95,217} As ethylene glycol is used as the solvent medium reaction temperatures can be used up to around 190°C prior to evaporation and higher under reflux. Often a surfactant or protecting group such as polyvinylpyrrolidone (PVP) is introduced, usually as a method

to prevent further agglomeration of nanoparticles once formed into crystalline structures. The presence of a protecting group is also of increased importance when working with a metal that possesses magnetic properties and as such agglomeration may occur more easily.

It is understood that under heating the ethylene glycol (EG) used as solvent will degrade to several groups dependant on the reaction temperature each with varying reduction potentials which are able to reduce the as added metal salts in solution. In previous experiments conducted by Fievet et al. it was thought that acetaldehyde was the in-situ formed reducing agent as diacetyl was detected in the final solution.^{92,93,220,221} This is likely true in the published case but is probably a side product from the initial reduction of the cobalt and nickel hydroxide precursors used promoting acetaldehyde production from the presence of as formed hydroxide ions. As such it is now thought that glycoaldehyde is a common in-situ reducing agent alongside EG itself responsible for many polyol syntheses of silver nanostructures.^{12,218,220}

7.3 Silver nanowires

In the case of silver nanowires the metal salt precursor: usually AgNO_3 ; is added drop wise into the reaction vessel, where it is first released into solution as Ag^+ ions. These ions are then reduced by the solvent and will combine to form small nuclei of metallic silver, with no as yet defined crystal structure as this will change depending on the reaction conditions and the energetic favourability of certain structures. It has been suggested that the nanowire structures can only form from seeds with a multiply twinned decahedral structure rather than just a single crystal FCC structure, so this ability for the small nuclei to form and remove such defects in-situ is important for this process.^{19,222} As the nuclei grow they become stuck with their current crystal structure as the required thermal energy to convert structure at this stage is too costly. These can now be considered seeds for further crystal growth epitaxially as their structure will not now change.^{12,65,66,222}

The reaction is often said to be monitored by colour, where upon initial addition of AgNO_3 the solution turns slightly yellow, indicating the production of small silver nanocrystal seeds. As the reaction continues the solution should turn more to a grey-silver colour and over the reaction time will become more thick, wispy and turbid, which is the accepted visual confirmation of the formation of nanowires.^{216,219,221} The reaction is often left at reaction temperature for around an hour after all reagents have been added, as the final stage progresses by Ostwald ripening this just allows more time for the nanowires to form and use up any leftover metal nuclei and small clusters.⁶⁵

Some publications on this method report a product yield of 90–95% nanowires but this often involves the use of pre-synthesised seeds, with slightly lower yields having been gained from methods that don't use seeds. A common technique for separating the nanowires from any other formed nanocrystals is by centrifugation, as the nanowires are much harder to disperse in solvents such as acetone and ethanol than any much smaller nanocrystals formed in this reaction, the supernatant can be removed after centrifugation removing any extraneous ions, reactants and unwanted nanocrystals.^{215,219,221}

A typical reaction of this method will start with heating a portion of EG to the reaction temperature, for silver synthesis this tends to be around 160–170°C but metal salts with higher reduction potentials will require higher temperatures, which can be up to 190°C with EG as a solvent. Often reflux apparatus is set up so as to ensure no evaporation of solvent over the reaction time. The EG solvent will often be kept at this elevated temperature for a while prior to adding any additional reagents,^{12,216,221} some groups have had success with adding in the PVP at this early stage whereas others inject the PVP solution simultaneously with the metal salt solutions. After the solvent has been pre-heated, typically low concentrations (or lower than that of PVP concentration) of metal salt precursors in EG are added drop wise to the heated reaction vessel.

7.3.1 PVP

Controlled growth in these conditions will occur in either; 3 steps in a one-pot reaction, or in two steps when using pre-synthesised seeds on which to grow. In the case of a one-pot synthesis, the reaction will start with the metal salt/salts being reduced to form free

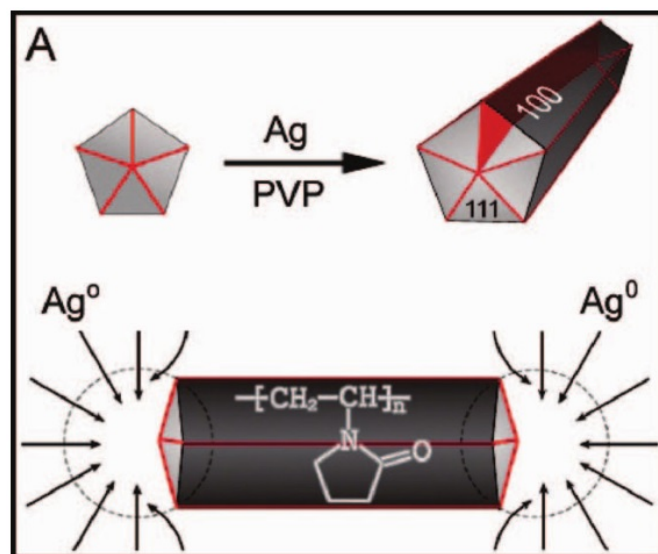


FIGURE 7.1: Diagram showing how PVP preferentially protects the (100) crystal face of silver nanowires¹²

atoms and metal ions in solution which arrange into small metal clusters, secondly these nuclei or small clusters will become seeds with defined crystal structures and faces that can be monitored, and thirdly the seeds will be directed to grow in certain planes giving distinct morphologies.^{12,65} At each step there is a combination of thermodynamic and kinetic factors that must be considered and any slight change in any one factor can result in particles of different shapes and sizes being formed. The formation of specific shapes or morphologies from this method is not fully understood due to the lack of experimental tools available to show the mechanism of seed formation from small atomic clusters or ions in-situ.^{12,41,65}

The crucial stage of crystal growth for forming anisotropic particles involves the structures being grown mostly in just one plane to form the nanowires, an important part in this is the presence of PVP. It is understood that PVP acts as a capping agent in this process and will preferentially bind to any (100) crystal facets of silver over the (111) crystal facets which are left open and this is where the successive crystal growth occurs with free Ag^+ ions and Ag^0 clusters attaching to the ends and conforming to the

defined crystal structure given by the seed particle.^{65,223,224} This process is understood to progress by Ostwald ripening with larger ready formed particles growing at the expense of smaller nuclei particles and free metal ions.^{95,219,225} The presence of PVP as mentioned before allows the silver crystals to grow in just one dimension and its role is demonstrated in figure 7.1.⁴¹

As these crystals grow further in one dimension to a rod or wire, their stability in solution decreases which in the PVP system the effect is lessened. This aids further controlled growth of primary particles by stepwise addition of atoms and ions, at the same time preventing coalescence of smaller particles resulting in secondary particles with less defined morphologies.

7.3.2 Seeds and Etchants

Use of pre-synthesised seeds is common for this method where near to monodisperse seeds are made prior in a separate reaction, and then added into the polyol system to provide a crystalline structure with defined crystal faces on which to grow with further in-situ produced small atomic clusters and ions.^{19,65,95,225} These pre-synthesised seeds don't necessarily need to be of the same metal of which the desired product will be, but the seeds will form a constituent part of the final particles.^{95,225} Commonly used seeds for the process of forming silver nanowires are silver, copper or platinum, and are made in relatively easy syntheses with high control over dispersity.

The addition of copper and platinum reagents in this reaction are not always just to function as seeds on which crystal growth occurs, but as a way to facilitate and increase the rate of this reaction. The work of Korte et al.¹³ describes the oxygen scavenging properties of added CuCl or CuCl₂ in the polyol process whereby Cu²⁺ is reduced by the solvent and reducing agent EG to its Cu⁺ state. The Cu⁺ then scavenges any adsorbed oxygen from the (111) face of the silver oxidising to Cu²⁺. The EG can keep reducing the Cu²⁺ back to Cu⁺ providing a constant etching of oxygen from the Ag surface allowing the nanowires to grow faster.^{13,19,226} This process of oxygen removal via Cu⁺ ions is shown in figure 7.2. The addition of Fe species has been studied in a similar way to

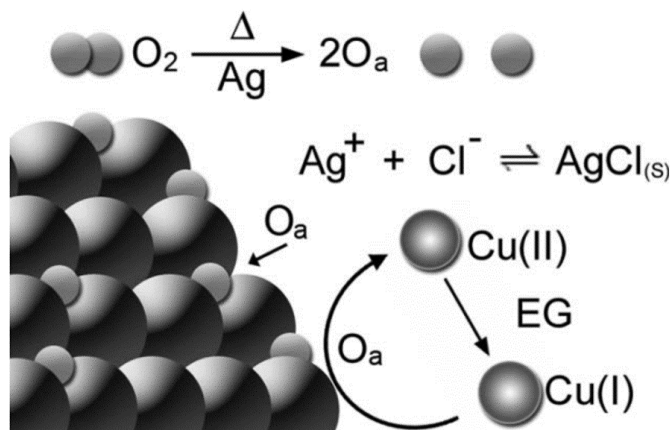


FIGURE 7.2: Diagram detailing the mechanism by which copper ions facilitate the growth of silver nanowires¹³

$CuCl$ and $CuCl_2$ as way of etching adsorbed oxygen from the (111) face of silver due to the (100) face being protected by PVP or other surfactant.²²⁷

It is not required that pre-synthesised seeds or oxygen scavenging reagents are used but they can greatly increase the yield and reduce the polydispersity of the product.^{19,216,221}

7.4 Experimental

To fit our aim of producing magneto-plasmonic nanorod structures, we have strived to co-precipitate nickel by modifying the well published route of synthesis for silver nanowires in EG.^{95,216} Nickel from several precursors had previously been shown to be able to be precipitate in polyol systems with or without additional reducing agents,^{22,92,228–231} taking advantage of the higher boiling point of polyols.

The coating of pre-formed silver nanowires by nickel and nickel oxide, with further post processing has been achieved and published previously.^{231?, 232} However, despite these known routes, it was thought it was of use to explore the potential of co-reduction of silver and nickel in a one-pot synthesis, without the use of harsher reducing agents such as $NaBH_4$ and $N_2H_4 \cdot H_2O$.

For this method the process pioneered by Sun et al. in 2002 was modified,⁹⁵ with aspects from other publications around this area of work.^{13,221} In short, all following reagents are added to a round bottom flask with reflux apparatus: 10 mL EG is heated to just shy of the boiling point (150–180°C) for half an hour, following with EG solutions of AgNO_3 (≈ 0.1 M), PVP (≈ 0.6 M), $\text{Ni}(\text{CH}_3\text{CO}_2)_2 \cdot 4\text{H}_2\text{O}$ (≈ 0.1 M) and CuCl_2 (≈ 4 mM). The metal precursor and PVP solutions were added to the pre-heated EG, injected at controlled rates of 5–20 mL/hr. After the reagents had been fully inserted into the reaction, the vessel was maintained at the reaction temperature for a further hour, at which point the reaction was allowed to cool to room temperature.

All factors in this chemical reactions were varied in attempt to find the optimal parameters. The variations made were: concentration and volume of reagents, relative precursor ratios, some precursors omitted, reaction temperature and ramp and injection rate of reagents. Some studies were also performed keeping all relative parameters equal but increasing the total volume of the reaction, to test any changes with batch volume.

Again the desired larger particles were separated from small nanocrystals, unreacted reagents and excess surfactants by following centrifugation washing steps used elsewhere in this project, and outlined in table 2.1.

7.4.1 Results and Discussion

Concurring with the existing literature, the optimal conditions found for the formation of nanowire morphologies were as follows: AgNO_3 (4 mL, 0.1 M), PVP (6 mL, 0.1 M), $\text{Ni}(\text{CH}_3\text{CO}_2)_2 \cdot 4\text{H}_2\text{O}$ (2 mL, 0.1 M) and CuCl_2 (160 μL , 4 mM) were injected to 10 mL EG at 160°C at a rate of 10 mL/hr. Additionally the temperature of the reaction was increased to 170°C and was held at this temperature for 1 hour following all reagents being added. This particular methodology resulted in the sample titled “NW46” and is referred to below. A summary table of all tested experiment parameters is included in Appendix C.

The use of CuCl_2 was found to greatly improve the generation of elongated morphologies in this system, by increasing the deposition rate of silver ions onto existing (111) silver

surfaces, and possibly by providing fine copper seed particles on which silver growth could proceed epitaxially.

Even with the addition of nickel precursors into the system, nickel nanoparticles or alloying of silver-nickel was not found with subsequent analysis.

XRD

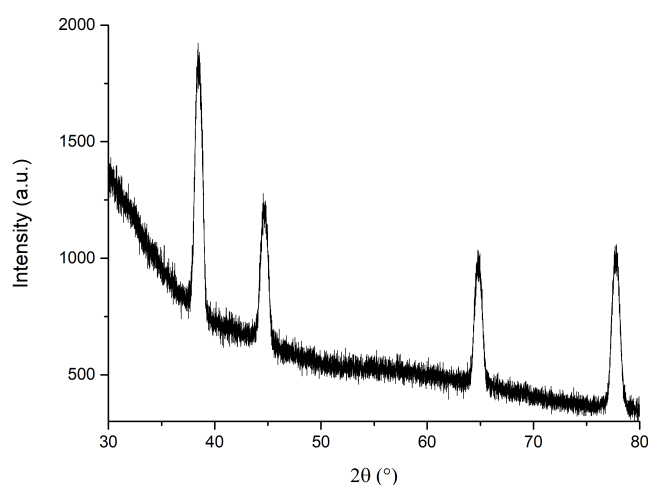


FIGURE 7.3: XRD data plot of sample NW46

Through XRD analysis of the NW46 sample produced in these experiments, a strong correlation of the data was found to published diffractograms of silver nanowires with PVP surfactant groups.^{216,224,226} These peaks are typical of single crystallite silver and thus confirm the material properties of the precipitate of this experiment,²³³ being both single crystalline silver particles with a face-centered cubic lattice structure. We find peak positions at 2θ values of 38.5, 44.7, 64.8 and 77.7°, which correspond to the crystalline planes: in ascending order; (111), (200), (220) and (311) of silver. The relative prominence of the (111) peak agrees with the analysis of PVP adsorbing to the (100) face encouraging further silver deposition and growth along the (111) plane as demonstrated

in figure 7.1. The synthesis of NW46 did involve a 33% fraction of nickel precursor to silver precursor, however in the XRD we see no presence of peaks; additional to the peaks attributed to silver, that would normally be attributed to either nickel, or nickel oxide.^{91,234,235} The peaks also appear reasonably sharp adding to the conclusion that just silver metal is present, as we would expect some broadening of peaks if nickel was to be alloyed with the silver in low amounts.²³⁵

Raman

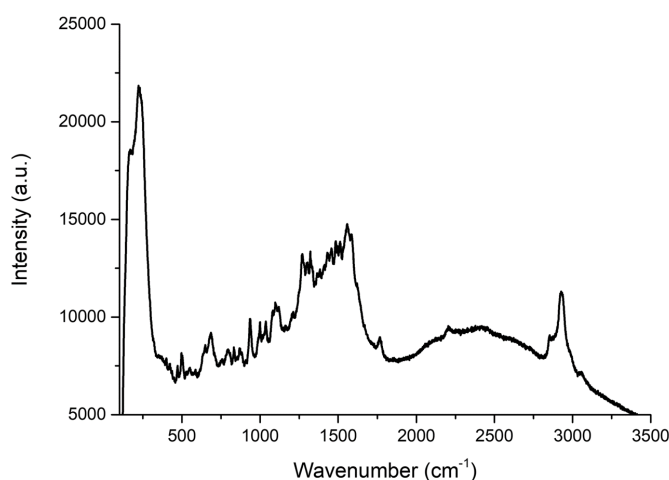


FIGURE 7.4: Raman spectra of sample NW46

Raman spectroscopy analysis performed on sample NW46 resulted in spectra very closely matched to published data of a similar procedure producing silver nanowires.²²¹ Our spectra shown in figure 7.4 has prominent peaks at 2933, 1556, 1322, and 222 cm^{-1} . It is thought that the peaks present in this spectra are actually from the PVP surface capping molecules bound to the silver particles' (100) surfaces, due to the Surface Enhanced Raman Spectroscopy (SERS) effect, where the silver nanoparticles are acting to enhance the spectra of PVP.^{221,236} This strong enhancement of the PVP spectra confirms the close proximity of PVP to the silver particles' surface, and the strong or weak enhancement

of certain peaks can help to resolve how PVP is arranged at the silver surface. The peak at 222 cm^{-1} which is not in PVP spectra, represents the Ag-O stretching vibration showing the carbonyl group of PVP is responsible for its coordination to silver through nonbonding electrons on the oxygen atom. This is backed up by the enhancement of 1556 cm^{-1} peak assigned to the stretching vibration of C=O, again indicating the close proximity of carbonyl group to silver. We also see an enhancement of the peak at 2933 cm^{-1} from the standard PVP spectra, which is linked to asymmetric stretching of CH_2 indicating the alkane chain is close to the surface of the silver particles.

Electron Microscopy

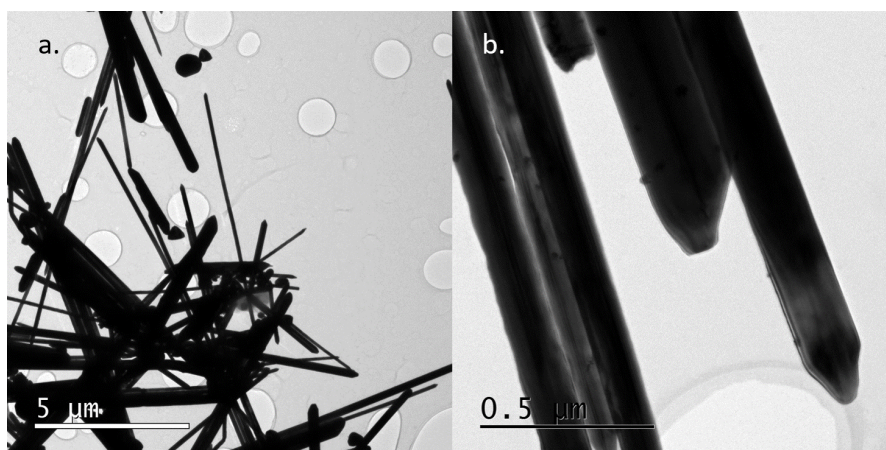


FIGURE 7.5: HRTEM images of sample NW46

Through TEM analysis of our produced particles, in particular sample NW46, we see the typical well defined nanowire shapes of silver metal. These particles have a precisely characterised morphology and structure in the literature,^{12,223} with a five sided geometry extending along the (111) plane. The nanowires synthesised in sample NW46 range from 2–10 μm in length, and a width of approximately 100 nm. In some instances the wire particles are seen to bundle together, while the yield of particles in this experiment is not completely wire morphologies, with some platelets and other structures present. HRTEM-EDX mapping of sample NW46 also confirmed the absence of nickel in the

produced particles despite nickel precursor being added to the reaction (figure D.3 in Appendix D).

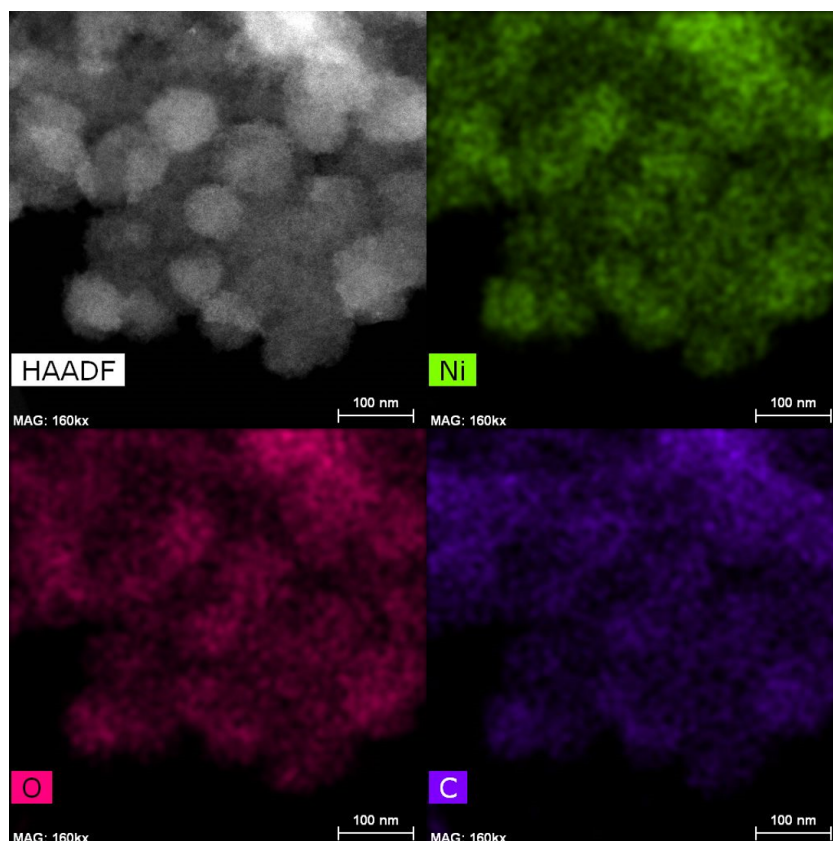


FIGURE 7.6: HRTEM-EDX mapping of particles formed by reduction of nickel precursor

A test was made to try and reduce only $\text{Ni}(\text{CH}_3\text{CO}_2)_2 \cdot 4 \text{H}_2\text{O}$ in ethylene glycol to test its applicability in this study. The resulting precipitate shown in figure 7.6 by HRTEM-EDX mapping indicates the resulting particles are an amorphous nickel oxide compound, while some crystalline particles were also seen elsewhere (figure D.4 in Appendix D). However further analysis into this needs to be performed to fully qualify the reaction products.

7.5 Conclusions

The polyol process investigated in this section proved a very delicate synthesis method, where slight changes in methodology resulted in great differences in the reaction product. Using a combination of several published methods for producing silver nanowires, combining the key variables from each we could also produce wire morphologies of silver. It was, however, not possible to co-deposit nickel with the silver as was desired. Further work into this method to fully designate the compounds in solution responsible for the reduction of metal precursors should be performed, and extending from this the use of other polyol solvents could be explored, alongside possible introduction of other more potent reducing agents. Subsequent growth of nickel or nickel oxide on the silver nanowires could also be explored using an alternative secondary coating step.

Chapter 8

Cobalt Nanorods Synthesised by Hydrogenation Reduction

8.1 Introduction

Cobalt metal is easily oxidised even just by oxygen in the air, as such when aspiring to produce cobalt particles dry conditions must be used and synthesis routes not using aqueous solutions. In recent years cobalt nanoparticles have been prepared using hydrogen gas as the reducing agent with precursors dissolved in organic or anhydrous solvents,^{96–99} or just as solid precursor.²³⁷ The cobalt precursors hence have typically large ligand structures with oligophilic regions to allow them to be solute in organic solvents, they are not easily available compounds and relatively expensive. Usual cheap halide metal salt precursors also cannot be used, as they will often contain water such as $\text{CoCl}_2 \cdot 6\text{H}_2\text{O}$.

Synthesis methods previously published on this topic again require the presence of a kind of structure directing agent or surfactant to attain nanorod shaped particles.^{96,97,238} Lauric acid (LA) or dodecanoic acid (DDA), and hexadecylamine (HDA) are some such surfactants used in these processes. Auspiciously a phase transfer mechanism has been published for the transfer of transition metal ions from the aqueous phase to the organic phase, using LA.²¹⁰ A combination of these two processes has been experimented with to try and find a new route to the synthesis of cobalt nanorods, from an easily available cobalt precursor.

Many of the publications then include a further step of coating the cobalt nanorods with a metal that is harder to oxidise, so that the particles can be stored or used in aqueous media. Typically gold, platinum and tin have been used for this coating purpose. This would provide the optical properties of an anisotropically shaped particle we have strived for throughout this project, while the cobalt core, being strongly magnetic, providing the magnetic properties required.

The cobalt nanorods produced in these inert atmosphere syntheses are closely matched in shape and size to candidate particles in several theoretical and computational publications on the use of magneto-optic particles in some diagnostic system.^{57,58}

8.2 Experimental

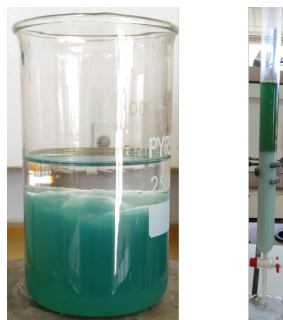


FIGURE 8.1: Images showing phase transfer step of cobalt ions from aqueous to organic solvents

This process was commenced with the phase transfer method.²¹⁰ Starting with $\text{CoCl}_2 \cdot 6\text{H}_2\text{O}$ (0.24 g, 20 mM) dispersed in 50 mL DI water and subsequently added to an equal volume of IMS with 20 mL solvated hexadecylamine (HDA), this is presented in the left image of figure 8.1 with a clear solvent phase sitting above the cobalt precursor aqueous solution. The mixture was stirred for some minutes and slightly heated at 50°C to keep the HDA from solidifying, at which point an equal volume of toluene to the aqueous phase was introduced, with stirring continued. As the toluene is added, a clear transition from the aqueous to organic layer is seen of the green-turquoise colour, within moments. This proceeds through HDA's clear preference to existing in the organic solvent, however is soluble enough in IMS through high polarity, to first complex with the cobalt ions present in aqueous phase.

The coloured toluene phase is then taken to contain Co-HDA complex, due to the observed phase transition, while no other phase transfer agents are present in solution. A qualitative phase transfer (<95%) is assumed and so the desired mass of molar mass of cobalt ions in the hydrogenation reduction step is introduced to the initial phase transfer process.²¹⁰

The green coloured toluene phase is then separated from the aqueous phase by use of a separating funnel, seen in the right hand image of figure 8.1.

This solution of Co-HDA in anhydrous toluene is then used in a secondary step. This step uses heating and hydrogen gas to reduce the cobalt precursor to surfactant coated metal particulates.⁹⁹ Some variations were made on the following method, such as reaction temperature and relative amount of HDA to lauric acid (LA).

The volume of Co-HDA in toluene from the phase transition step was measured, and made up to a total volume of 20 mL with anhydrous, degassed toluene in a Fisher-Porter pressure vessel. To this an amount of LA is added and stirred to dissolve, and the vessel is sealed shut. The vessel is heated in an oil bath to 170°C, while the vessel is purged with N₂ multiple times, and then purged with H₂ two times and then charged to a pressure of 3 bar with H₂. This mixture is held at this pressure and heated with constant stirring for 48 hours. A black precipitate is resulting, indicative of cobalt metal or cobalt oxides.

The precipitate was washed through centrifuge washing steps, consisting of two 20 minute spins in fresh degassed anhydrous toluene, then stored in anhydrous toluene to attempt to limit oxidation of the cobalt metal, prior to analysis.

8.2.1 Results and Discussion

Sample 24 was prepared as explained above, with 200 mg of LA added to solution prior to heating in hydrogen reduction step, the vessel was purged with N₂ and H₂ gas then pressurised again to 3 bar with H₂ after 24 hours of heating. Sample 29 was prepared as detailed above, with the one caveat that 400 mg of LA (double that of sample 24) was added to solution in this case. Additionally the vessel stayed sealed with 3 bar H₂ the whole 48 hours of heating.

Electron Microscopy

Sample 29 had double the amount of LA acid added into the hydrogenation step than sample 24, and as can be seen in figure 8.2 this resulted in the formation of cubic nanocrystals. In contrast to sample 24 with less LA in solution, where longer rod shaped particles are formed.

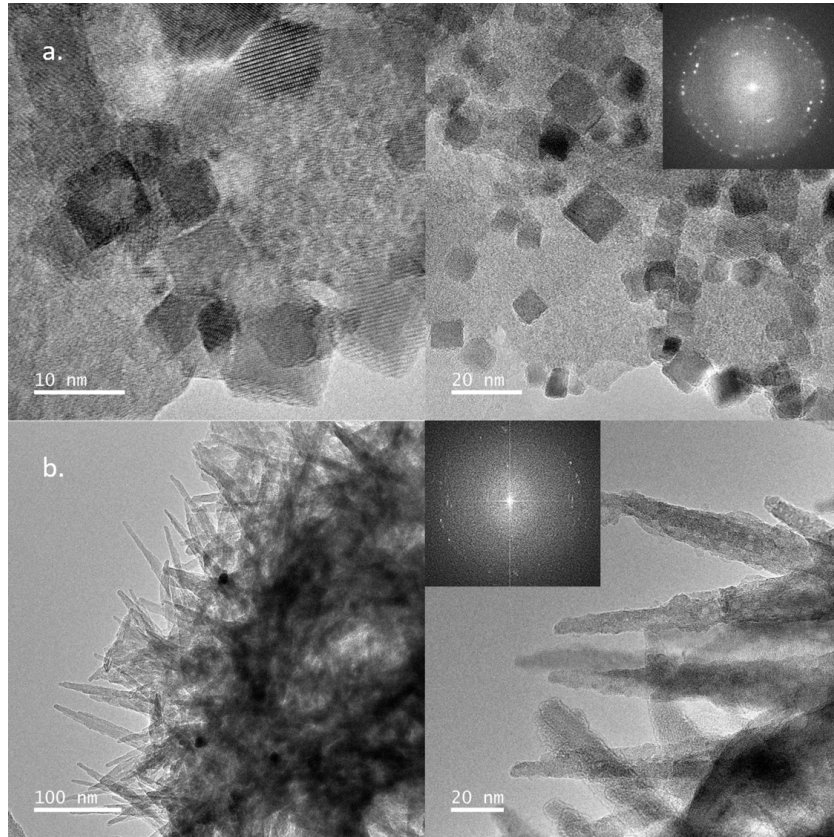


FIGURE 8.2: HRTEM images of cobalt and cobalt oxide nanoparticles formed after hydrogenation reduction reaction, with inset electron diffraction pattern, row a. is of sample 29 and row b. shows sample 24

The cube shapes formed indicate the presence of various Co, CoO and Co_3O_4 lattice planes when interpreting the electron diffraction patterns from the HRTEM images in figure 8.2. Lattice interference measurements of 0.2214, 0.1856, 0.4216 and 0.2615 nm were measured, and match closest to the following calculated lattice planes and crystal structures in order: (100)/(010) of cobalt, (210) and (100) of CoO, and (210) of Co_3O_4 . It is assumed that oxidation of certain planes may have occurred after synthesis, despite best efforts to store in anhydrous environments. The cube nanoparticles vary in size between 13.5 and 6 nm length edges. The greater availability of LA in solution must hinder the growth of the cobalt nanoparticles in certain directions, counterbalancing the

existing presence of HDA in solution following the phase transfer step.

The longer rod shape particles seen in sample 24 and in figure 8.2 row b. were equally not well dispersed and looked to be half embedded in some amorphous material, just as in sample 29. This factor makes measuring the dimensions of the rod shaped particles more difficult. The length of the rods is estimated at between 70 and 200 nm, with a width of about 8-16 nm, giving the particles an aspect ratio of between 8.75 and 12.5. The observed lattice spacings in these HRTEM images match best to cobalt oxide miller indices. 0.4713, 0.4638, 0.3109, 0.27, 0.2401 and 0.2331 nm lattice spacings were measured, but the first two could not be linked to any calculated lattice spacings of cobalt or cobalt oxides. A measured lattice spacing of 0.3109 nm is likely attributed to the (110) plane of CoO, while the remaining spacings of 0.2401 and 0.2331 nm correspond to the (211) plane of Co₃O₄ and 0.27 nm corresponds to the (210) plane of Co₃O₄. No lattice spacings from this sample could be linked to interplanar distances calculated for cobalt metal, this again could well be due to oxidation of the precipitate occurring after synthesis prior to analysis.

8.3 Conclusions

Through this brief study we have found it possible to conduct a phase transfer step of aqueous soluble cobalt ions into anhydrous toluene via use of a phase transfer agent (HDA), and then use this Co-HDA precursor directly in a hydrogen reduction process. Further analysis of the phase transfer product should be conducted to characterise the compound as Co-HDA, and also to quantify the efficiency of this step. While precise shape control of the formed particles was not realised in the second hydrogen reduction step it is anticipated that this route could match other publications on morphological control, while using more easily attainable cobalt precursor compounds. The protection of cobalt metal by further deposition of gold should also be performed to maintain the formed cobalt metal structure and its desirable strong magnetic properties.

Chapter 9

Pickering Emulsions

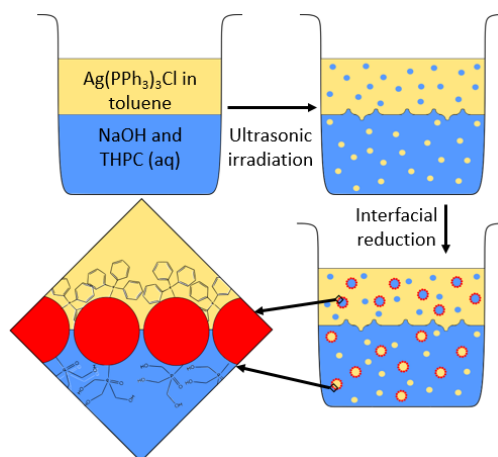


FIGURE 9.1: Schematic illustration of the Pickering emulsion synthesis scheme with silver precursor.

9.1 Introduction

Emulsions are defined as the mixing of two immiscible liquids that form a stable colloid in the presence of a surfactant, commonly these are molecular surfactants that tend to have a hydrophilic and oligophilic constituent. These are found in many applications and uses such as paints, milks, medical applications and others. The key difference with Pickering emulsions are that these colloids are stabilised by solid particulate surfactants.^{100,239–241} The juxtaposition of these two emulsion types is presented previously in figure 1.11. This attribute to Pickering emulsions can bring new functionalities to emulsions that do not originate from molecular compounds dispersed in either the water or oil phase, but from the solid surfactants themselves.

The justification of how these emulsions can be stabilised by solid particles can be drawn from Gibbs free energy equations 6.1 and 6.2 discussed in section 6.1. Through these Gibbs equations it has been proven that stability of Pickering emulsions can actually be of a few magnitudes greater than regular emulsions stabilised by molecular surfactants.^{201–203,239,240}

9.2 Experimental

Pickering emulsions have been produced in a one-pot reaction of molecular precursors and reducing agents solvent in opposing phases. As the reducing agent is introduced, initiating the reaction, then the whole reaction vessel is subjected to ultra-sonic radiation which agitates the interface of the two phases creating countless droplets of each phase dispersed in the other. During this agitation of the interface, the molecular precursors are being reduced resulting in metal ions and clusters which then increase in size by crystal growth. Due to the reagents only being in proximity to each other at the fluid boundaries then these metallic seeds are again first produced in close proximity to the interface. As the metal seeds grow then the reduction in interfacial tensions will increase driving the reaction to form nanoparticles adsorbed to the interface.

An example reaction proceeds as 1 mL of 18.43 mM $\text{NaOH}_{(aq)}$ and 5 mL of 0.6445 mM of either $\text{Ag}(\text{PPh}_3)_3\text{Cl}$ or $\text{Au}(\text{PPh}_3)\text{Cl}$ in toluene are introduced in a vial. Then 0.12 mL of 50 mM $\text{THPC}_{(aq)}$ is injected into the vial, which is sealed and then placed into an ultra-sonic bath for 60 minutes where the water is kept between 15-20°C.

The reduction of metal salts by THPC is initiated in the same manor as demonstrated in equation 4.1, whereby THPC is hydrolysed to form formaldehyde which can reduce the salts, resulting in metal ion and cluster formation, which grow by further crystal growth.

9.2.1 Results and Discussion

This process has shown its ability to produce stable emulsions stabilised by nanoparticles synthesised in-situ of phase mixing. This has been simply demonstrated by dispersing dyes insoluble in either organic and aqueous phases, and showing their presence throughout the prepared emulsion. This property is exhibited in figure 9.2, whereby image a. shows the incorporation of a red ink dye which normally only disperses in aqueous solutions as shown in the vial on the left. However the right-hand vial of image a. (9.2) a Pickering emulsion preparation clearly shows the red dye is also now present in the top toluene layer, indicating how droplets of water containing the red dye must be dispersed

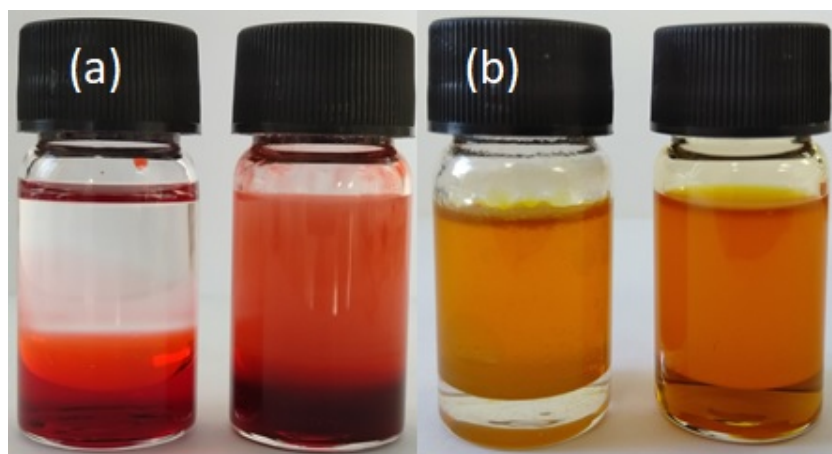


FIGURE 9.2: Pickering emulsions prepared with silver nanoparticles by the method detailed with phase soluble dyes to demonstrate presence of emulsions, in each image the left vial contains no THPC hence no emulsions formed and both right vials were prepared as normal with THPC. Image (a) shows an aqueous soluble red dye, with image (b) showing a lipophilic solvent dye

in this phase. The opposing dispersion of toluene droplets within the aqueous layer has also been demonstrated here in image b. of figure 9.2. This was performed by incorporation of the organic solvent dye 2-Aminoazotoluene or “Solvent Yellow 3”, with high solubility in toluene while insoluble in water. Again the vial on the left of image b. 9.2 shows the dye only dispersed in the preferred phase while no emulsion is present, while when the dye is added to a Pickering emulsion on the right hand vial the dye is seen to be present throughout the two phases, indicating dispersed droplets of toluene within the water layer.

It can also be observed in figure 9.2 that there is an obvious difference between vials with and without Pickering emulsions, this is the apparent flattening of the interface between the two phases. Two immiscible liquids or phases usually form a curved meniscus where they meet due to interfacial tensions between the two phases. However due to the inherent nature of Pickering emulsions which involves the adsorption of solid particles to the interface to enact a reduction in interfacial tension, this likewise results in a reduction of surface tension between the two majority phases that are still present, resulting in a

flattened interface.

Optical Microscopy

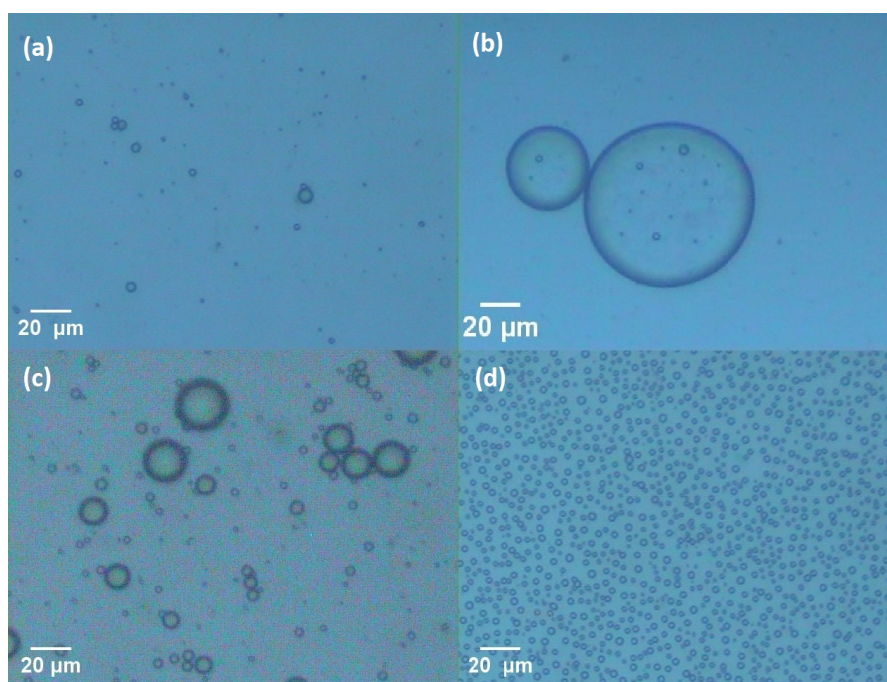


FIGURE 9.3: Photographs showing droplets of oil present in the majority water layers. Image (a) shows freshly prepared emulsion with silver, opposed to (b) which is imaged 3 months after initial preparation. Images (c) and (d) show Pickering emulsions prepared with gold nanoparticles, freshly made and aged 1 month respectively.

Using a digital microscope setup the presence of toluene emulsion droplets in the aqueous layer was studied at various time points, while subsequently droplet sizes were measured from the images to study any changes with ageing. The microscope images in figure 9.3 are representative of the emulsion droplets observed in the aqueous layer, stabilised in two cases by silver and gold nanoparticles separately, while freshly prepared and aged for 1 month or over. Unfortunately, due to the intense lighting used in the microscope system analysis of water emulsion droplets dispersed in the toluene majority layer was

not feasible as the solvent evaporated rapidly, however the presence of water in toluene emulsion was evidenced and discussed above in figure 9.2.

Images a. and b. of figure 9.3 present emulsions stabilised by silver nanoparticles, freshly prepared and at 3 months after preparation. Some much larger droplets are present in the aged sample which are not observed in the fresh sample, while the presence of similarly sized small droplets are also still maintained in the aged sample. This size dispersion of measured droplets are exhibited in figure 9.4 with fresh emulsions exhibiting droplet sizes largely between 0.5 and 4 μm diameter, however the presence of much larger diameter droplets (of around 85 μm) in the aged sample indicates the flexibility and stability of this nanoparticle stabilised emulsion. It is also seen in the 3 month aged sample that there are double emulsions, i.e. within the largest toluene-in-water droplet, there are further droplets which must then be water-in-toluene droplets.

The emulsion droplets seen in images c. and d. of figure 9.3 are alternatively prepared with gold nanoparticles. Interestingly in this sample it seems that up to one month after the emulsion is prepared, a focussing of droplet sizes is observed. Freshly prepared emulsion presented in image c. shows a range of droplet sizes measured to be between 1 and 27 μm but the distribution of these droplet sizes presented in plot c. of figure 9.4 is largely centered at about 5 μm diameter. After 1 month of ageing all the droplets measured had a diameter of between 1 and 4.5 μm with the average droplet size being slightly less than 3 μm .

Electron Microscopy

The nanoparticles in-situ synthesised of the emulsion preparation have been analysed by HRTEM to study the nanoparticle sizes and morphology. The nanoparticles were extracted from emulsion by centrifugation of the whole sample, both water and toluene majority phases, retaining the precipitate. The precipitate was then dried in an oven at 80°C and then dispersed in IMS for deposition to TEM grids for analysis. Displayed in figure 9.5 image a. shows the gold nanoparticles formed in a freshly prepared Pickering emulsion with in-situ reduction of the gold precursor. The particles are all spherical

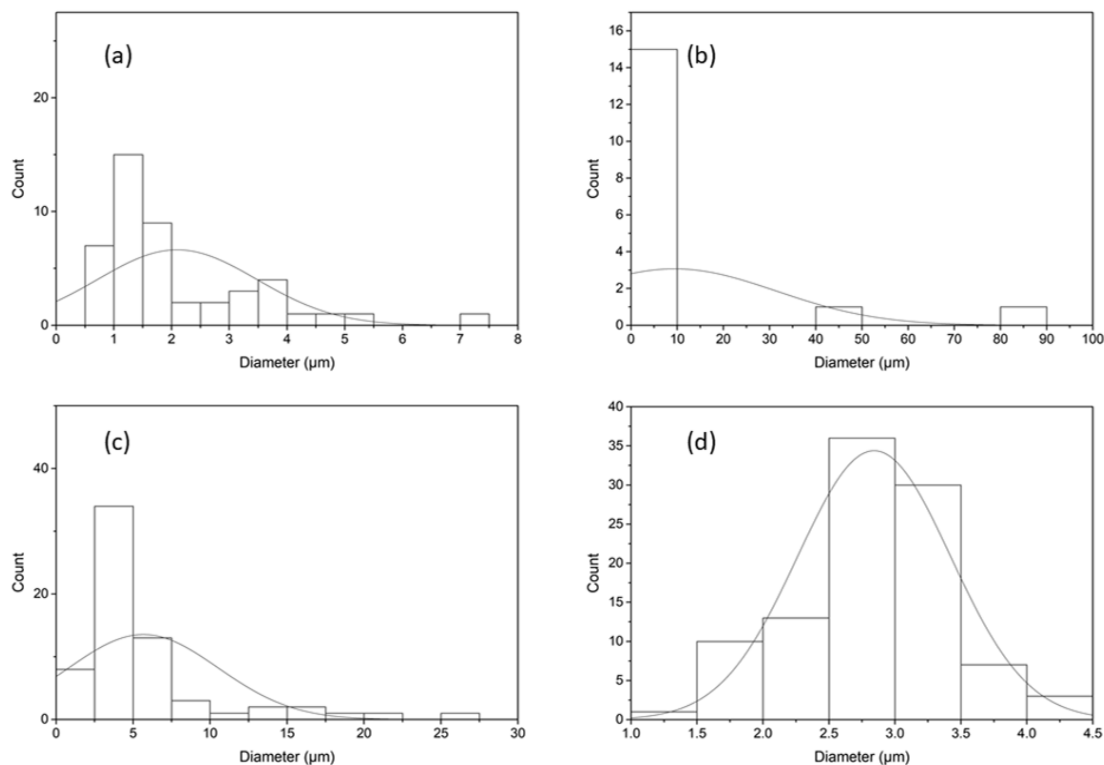


FIGURE 9.4: Histogram plots of droplet diameter size form fresh and aged samples of Pickering emulsions stabilised with silver and gold nanoparticles, plots a., b., c. and d. are measured from droplets seen in the relevant images seen in figure 9.3

with small sizes of around 1 to 4 nm diameter, which matches typical nanoparticle sizes of gold reduced by THPC, for example by the Duff method.¹⁷⁷

Image b. in figure 9.5 displays silver nanoparticles isolated from a freshly prepared Pickering emulsion with the aforementioned particles, with an additional inset image of the particles isolated from a 3 month aged emulsion. The sample from fresh emulsion demonstrates the largely spherical morphologies with diameters of 10 to 13 nm. Interestingly nanoparticles taken from the aged emulsion indicate the presence of much larger silver nanoparticles, with some undefined morphologies, while small nanoparticles like those in

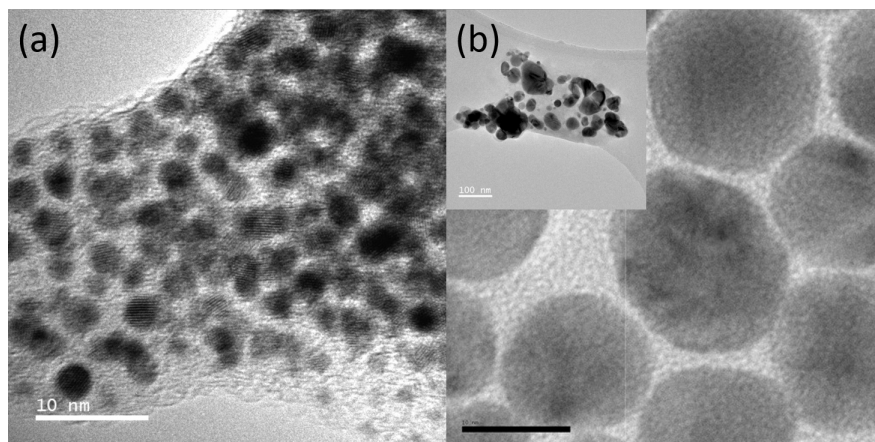


FIGURE 9.5: HRTEM images of nanoparticles synthesised in-situ of Pickering emulsion preparation. Image (a) shows as formed gold nanoparticles, with image (b) showing silver nanoparticles with an inset image of the nanoparticles after 3 months of ageing in emulsion condition. The main images a. and b. both have scale bars of 10 nm

the fresh preparation are still present. The largest particles in this aged sample are up to 100 nm in diameter, indicating a growth of 10x. The growth of these nanoparticles can be understood as all reaction products and reagents are present in solution through ageing, while we can link the presence of larger droplets observed in the aged solution in figure 9.3 image b. to the presence of larger nanoparticle stabilisers, as there has been some discussed relationship between the size of solid surfactants and the resultant droplet size.¹⁰⁰

By putting in the nanoparticle diameters measured and discussed above for gold and silver, the reduction in interfacial energy due to the particle adsorption to the interface could be approximated through the use of equation 6.1. The value of γ_{wo} was taken to be 0.036 Nm^{-1} ,²⁰¹ while θ is set to 90° . Using 3 nm diameter for gold and 12 nm for silver values of interfacial energy reduction due to nanoparticle adsorption was calculated to be 250 and 4000 $k_B T$ respectively, which is drastically larger than thermal energy in solution at room temperatures.²⁰³ These adsorption energies are also much larger than values for typical surfactant molecules used for standard emulsion preparations (in the region of 10 $k_B T$),^{100,105} making these solid stabilised emulsions highly stable.

Nuclear Magnetic Resonance Spectroscopy

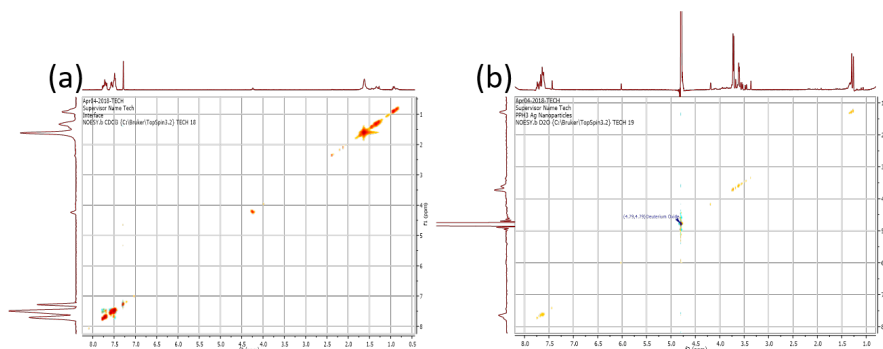


FIGURE 9.6: ^1H NOSEY 2D NMR spectra of (a.) silver nanoparticles produced at the interface of toluene and water, and (b.) silver nanoparticles synthesised with the same reducing agents, however solvent in a mix of CH_3OH and H_2O

The nanoparticles of silver formed in this Pickering emulsion preparation were also studied by 2D proton NMR, which is presented in plot a. of figure 9.6. Multiplet peaks centered at 7.69 ppm is attributed to the proton environment in PPh_3 , while similar peaks at 1.31 and 0.97 ppm corresponds to the oxidation product of THPC; THPO. 2D NOSEY NMR analysis in theory allows for the interpretation of surface groups that are present in very close proximity (less than 5\AA) to each other through cross-coupling.¹⁸² In our case no off-diagonal peaks are observed in the 2D plot which would indicate that the stabilising surface ligands of PPh_3 and THPO are present in separate faces of the nanoparticle in a Janus particle configuration.

We also prepared silver nanoparticles with the same reducing agents and precursors, however just in aqueous solution. This is presented in plot b. of figure 9.6 where multiplet peaks attributed to both PPh_3 and THPO are observed, however again there is an absence of off-diagonal peaks caused through cross-coupling of surface groups in close proximity. This would be expected in this case with a distribution of these surface groups being evenly spread on the nanoparticles, due to there being no driving arrangement factor from the particles' environment such as the presence of oil. This result throws into dispute the effectiveness of this study to resolving the surface arrangement of the

hydrophilic or hydrophobic groups, or that the surface coverage of ligands in this case is lower than previous studies of gold nanoparticles;¹⁸² meaning that neighbouring surface groups are more than 5\AA away from each other and hence no evidence of interactions.

9.3 Conclusions

These brief studies have further proven by extension the applicability of equation 6.1 for adsorption of nanoparticles to an interface, and thus in-situ synthesis of nanoparticles alongside mixing of a two phase system resulting in long term stable emulsions by reducing interfacial energy of the two immiscible phases.

This simple modification of a gold and silver nanoparticle thin film deposition process, has resulted in Pickering emulsions with the as formed nanoparticles acting as solid particulate surfactants. The reaction mechanism produces PPh_3 and THPO from reduction and oxidation of the metal salt and reducing agent respectively, which in turn are able to act as surface ligands on the precipitated nanoparticles providing hydrophobic and hydrophilic properties simultaneously allowing for preferential adsorption to the interface of toluene and water.

Chapter 10

Conclusions and Future Work

The set aims of this project have been addressed by various methods, and the resulting nanoparticle properties are analysed through a suite of analysis techniques. Further work could help to build a more detailed picture of these procedures and to tune the methods to ensure their reciprocity and value, and some such prospective avenues are ruminated here.

Starting with chapter 2: structural and material analysis was made on spindle shaped iron oxide particles that were synthesised by the process first pioneered by Matijevic et al.,⁷³ and subsequently the subject of studies by many groups globally.^{59,111,115,116,148} Concurring with these studies we find that the particles first proceeded via forced hydrolysis from the FeCl_3 precursor forming $\beta\text{-FeOOH}$ nanorod particles up until around 24 hours of heating. Past this point with further heating it seems that $\alpha\text{-Fe}_2\text{O}_3$ is formed at the expense of akaganeite in solution, while it has been theorised that the transition from akaganeite to hematite can proceed when close bundles of these sub-units are closely aligned making the transition more favourable. The final formation of the hematite form of iron oxide was qualified by XRD, Raman, electron microscopy and TGA analysis.

The study of a large population of the particles (593) formed after 72 hours heating confirmed that the synthesis process produces well defined spindle shaped particles with tight size dispersion. The tighter the size control of the synthesised particles will, after subsequent coating procedures; result in a more acute optical resonance of the particles. This is of importance if the proposed system of use for the magneto-optic reporter particles is to be multi-plexed, it is hoped that individual populations of particles can be monitored by their discrete optical resonances. VSM analysis of the hematite nanorice confirmed the expected magnetic properties of these particles, as being weakly ferromagnetic. The limitations of the equipment used (lack of field strength >0.4 Oe) meant that magnetic saturation of the material was not observed, but just a weak hysteresis is detected indicating some remnant magnetisation of the particles; which would not be seen for a super-paramagnetic material.

Further work in this area would primarily base on attaining more comprehensive magnetic analysis of the material, and to experimentally study the particle sizes and size dispersions for different reaction times and phosphate to iron precursor ratios.

In chapter 3 a co-precipitation method was discussed as a route to dope the prior discussed hematite nanorice particles with various transition metal ions. This was achieved through simple modification of the forced hydrolysis method that was performed in chapter 2. Through the introduction of metal salts of nickel, cobalt and copper at low relative proportions to that of the iron precursor salt it was found that these select transition metals could be doped into the hematite structure, while maintaining the morphological control over the produced particles with KH_2PO_4 addition.

The successful incorporation of these metals into the hematite particles was demonstrated by XRD and Raman analysis, which generally found a slight contraction of the crystal lattice upon doping due to the relatively smaller ionic sizes when compared to that of iron species in hematite. Additionally the maintained shape control of the synthesis method was proven through electron microscopy studies, however it is thought that the resulting particles are not quite as well defined and there is greater variation in size and shape than those from the undoped hematite synthesis method. Despite this reduced size control, it was found that the nickel doped hematite particles in particular showed a large improvement in sensitivity when used to detect changes in solution viscosity, when compared to the undoped hematite particles.

Subsequent work on these formed particles would be able to further qualify the magnetic properties to a greater extent, while experimental work should try to further tune the process to maintain the tight size control of the original procedure, establish the maximum extent of doping possible, and to study the efficacy of these particles to be later coated with noble metals by the processes discussed in chapters 4, 5 and 6.

Chapter 4 hosted a broad discussion of the many varied approaches to attaining core-shell morphology particles, and more specifically the published routes to coating noble metal particles on a base or core of iron oxide materials. It was also described the method followed in this study of immobilising noble metal seeds on the hematite core to perform further shell growth steps.

Demonstrated in this chapter is that gold nanoparticle attachment to hematite cores through APTES functionalisation gave a more dispersed coating of particles than when repeated with silver nanoparticles, this is probably due to the size dispersity of the

nanoparticle seeds being attached (gold more monodisperse than silver). Much further work could be done in this region of study such as: optimising the APTES coating of the hematite core, narrowing the size dispersion of nanoparticles being used for attachment to the core particle, and to explore other attachment routes other than APTES; such as the ones described within the chapter. A good candidate for this would be to explore deposition of a silica shell on the hematite core to provide a smoother surface, with subsequent APTES functionalisation in anhydrous solvents and then nanoparticle coating. Other analysis such as X-ray Photoelectron Spectroscopy (XPS) would also add to this study showing the binding of relevant groups (hematite-APTES, APTES-gold/silver) and informing of their successfulness.

Introduced in chapter 5 is the nanoparticle size processing method titled “digestive ripening”. This method has a proven record of tuning and narrowing the size dispersion of nanoparticle colloids by gentle heating with some digestive ripening agent; or ligand, which can etch portions of metal material from the largest particles in solution, subsequently adding onto the smallest particles growing their mass and narrowing the range of particle size or mass over the whole population.

This low-temperature process has proven able to produce alloyed and well mixed shells of gold and silver, coated on a hematite core structure. This has meant that the optical resonance of the core-shell particles can be tuned by adjusting the proportion of gold to silver, while the best coatings were produced with just, or in higher proportions of, gold. The use of gold seeds over silver was also found to give a better surface density of coatings. Further work on this study should explore the other options for alternative digestive ripening agents, such as thiol functional molecules, introduction of another metal precursor, or to apply the digestive ripening process to the seed nanoparticles first deposited onto the core particles. The question of subsequent coating steps could also be approached, while it may be interesting to study whether the presence of seeded core particles is necessary to forming a shell. Further analysis of the particles such as extended UV/Vis spectra could enable a monitoring of the longitudinal plasmon resonance of the core-shell particles, while XPS would show such details as gold binding to APTES coated particles, and possibly the action of the digestive ripening agents bonding to nanoparticle surfaces.

The nanoparticle coating process discussed in chapter 6 explored the use of a two phase liquid system of synthesising thin films of nanoparticles, but for the deposition of noble metals on core particles suspended at the interface. This secondary coating process was shown to be successful using a slightly modified method, resulting in some conditions with good surface coverage and controlled optical properties. The variables in this method could further be explored to achieve even better coatings, with subsequent coating steps presenting an obvious option to improve deposition with. Work could also be performed on better retainment of core-shell nanoparticles from the interface after reaction, using some phase transfer agent or the like. The core-shell particles produced through this method have proven to function well as reporter particles in the prospective magneto-optic diagnostic system, all being able to signal changes in solution viscosity adequately, while it seems that the particles with largest shell growths saw some slight reduction in sensitivity in this case.

A well known route for synthesis of high-aspect ratio silver nanowires was explored in chapter 7, while the co-precipitation of these structures with nickel metal was examined. This process proved to be a delicate balance of factors, as the breadth of literature indicates. While silver nanowire particles were produced, the simultaneous reduction of nickel nanoparticles was not evidenced after analysis of the precipitates by XRD, HRTEM and Raman techniques. Further work in this region could look at other solvents which may be more amenable to nickel reduction, or to other subsequent methods which could be used to coat the silver nanowires with nickel. Oxidation of nickel metal may however prove to be an issue in all cases, and more strict storage protocols could be introduced.

Nevertheless, the experimental work here concluded with many separate publications on factors that improve the growth and yield of high-aspect ratio particles, such as temperature, injection rate, reagent ratios and presence of metal halide salts.

Chapter 8 introduced a relatively newer nanoparticle synthesis method, for forming well defined cobalt nanorods by hydrogen reduction in anhydrous conditions. A variation of a published phase transfer mechanism allowed us to explore the application of other cobalt precursor compounds in this synthesis method. It was demonstrated that phase transfer of cobalt ions from aqueous solution to toluene with HDA, could then be used as

a precursor in the subsequent hydrogenation step. It was found by variation of the ratio of HDA to LA added in the hydrogen reduction step affected the shape of the produced cobalt structures.

Subsequent study should work on finessing this technique, possibly by first removing any excess HDA from solution so the ratio of particle surfactants can be better controlled. Subsequent coating of the cobalt core with tin and gold metals should also then be examined to prevent oxidation of cobalt. More detailed analysis of the produced particles should also be made, such as XRD crystallography and Raman spectroscopy to confirm the material's structural properties, and some magnetic analysis such as VSM.

The final additional chapter 9 goes further into exploring the dynamic system of liquid-liquid interfaces, and the use of in-situ synthesised nanoparticles to stabilise emulsions of two liquids. By the adaptation of a published method for the preparation of gold and silver thin films at the interface of toluene and water, Pickering emulsions were produced displaying significant stability.

By the reaction of reagent compounds in opposing phases and constant irradiation by ultra-sound energy, nanoparticles formed at the interface and stabilised by both hydrophilic and phobic surface groups stayed adsorbed to this interface after reaction was complete. The formed nanoparticles of gold and silver were found to be of reasonably tight size dispersions of around 10-13 nm diameter particles of silver and 1-4 nm diameter particles of gold in freshly prepared emulsion. However, in the case of an emulsion with silver nanoparticles prepared 3 months prior, the size and dispersity of the particle sizes had increased dramatically. Further analysis of droplet sizes should be explored for this method using a technique such as Dynamic Light Scattering analysis, while the simultaneous precipitation of gold and silver in this process could be explored, and the nanoparticle stabiliser growth alongside emulsion ageing mechanism could be studied with more detailed chronological studies. Studies with XPS could also shed more light on the stabilising ligand environment on the nanoparticle surfaces.

All aspects of this project have strived to manipulate the optical and magnetic properties of high-aspect ratio nanoparticles that would be stable in aqueous environments, through

the use of various chemical synthesis methods, and the successes of such methods have been presented.

Optical resonance properties have been influenced by surface coverage of core particles with gold and silver nanoparticles, and the relative proportions of these two plasmonic materials. Alternative rod or wire particle preparation methods were also explored which would have inherently different optical properties due to size, morphology and structure differences. Magnetic properties of the anisotropically shaped nanoparticles have also been affected, by doping of hematite core particles with other transition metal ions, while the use of other rod shaped nanoparticles of different magnetic metals was explored. Many avenues for further work on these methods have been identified, however not exhaustively. Other novel properties of these well defined nanoparticles such as SERS enhancements, catalysis and other applications could be examined.

Appendix A

Table of Digestive Ripening Experiment Conditions

In table A.1, the “Au shell growth” precursor solution referred to is explained in chapter 5, and contains a gold precursor concentration of 5.55 mM. The AgNO_3 concentration of 5 mM was used to closely match the gold shell growth solution used.

TABLE A.1: Table of digestive ripening experiments performed (chapter 5)

Name	Au seeded nanorice (mL)	Ag seeded nanorice (mL)	Deionised water (mL)	5 mM AgNO ₃ (aq) (mL)	Au shell growth sol (aq) (mL)	PVP mw~40,000 (mg)	NaOH _(aq) (mL, M)	THPC _(aq) (mL, mM)	Temp (°C)	Time (hours)
DR1	0.073	-	30	-	5	40	2.5, 0.2	2.5, 20	60	1
DR2	0.073	-	30	1.25	3.75	40	2.5, 0.2	2.5, 20	60	1
DR3	0.073	-	30	2.5	2.5	40	2.5, 0.2	2.5, 20	60	1
DR4	0.073	-	30	3.75	1.25	40	2.5, 0.2	2.5, 20	60	1
DR5	0.073	-	30	-	5	40	2.5, 0.2	2.5, 20	60	3
DR6	0.073	-	30	1.25	3.75	40	2.5, 0.2	2.5, 20	60	3
DR7	0.073	-	30	2.5	2.5	40	2.5, 0.2	2.5, 20	60	3
DR8	0.073	-	30	3.75	1.25	40	2.5, 0.2	2.5, 20	60	3
DR9	0.073	-	30	-	5	40	2.5, 0.2	2.5, 20	60	5
DR10	0.073	-	30	1.25	3.75	40	2.5, 0.2	2.5, 20	60	5
DR11	0.073	-	30	2.5	2.5	40	2.5, 0.2	2.5, 20	60	5
DR12	0.073	-	30	3.75	1.25	40	2.5, 0.2	2.5, 20	60	5
DR13	0.073	-	30	-	5	40	2.5, 0.2	2.5, 20	75	1
DR14	0.073	-	30	1.25	3.75	40	2.5, 0.2	2.5, 20	75	1
DR15	0.073	-	30	2.5	2.5	40	2.5, 0.2	2.5, 20	75	1
DR16	0.073	-	30	-	5	40	2.5, 0.2	2.5, 20	75	3
DR17	0.073	-	30	1.25	3.75	40	2.5, 0.2	2.5, 20	75	3
DR18	0.073	-	30	2.5	2.5	40	2.5, 0.2	2.5, 20	75	3
Continued on next page										

Table A.1 – continued from previous page

Name	Au seeded nanorice (mL)	Ag seeded nanorice (mL)	Deionised water (mL)	5 mM AgNO ₃ (aq) (mL)	Au shell growth sol (aq) (mL)	PVP mw~40,000 (mg)	NaOH (aq) (mL, M)	THPC (aq) (mL, mM)	Temp (°C)	Time (hours)
DR19	0.073	-	30	-	5	40	2.5, 0.2	2.5, 20	75	5
DR20	0.073	-	30	1.25	3.75	40	2.5, 0.2	2.5, 20	75	5
DR21	0.073	-	30	2.5	2.5	40	2.5, 0.2	2.5, 20	75	5
DR22	0.073	-	30	-	5	40	2.5, 0.2	2.5, 20	60	1
DR23	0.073	-	30	-	5	40	2.5, 0.2	2.5, 20	60	3
DR24	0.073	-	30	-	5	40	2.5, 0.2	2.5, 20	75	1
DR25	0.073	-	30	-	5	40	2.5, 0.2	2.5, 20	75	3
DR26	0.073	-	30	-	5	40	2.5, 0.2	2.5, 20	85	1
DR27	0.073	-	30	-	5	40	2.5, 0.2	2.5, 20	85	3
DR28	0.073	-	30	-	5	40	2.5, 0.2	2.5, 20	75	3
DR29	0.073	-	20	-	5	40	2.5, 0.2	2.5, 20	75	3
DR30	0.073	-	10	-	5	40	2.5, 0.2	2.5, 20	75	3
DR31	0.073	-	30	-	2.5	40	2.5, 0.4	2.5, 40	75	3
DR32	0.073	-	30	1	2	40	2.5, 0.4	2.5, 40	75	3
DR33	0.073	-	30	1.25	1.875	40	2.5, 0.4	2.5, 40	75	3
DR34	0.073	-	30	2.5	1.25	40	2.5, 0.4	2.5, 40	75	3
DR35	0.073	-	25	1.25	1.875	40	5, 0.4	5, 40	75	3
DR36	0.073	-	25	2.5	1.25	40	5, 0.4	5, 40	75	3
DR37	0.0584	-	30	-	5	40	2.5, 0.2	2.5, 20	75	3

Continued on next page

Table A.1 – continued from previous page

Name	Au seeded nanorice (mL)	Ag seeded nanorice (mL)	Deionised water (mL)	5 mM AgNO ₃ (aq) (mL)	Au shell growth sol (aq) (mL)	PVP mw~40,000 (mg)	NaOH (aq) (mL, M)	THPC (aq) (mL, mM)	Temp (°C)	Time (hours)
DR38	0.0438	-	30	-	5	40	2.5, 0.2	2.5, 20	75	3
DR39	0.0292	-	30	-	5	40	2.5, 0.2	2.5, 20	75	3
DR40	0.0146	-	30	-	5	40	2.5, 0.2	2.5, 20	75	3
DR41	0.0876	-	30	-	5	40	2.5, 0.2	2.5, 20	75	3
DR42	0.1022	-	30	-	5	40	2.5, 0.2	2.5, 20	75	3
DR43	0.1168	-	30	-	5	40	2.5, 0.2	2.5, 20	75	3
DR44	0.1314	-	30	-	5	40	2.5, 0.2	2.5, 20	75	3
DR45	0.073	-	30	-	4	40	2.5, 0.2	2.5, 20	75	3
DR46	0.073	-	30	-	3	40	2.5, 0.2	2.5, 20	75	3
DR47	0.073	-	30	-	2	40	2.5, 0.2	2.5, 20	75	3
DR48	0.073	-	30	-	1	40	2.5, 0.2	2.5, 20	75	3
DR49	0.073	-	30	0.5	4.5	40	2.5, 0.2	2.5, 20	75	3
DR50	0.073	-	30	1	4	40	2.5, 0.2	2.5, 20	75	3
DR51	0.073	-	30	1.5	3.5	40	2.5, 0.2	2.5, 20	75	3
DR52	0.073	-	30	2	3	40	2.5, 0.2	2.5, 20	75	3
DR53	0.073	-	30	2.5	2.5	40	2.5, 0.2	2.5, 20	75	3
DR54	0.073	-	30	3	2	40	2.5, 0.2	2.5, 20	75	3
DR55	0.073	-	30x4	-	5x4	40	2.5, 0.2	2.5, 20	75	3
DR56	0.073	-	30x4	2.5x4	2.5x4	40	2.5, 0.2	2.5, 20	75	3

Continued on next page

Table A.1 – continued from previous page

Name	Au seeded nanorice (mL)	Ag seeded nanorice (mL)	Deionised water (mL)	5 mM AgNO ₃ (aq) (mL)	Au shell growth sol (aq) (mL)	PVP mw~40,000 (mg)	NaOH (aq) (mL, M)	THPC (aq) (mL, mM)	Temp (°C)	Time (hours)
DRS1	-	0.073	30	-	2.5	40	2.5, 0.2	2.5, 20	75	3
DRS2	-	0.073	30	1	2	40	2.5, 0.2	2.5, 20	75	3
DRS3	-	0.073	30	2	1.5	40	2.5, 0.2	2.5, 20	75	3
DRS4	-	0.073	30	3	1	40	2.5, 0.2	2.5, 20	75	3
DRS5	-	0.073	30	4	0.5	40	2.5, 0.2	2.5, 20	75	3
DRS6	-	0.073	30	5	-	40	2.5, 0.2	2.5, 20	75	3

Appendix B

Table of Interface Coating Experiment Conditions

In table B.1, the table of experiment parameters are divided into groups of experiments that looked to vary a couple or so variables at any one time.

When “(A)” is seen in the CTAB column it indicates that this surfactant was added to the reaction vessel after the heating step and the interface film had been formed. When an experiment has been performed in multiple coating steps, then values for volumes of reagents may appear as “10x4” which indicates that the same volume (10 mL) of reagent solution has been used for each coating step with centrifuge washing performed on the precipitate particles between steps. Whereas if “10+5” is shown, this indicates that 10 mL of a reagent was used in the first coating stage, followed by a further 5 mL in the second coating stage.

If an experiment was performed with multiple coating steps, but some parameters are displayed only once, then this same parameter value was used for each coating step.

IC53-56 were all performed keeping synthesised particles in the same reaction vessel between coating steps, not being washed by centrifuge, and with further reagents added to the vessel in the second coating step.

Appendix B. Table of Interface Coating Experiment Conditions

159

Table B.1 – continued from previous page

Name	Au(PPh ₃)Cl (mL, mM)	Ag(PPh ₃) ₃ Cl (mL, mM)	NaOH (mL, mM)	THPC (mL @ 50 mM)	Au seeded core (mL, solvent)	APTES- core in toluene (mL)	CTAB (mL, mM)	PVP (mg)	Time (hours)	Coating steps
IC63	20, 1.5	-	16, 12.5	0.66	-	0.146	0.5, 25 (A)	-	3	1
IC64	10, 1.5	10, 1.5	16, 12.5	0.66	-	0.146	0.5, 25 (A)	-	3	1
IC65	20, 1.5	-	16, 12.5	0.66	-	0.146	0.5, 25 (A)	-	5	1
IC66	10, 1.5	10, 1.5	16, 12.5	0.66	-	0.146	0.5, 25 (A)	-	5	1
IC67	8, 1.5	2, 1.5	16, 6.25	0.66	-	0.146	0.5, 25 (A)	-	3	1
IC68	6, 1.5	4, 1.5	16, 6.25	0.66	-	0.146	0.5, 25 (A)	-	3	1
IC69	8, 1.5	2, 1.5	16, 6.25	0.33x2	-	0.146	0.5, 25 (A)	-	3	2
IC70	6, 1.5	4, 1.5	16, 6.25	0.33x2	-	0.146	0.5, 25 (A)	-	3	2

Appendix C

Table of Polyol Experiment Conditions

In table C.1, the table of experiment parameters are divided into groups of experiments that looked to vary a couple or so variables at any one time.

In the column for Ethylene glycol; when two temperatures are listed, such as “160/170”, this means that the solvent temperature was at 160°C prior to precursor injection and then raised to 170°C following precursor injection. In the column for AgNO₃ when a volume is presented with an * this volume was injected instantaneously, while the remaining volume was injected at the specified rate. The column referring to “Ni seeds” refers to particles synthesised following the experiment parameters listed under the same name at the very end of the table, which were centrifuged as any others but were however re-dispersed in 20 mL EG. The column for centrifuge washing steps refers to an “initial” spin of the produced colloid, while “wash” steps are performed as the resulting precipitate is re-dispersed in deionised water and washed twice for the stated time, and likewise twice more in industrial methylated spirits. The final precipitate was always finally dispersed in a small amount of industrial methylated spirits for storage.

For samples NW67 and 68, in the PVP column 29k and 1,300k refers to the average molecular weight of PVP used, i.e. 29,000 and 1,300,000. The normal molecular weight PVP used for the rest of the experiments was 40,000. For sample NW69, FeCl₃ 4 mM was trialled to be used instead of the previously used CuCl₂ 4 mM solution.

TABLE C.1: Table of polyol experiments performed (chapter 7)

Name	Ethylene glycol (mL, °C)	AgNO ₃ (mL, M)	PVP (mL, M)	Ni(acetate) (mL, 0.1 M)	CuCl ₂ (μL, 4 mM)	Injection rate (mL/hr)	Silver or nickel precursor injected first	Nickel seeds (mL)	Centrifuge washing steps (initial / wash minutes)
NW1	10, 170	6, 0.1	6, 0.6	-	-	5	-	-	20/15
NW2	10, 170	6, 0.1	6, 0.6	-	-	10	-	-	20/15
NW3	10, 170	6, 0.1	6, 0.6	-	-	20	-	-	20/15
NW4	10, 170	6, 0.1	6, 0.6	-	-	5	-	-	20/15
NW5	10, 160	6, 0.1	6, 0.6	-	-	10	-	-	20/15
NW6	10, 160	6, 0.1	6, 0.6	-	-	20	-	-	20/15
NW7	10, 160	6, 0.1	6, 0.6	-	-	5	-	-	20/15
NW8	10, 160	6, 0.1	6, 0.6	-	-	10	-	-	20/15
NW9	10, 170	3, 0.1	6, 0.6	3	-	20	-	-	20/15
NW10	10, 170	3, 0.1	6, 0.6	3	-	5	-	-	20/15
NW11	10, 170	3, 0.1	6, 0.6	3	-	10	-	-	20/15
NW12	10, 170	3, 0.1	6, 0.6	3	-	20	-	-	20/15
NW13	10, 180	3, 0.1	6, 0.6	3	-	5	-	-	20/15
NW14	10, 180	3, 0.1	6, 0.6	3	-	10	-	-	20/15
NW15	10, 180	3, 0.1	6, 0.6	3	-	20	-	-	20/15
NW16	10, 180	5, 0.1	6, 0.6	1	-	5	-	-	20/15
NW17	10, 170	5, 0.1	6, 0.6	1	-	10	-	-	20/15
NW18	10, 170	5, 0.1	6, 0.6	1	-	20	-	-	20/15
Continued on next page									

Table C.1 – continued from previous page

Name	Ethylene glycol (mL, °C)	AgNO ₃ (mL, M)	PVP (mL, M)	Ni(acetate) (mL, 0.1 M)	CuCl ₂ (μL, 4 mM)	Injection rate (mL/hr)	Silver or nickel precursor injected first	Nickel seeds (mL)	Centrifuge washing steps (initial / wash minutes)
NW19	10, 170/180	4, 0.1	6, 0.6	2	-	-5	-	-	20/15
NW20	10, 180	4, 0.1	6, 0.6	2	-	10	-	-	20/15
NW21	10, 180	4, 0.1	6, 0.6	2	-	20	-	-	20/15
NW22	10, 170	3, 0.1	6, 0.6	3	-	5	-	-	20/15
NW23	10, 170	3, 0.1	6, 0.6	3	-	10	-	-	20/15
NW24	10, 170	3, 0.1	6, 0.6	3	-	20	-	-	20/15
NW25	10, 170	5, 0.1	6, 0.6	1	-	5	-	-	20/15
NW26	10, 170	5, 0.1	6, 0.6	1	-	10	-	-	20/15
NW27	10, 170	5, 0.1	6, 0.6	1	-	20	-	-	20/15
NW28	10, 170/180	4, 0.1	6, 0.6	2	-	5	-	-	20/15
NW29	10, 170	4, 0.1	6, 0.6	2	-	10	-	-	20/15
NW30	10, 170	4, 0.1	6, 0.6	2	-	20	-	-	20/15
NW31	10, 170/180	3, 0.1	6, 0.6	3	-	5	-	-	20/15
NW32	10, 170	3, 0.1	6, 0.6	3	-	10	-	-	20/15
NW33	10, 170	3, 0.1	6, 0.6	3	-	20	-	-	20/15
NW34	10, 170	5, 0.1	6, 0.6	1	-	5	-	-	20/15
NW35	10, 170	5, 0.1	6, 0.6	1	-	10	-	-	20/15
NW36	10, 170	5, 0.1	6, 0.6	1	-	20	-	-	20/15
NW37	10, 170/180	4, 0.1	6, 0.6	2	-	5	-	-	20/15
Continued on next page									

Table C.1 – continued from previous page

Name	Ethylene glycol (mL, °C)	AgNO ₃ (mL, M)	PVP (mL, M)	Ni(acetate) (mL, 0.1 M)	CuCl ₂ (μL, 4 mM)	Injection rate (mL/hr)	Silver or nickel precursor injected first	Nickel seeds (mL)	Centrifuge washing steps (initial / wash minutes)
NW57	10, 170	5, 0.2	7, 0.3	-	160	10	-	-	20/15
NW58	10, 170	4, 0.2	8, 0.3	-	160	10	-	-	20/15
NW59	10, 170	3, 0.2	9, 0.3	-	160	10	-	-	20/15
NW60	10, 170	5, 0.1	7, 0.6	-	160	10	-	-	20/15
NW61	10, 170	4, 0.1	8, 0.6	-	160	10	-	-	20/15
NW62	10, 170	3, 0.1	9, 0.6	-	160	10	-	-	20/15
NW63	10, 165	2*/4, 0.1	6, 0.6	-	160	10	-	-	20/15
NW64	10, 165	5, 0.1	6, 0.6	-	160	10	Nickel	1	20/15
NW65	10, 165	4, 0.1	6, 0.6	-	160	10	Nickel	2	20/15
NW66	10, 165	3*/3, 0.1	6, 0.6	-	160	10	-	-	20/15
NW67	10, 160	4, 0.1	6, 0.6 (29k mw)	2	160	10	Silver	-	20/15
NW68	10, 160	4, 0.1	6, 0.6 (1,300k mw)	2	160	10	Silver	-	20/15
NW69	10, 165	6, 0.1	6, 0.6	-	160 (FeCl ₃)	10	-	-	20/15
Ni seeds	10, 170	-	5, 0.6	5	-	-	-	-	20/15

Appendix C. Table of Polyol Experiment Conditions

Appendix D

Supplementary HRTEM images

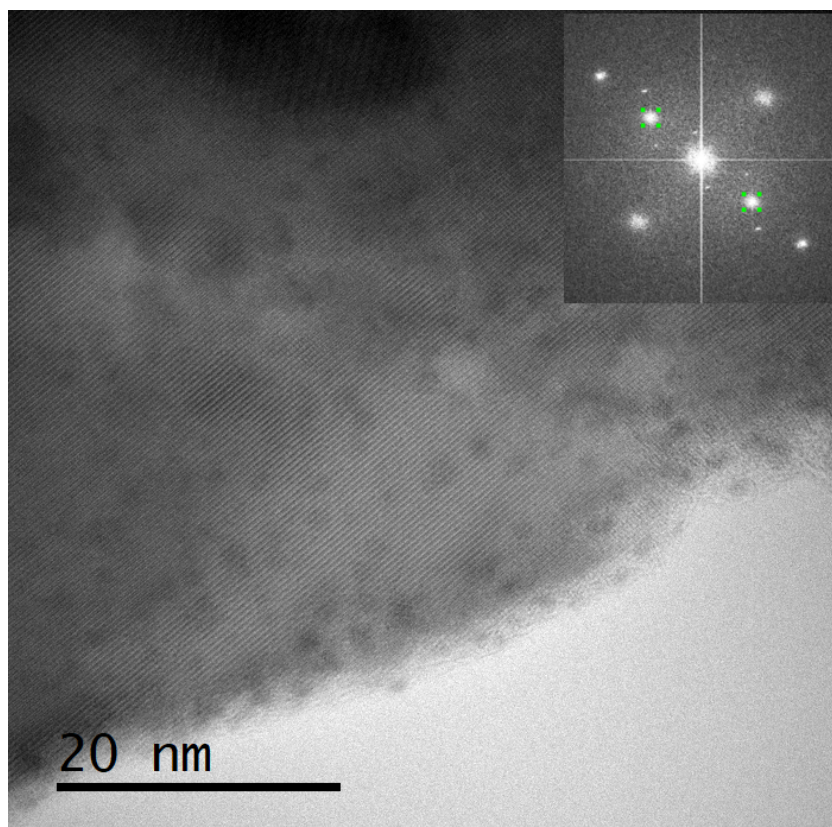


FIGURE D.1: HRTEM image of sample DR42 with inset electron diffraction pattern

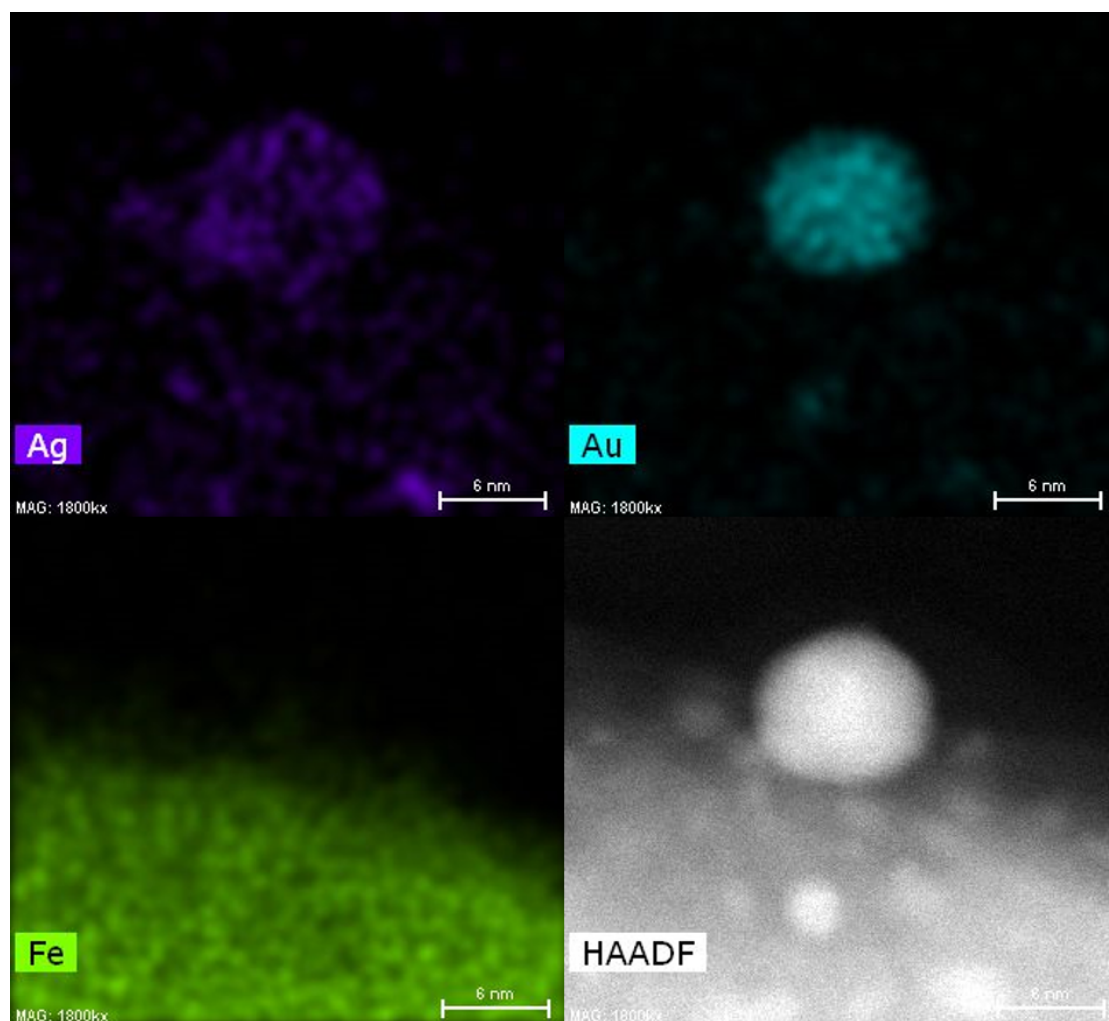


FIGURE D.2: HRTEM-EDX image and mapping of sample DR51 showing presence of gold-silver core-shell morphology deposited on hematite core

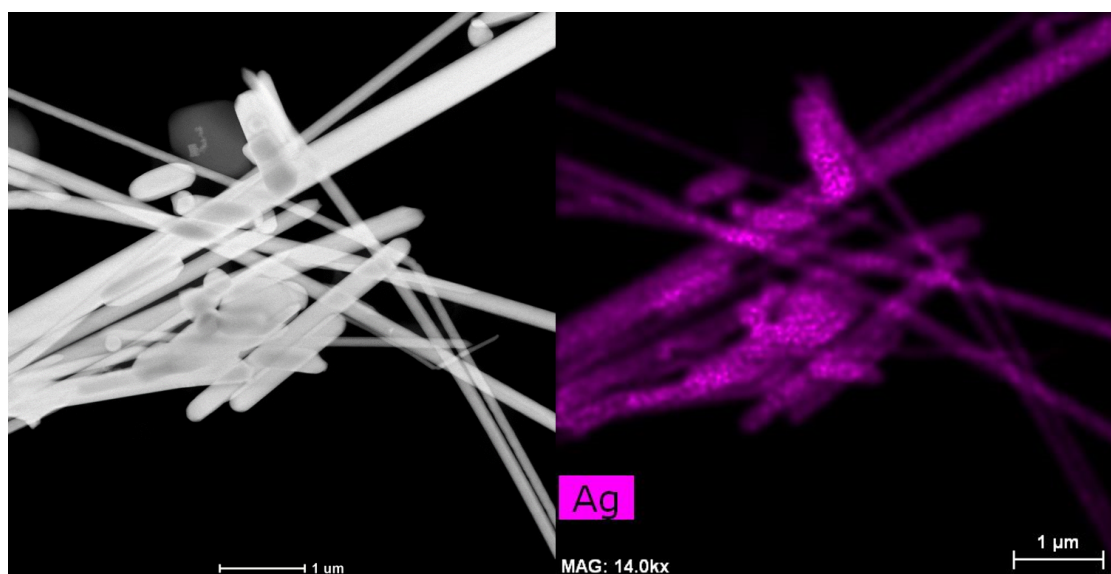


FIGURE D.3: HRTEM-EDX image of NW46 showing presence of silver only

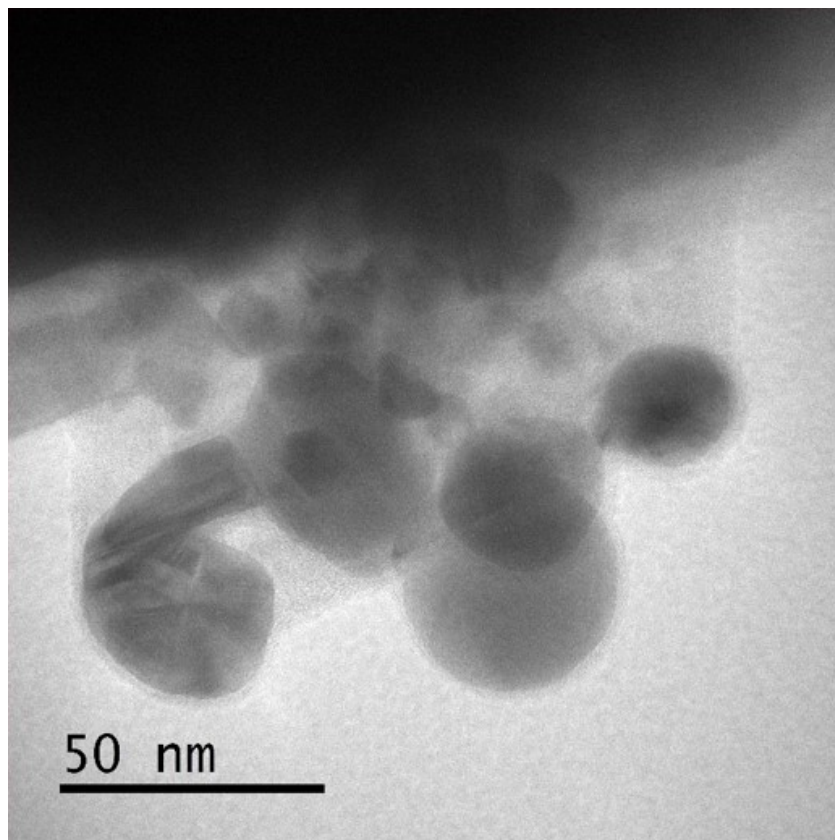


FIGURE D.4: HRTEM image of crystalline nickel or nickel oxide particles produced from reduction of $\text{Ni}(\text{CH}_3\text{CO}_2)_2 \cdot 4\text{H}_2\text{O}$ in ethylene glycol

Bibliography

- [1] C. Rao, P. Thomas and G. Kulkarni, in *Nanocrystals: Synthesis, Properties and Applications*, Springer-Verlag, Berlin, 2007, ch. 1 Basics of Nanocrystals, p. 182.
- [2] S. Link and M. a. El-Sayed, *Int. Rev. Phys. Chem.*, 2000, **19**, 409–453.
- [3] B. M. I. van der Zande, M. R. Böhmer, L. G. J. Fokkink and C. Schönenberger, *Langmuir*, 2000, **16**, 451–458.
- [4] M. Arruebo, R. Fernández-pacheco, M. R. Ibarra and J. Santamaría, *Nano Today*, 2007, **2**, 22–32.
- [5] S. Schrittwieser, D. Reichinger and J. Schotter, *Materials*, 2017, **11**, 1–28.
- [6] T. Sugimoto, *J. Colloid Interface Sci.*, 2007, **309**, 106–118.
- [7] T. Teranishi and M. Miyake, *Chem. Mater.*, 1998, **10**, 594–600.
- [8] Y. Chevalier and M.-A. Bolzinger, *Colloids Surf., A*, 2013, **439**, 23–34.
- [9] Y. Liu, Y. Li, X. M. Li and T. He, *Langmuir*, 2013, **29**, 15275–15282.
- [10] D. S. Sidhaye and B. L. V. Prasad, *New J. Chem.*, 2011, **35**, 755–763.
- [11] Levine, Samuel, Bowen, Bruce D. and Partridge, Susan J., *Colloids and Surfaces*, 1989, **38**, 325–343.
- [12] B. Wiley, Y. Sun and Y. Xia, *Acc. Chem. Res.*, 2007, **40**, 1067–1076.
- [13] K. E. Korte, S. E. Skrabalak and Y. Xia, *J. Mater. Chem.*, 2008, **18**, 437–441.

- [14] R. D. Shannon, *Acta Crystallographica Section A*, 1976, **32**, 751–767.
- [15] I. Chakraborty and T. Pradeep, *Chem. Rev.*, 2017, **117**, 8208–8271.
- [16] F. Baletto and R. Ferrando, *Rev. Mod. Phys.*, 2005, **77**, 371–423.
- [17] M. Faraday, *Phil. Trans. R. Soc.*, 1857, **147**, 145–181.
- [18] P. P. Edwards and J. M. Thomas, *Angew. Chem. Int. Ed.*, 2007, **46**, 5480–5486.
- [19] Y. Xia, Y. Xiong, B. Lim and S. E. Skrabalak, *Angew. Chem. Int. Ed.*, 2009, **48**, 60–103.
- [20] E. Roduner, *Chem. Soc. Rev.*, 2006, **35**, 583–592.
- [21] Y. Wang, J. He, C. Liu, W. H. Chong and H. Chen, *Angew. Chem. Int. Ed.*, 2015, **54**, 2022–2051.
- [22] E. G. C. Neiva, M. F. Bergamini, M. M. Oliveira, L. H. Marcolino and A. J. G. Zarbin, *Sens. Actuators, B*, 2014, **196**, 574–581.
- [23] J. a. Scholl, A. L. Koh and J. a. Dionne, *Nature*, 2012, **483**, 421–427.
- [24] J. Wilcoxon, *J. Phys. Chem. B*, 2009, **113**, 2647–2656.
- [25] D. Barchiesi, *J. Opt. Soc. Am. A*, 2015, **32**, 1544–1555.
- [26] I. Freestone, N. Meeks, M. Sax and C. Higgitt, *Gold Bull.*, 2007, **40**, 270–277.
- [27] D. J. Barber and I. C. Freestone, *Archaeometry*, 1990, **32**, 33–45.
- [28] P. L. Truong, X. Ma and S. J. Sim, *Nanoscale*, 2014, **6**, 2307–2315.
- [29] G. Mie, *Ann. Phys.*, 1908, **330**, 377–445.
- [30] T. Wriedt, in *The Mie Theory*, ed. W. Hergert and T. Wriedt, Springer-Verlag Berlin Heidelberg, Berlin, Heidelberg, 2012, vol. 169 of Springer Series in Optical Sciences, ch. 2, pp. 53–71.
- [31] I. Mejac, W. W. Bryan, T. R. Lee and C. D. Tran, *Anal. Chem.*, 2009, **81**, 6687–6694.

- [32] H. Horvath, *J. Quant. Spectrosc. Radiat. Transfer*, 2009, **110**, 787–799.
- [33] J. Duque, J. Blandón and H. Riascos, *J. Phys. Conf. Ser.*, 2017, **850**, 012017.
- [34] W. Haiss, N. T. K. Thanh, J. Aveyard and D. G. Fernig, *Anal. Chem.*, 2007, **79**, 4215–4221.
- [35] A. L. González, C. Noguez, J. Beránek and A. S. Barnard, *J. Phys. Chem. C*, 2014, **118**, 9128–9136.
- [36] L. M. Liz-Marzán, *Langmuir*, 2006, **22**, 32–41.
- [37] J. Langer, S. M. Novikov and L. M. Liz-Marzán, *Nanotechnology*, 2015, **26**, 322001.
- [38] S. Eustis and M. El-Sayed, *J. Phys. Chem. B*, 2005, **109**, 16350–16356.
- [39] I. Ojea-Jimenez, J. Comenge, L. Garcia-Fernandez, Z. Megson, E. Casals and V. Puentes, *Curr. Drug Metab.*, 2013, **14**, 518–530.
- [40] Y. Wu, M. R. Ali, K. Chen, N. Fang and M. A. El-Sayed, *Nano Today*, 2019, **24**, 120–140.
- [41] Y. Xia, X. Xia and H. C. Peng, *J. Am. Chem. Soc.*, 2015, **137**, 7947–7966.
- [42] B. Sepúlveda, P. C. Angelomé, L. M. Lechuga and L. M. Liz-Marzán, *Nano Today*, 2009, **4**, 244–251.
- [43] A. Jakab, C. Rosman, Y. Khalavka, J. Becker, A. Trügler, U. Hohenester and C. Sönnichsen, *ACS Nano*, 2011, **5**, 6880–6885.
- [44] S. Chikazumi and S. Charap, *Physics of magnetism*, R. E. Krieger Pub. Co., 1978.
- [45] Néel, M. Louis, *Ann. Phys.*, 1948, **12**, 137–198.
- [46] Q. A. Pankhurst, J. Connolly, S. K. Jones and J. Dobson, *J. Phys. D: Appl. Phys.*, 2003, **36**, R167–R181.
- [47] D. Newman, R. Matelon, M. Wears, L. Savage, J. Heptinstall, J. Beddow and M. Cox, 2008 IEEE PhotonicsGlobal@Singapore, 2008.

- [48] S. Schrittwieser, J. Schotter, T. Maier, R. Bruck, P. Muellner, N. Kataeva, K. Soulantica, F. Ludwig, A. Huetten and H. Brueckl, *Procedia Eng.*, 2010, **5**, 1107–1110.
- [49] S. Schrittwieser, B. Pelaz, W. J. Parak, S. Lentijo-Mozo, K. Soulantica, J. Dieckhoff, F. Ludwig, T. Altantzis, S. Bals and J. Schotter, *ACS Appl. Mater. Interfaces*, 2016, **8**, 8893–8899.
- [50] P. Yager, G. J. Domingo and J. Gerdes, *Annu. Rev. Biomed. Eng.*, 2008, **10**, 107–144.
- [51] D. M. Newman, J. Heptinstall, R. J. Matelon, L. Savage, M. L. Wears, J. Beddow, M. Cox, H. D. Schallig and P. F. Mens, *Biophys. J.*, 2008, **95**, 994–1000.
- [52] *Molecular Electro-Optics*, ed. S. Krause, Springer US, 1981.
- [53] C. Rizzo, A. Rizzo and D. M. Bishop, *Int. Rev. Phys. Chem.*, 1997, **16**, 81–111.
- [54] J. Fock, C. Balceris, R. Costo, L. Zeng, F. Ludwig and M. F. Hansen, *Nanoscale*, 2018, **10**, 2052–2066.
- [55] D. Coursault, I. Dozov, C. Blanc, M. Nobili, L. Dupont, C. Chanéac and P. Davidson, *Materials*, 2017, **10**, 1191.
- [56] S. Schrittwieser, B. Pelaz, W. J. Parak, S. Lentijo-Mozo, K. Soulantica, J. Dieckhoff, F. Ludwig and J. Schotter, *Sci. Rep.*, 2017, **7**, 1–6.
- [57] J. Fock, C. Jonasson, C. Johansson and M. F. Hansen, *Phys. Chem. Chem. Phys.*, 2017, **19**, 8802–8814.
- [58] S. Schrittwieser, F. Ludwig, J. Dieckhoff, K. Soulantica, G. Viau, L.-M. Lacroix, S. M. Lentijo, R. Boubekri, J. Maynadié, A. Huetten, H. Brueckl and J. Schotter, *ACS Nano*, 2011, **6**, 791–801.
- [59] H. Wang, D. W. Brandl, F. Le, P. Nordlander and N. J. Halas, *Nano Lett.*, 2006, **6**, 827–832.
- [60] P. F. Mens, R. J. Matelon, B. Y. Nour, D. M. Newman and H. D. Schallig, *Malar. J.*, 2010, **9**, 1–8.

- [61] J. Polte, *CrystEngComm*, 2015, **17**, 6809–6830.
- [62] V. K. LaMer and R. H. Dinegar, *J. Am. Chem. Soc.*, 1950, **72**, 4847–4854.
- [63] N. T. K. Thanh, N. Maclean and S. Mahiddine, *Chem. Rev.*, 2014, **114**, 7610–7630.
- [64] F. Wang, V. N. Richards, S. P. Shields and W. E. Buhro, *Chem. Mater.*, 2013, **26**, 5–21.
- [65] Y. Sun, B. Mayers, T. Herricks and Y. Xia, *Nano Lett.*, 2003, **3**, 955–960.
- [66] L. D. Marks, *Rep. Prog. Phys.*, 1994, **57**, 603–649.
- [67] P. J. Thomas, O. L. Armstrong and S. N. Baxter, in *Metal Nanoparticles and Clusters*, Springer International Publishing, 2017, ch. 2, pp. 31–54.
- [68] L. M. Rossi, J. L. Fiorio, M. A. Garcia and C. P. Ferraz, *Dalton Trans.*, 2018, **47**, 5889–5915.
- [69] A. T. Cawley and U. Flenker, *Journal of mass spectrometry : JMS*, 2008, **43**, 854–864.
- [70] G. K. Pradhan and K. M. Parida, *ACS Appl. Mater. Interfaces*, 2011, **3**, 317–323.
- [71] S. Musić, S. Krehula, S. Popović and Ž. Skoko, *Mater. Lett.*, 2003, **57**, 1096–1102.
- [72] W. Wang, J. Y. Howe and B. Gu, *J. Phys. Chem. C*, 2008, **112**, 9203–9208.
- [73] M. Ozaki, S. Kratochvil and E. Matijevic, *J. Colloid Interface Sci.*, 1984, **102**, 146–151.
- [74] X. M. Lin, G. M. Wang, C. M. Sorensen and K. J. Klabunde, *J. Phys. Chem. B*, 1999, **103**, 5488–5492.
- [75] X. Lin, C. M. Sorensen and K. J. Klabunde, *J. Nanopart. Res.*, 2000, **2**, 157–164.
- [76] D. K. Lee, S. I. Park, J. K. Lee and N. M. Hwang, *Acta Mater.*, 2007, **55**, 5281–5288.
- [77] D. K. Lee and N. M. Hwang, *Scr. Mater.*, 2009, **61**, 304–307.

- [78] B. L. V. Prasad, S. I. Stoeva, C. M. Sorensen and K. J. Klabunde, *Chem. Mater.*, 2003, **15**, 935–942.
- [79] D. Jose, J. E. Matthiesen, C. Parsons, C. M. Sorensen and K. J. Klabunde, *J. Phys. Chem. Lett.*, 2012, **3**, 885–890.
- [80] B. Prasad, S. Stoeva, C. Sorensen and K. Klabunde, *Langmuir*, 2002, **18**, 7515–7520.
- [81] P. Sahu, J. Shimpi, H. J. Lee, T. R. Lee and B. L. V. Prasad, *Langmuir*, 2017, **33**, 1943–1950.
- [82] P. Sahu and B. L. V. Prasad, *Chem. Phys. Lett.*, 2012, **525-526**, 101–104.
- [83] Y. Ji, S. Yang, S. Guo, X. Song, B. Ding and Z. Yang, *Colloids Surf., A*, 2010, **372**, 204–209.
- [84] A. B. Smetana, K. J. Klabunde, C. M. Sorensen, A. A. Ponce and B. Mwale, *J. Phys. Chem. B*, 2006, **110**, 2155–2158.
- [85] S. P. Bhaskar and B. R. Jagirdar, *J. Chem. Sci.*, 2012, **124**, 1175–1180.
- [86] C. Bhattacharya and B. R. Jagirdar, *J. Phys. Chem. C*, 2018, **122**, 10559–10574.
- [87] P. Sahu and B. L. V. Prasad, *Langmuir*, 2014, **30**, 10143–10150.
- [88] F. Kim, S. Kwan, J. Akana and P. Yang, *J. Am. Chem. Soc.*, 2001, **123**, 4360–4361.
- [89] K. Ariga, Y. Yamauchi, T. Mori and J. P. Hill, *Adv. Mater.*, 2013, **25**, 6477–6512.
- [90] P. J. Thomas, G. U. Kulkarni, P. Saravanan, C. N. R. Rao and V. V. Agrawal, *J. Phys. Chem. B*, 2003, **107**, 7391–7395.
- [91] H. A. Chaghouri, M. A. Malik, P. J. Thomas and P. O. Brien, *J. Nanosci. Nanotechnol.*, 2016, **16**, 1–6.
- [92] F. Fievet, J. Lagier and M. Figlarz, *MRS Bull.*, 1989, **14**, 29–34.
- [93] F. Fievet, J. P. Lagier, B. Blin, B. Beaudoin and M. Figlarz, *Solid State Ion.*, 1989, **32-33**, 198–205.

- [94] F. Fievet, S. Ammar-Merah, R. Brayner, F. Chau, M. Giraud, F. Mammeri, J. Peron, J. Y. Piquemal, L. Sicard and G. Viau, *Chem. Soc. Rev.*, 2018, **47**, 5187–5233.
- [95] Y. Sun, Y. Yin, B. T. Mayers, T. Herricks and Y. Xia, *Chem. Mater.*, 2002, **14**, 4736–4745.
- [96] F. Dumestre, B. Chaudret, C. Amiens, M.-C. Fromen, M.-J. Casanove, P. Renaud and P. Zurcher, *Angew. Chem. Int. Ed.*, 2002, **41**, 4286–4289.
- [97] F. Wetz, K. Soulantica, A. Falqui, M. Respaud, E. Snoeck and B. Chaudret, *Angew. Chem. Int. Ed.*, 2007, **46**, 7079–7081.
- [98] B. Cormary, T. Li, N. Liakakos, L. Peres, P.-F. Fazzini, T. Blon, M. Respaud, A. J. Kropf, B. Chaudret, J. T. Miller, E. A. Mader and K. Soulantica, *J. Am. Chem. Soc.*, 2016, **138**, 8422–8431.
- [99] F. Wetz, K. Soulantica, M. Respaud, A. Falqui and B. Chaudret, *Mater. Sci. Eng., C*, 2007, **27**, 1162–1166.
- [100] R. Aveyard, B. P. Binks and J. H. Clint, *Adv. Colloid Interface Sci.*, 2003, **100-102**, 503 – 546.
- [101] V. V. Agrawal, P. Mahalakshmi, G. U. Kulkarni and C. N. R. Rao, *Langmuir*, 2006, **22**, 1846–1851.
- [102] V. Garbin, J. C. Crocker and K. J. Stebe, *J. Colloid Interface Sci.*, 2012, **387**, 1–11.
- [103] L. L. Dai, R. Sharma and C.-y. Wu, *Langmuir*, 2005, **21**, 2641–2643.
- [104] Y. Lin, A. Böker, H. Skaff, D. Cookson, A. D. Dinsmore, T. Emrick and T. P. Russell, *Langmuir*, 2005, **21**, 191–194.
- [105] R. Aveyard, J. H. Clint and T. S. Horozov, *Physical Chemistry Chemical Physics*, 2003, **5**, 2398–2409.
- [106] D. Fu, P. G. Keech and J. C. Wren, *Phys. Chem. Chem. Phys.*, 2011, **13**, 18523–18529.

- [107] R. L. Parfitt, *Adv. Agron.*, 1979, **30**, 1–50.
- [108] M. Spuch-Calvar, J. Pérez-Juste and L. M. Liz-Marzán, *J. Colloid Interface Sci.*, 2007, **310**, 297–301.
- [109] Z. Cai, E. S. P. Leong, Z. Wang, W. Niu, W. Zhang, S. Ravaine, N. L. Yakovlev, Y. J. Liu, J. Teng and X. Lu, *J. Mater. Chem. C*, 2015, **3**, 11645–11652.
- [110] X. Hu and J. C. Yu, *Adv. Funct. Mater.*, 2008, **18**, 880–887.
- [111] Z. Ma, H. Han, S. Tu and J. Xue, *Colloids Surf., A*, 2009, **334**, 142–146.
- [112] N. J. Reeves and S. Mann, *J. Chem. Soc., Faraday Trans.*, 1991, **87**, 3875–3880.
- [113] T. Sugimoto, Y. Wang, H. Itoh and A. Muramatsu, *Colloids Surf., A*, 1998, **134**, 265–279.
- [114] A. Breeuwsma and J. Lyklema, *J. Colloid Interface Sci.*, 1973, **43**, 437–448.
- [115] C. Frandsen, B. A. Legg, L. R. Comolli, H. Zhang, B. Gilbert, E. Johnson and J. F. Banfield, *CrystEngComm*, 2014, **16**, 1451–1458.
- [116] M. Ocaña, M. P. Morales and C. J. Serna, *J. Colloid Interface Sci.*, 1995, **171**, 85–91.
- [117] J. Kim, W. Li, B. L. Philips and C. P. Grey, *Energy and Environmental Science*, 2011, **4**, 4298–4305.
- [118] R. L. Parfitt, R. J. Atkinson and R. S. C. Smart, *Soil Sci. Soc. Am. J.*, 1975, **39**, 837–841.
- [119] M. A. Zayed, M. A. Ahmed, N. G. Imam and D. H. El Sherbiny, *J. Supercond. Novel Magn.*, 2016, **29**, 2899–2916.
- [120] W. Wei, W. Zhao, Y. Taekyung, J. Changzhong and K. Woo-Sik, *Sci. Technol. Adv. Mater.*, 2015, **16**, 23501.
- [121] T. K. Indira and P. Lakshmi, *Int. J. Pharm. Sci. Nanotech*, 2010, **3**, 1035–1042.
- [122] B. Mehdaoui, A. Meffre, L.-M. Lacroix, J. Carrey, S. Lachaize, M. Respaud, M. Gougeon and B. Chaudret, *J. Appl. Phys.*, 2010, **107**, 09A324–1–09A324–3.

- [123] N. Singh, G. J. Jenkins, R. Asadi and S. H. Doak, *Nano Rev.*, 2010, **1**, 1–15.
- [124] M. Z. Ahmad, B. A. Abdel-Wahab, A. Alam, S. Zafar, J. Ahmad, F. J. Ahmad, P. Midoux, C. Pichon and S. Akhter, *J. Nanosci. Nanotechnol.*, 2016, **16**, 7873–7897.
- [125] M. Mahmoudi, a. Simchi and M. Imani, *J. Iran. Chem. Soc.*, 2010, **7**, 1–27.
- [126] E. N. Maslen, V. A. Streltsov, N. R. Streltsova and N. Ishizawa, *Acta Cryst. B*, 1994, **50**, 435–441.
- [127] R. L. Blake and R. E. Hessevick, *Am. Mineral.*, 1966, **51**, 123–129.
- [128] D. Trpkov, M. Panjan, L. Kopanja and M. Tadić, *Appl. Surf. Sci.*, 2018, **457**, 427–438.
- [129] F. J. Morin, *Phys. Rev.*, 1950, **78**, 819–820.
- [130] D. Bersani, P. P. Lottici and A. Montenero, *J. Raman Spectrosc.*, 1999, **30**, 355–360.
- [131] K. F. McCarty, *Solid State Commun.*, 1988, **68**, 799–802.
- [132] Ö. Özdemir, D. J. Dunlop and T. S. Berquó, *Geochem. Geophys. Geosyst.*, 2008, **9**, 1–12.
- [133] A. G. Kolhatkar, A. C. Jamison, D. Litvinov, R. C. Willson and T. R. Lee, *Int. J. Mol. Sci.*, 2013, **14**, 15977–16009.
- [134] S. B. Wang, Y. L. Min and S. H. Yu, *J. Phys. Chem. C*, 2007, **111**, 3551–3554.
- [135] F. Bødker and S. Mørup, *Europhys. Lett.*, 2000, **52**, 217–223.
- [136] X. Zhang, Y. Niu, Y. Li, X. Hou, Y. Wang, R. Bai and J. Zhao, *Mater. Lett.*, 2013, **99**, 111–114.
- [137] A.-H. Lu, E. Salabas and F. Schüth, *Angew. Chem. Int. Ed.*, 2007, **46**, 1222–1244.
- [138] J. E. Post and V. F. Buchwald, *Am. Mineral.*, 1991, **76**, 272–277.

- [139] R. Parameshwari, P. Priyadarshini and G. Chandrasekaran, *American Journal of Materials Science*, 2011, **1**, 18–25.
- [140] A. L. Morales and J.-m. Greneche, *Rev. Fac. Ing. Univ. Antioquia*, 2009, 185–191.
- [141] M. A. Garcia-Lobato, A. I. Martinez, M. Castro-Roman, C. Falcony and L. Escobar-Alarcon, *Physica B*, 2011, **406**, 1496–1500.
- [142] D. L. A. de Faria, S. Venâncio Silva and M. T. de Oliveira, *J. Raman Spectrosc.*, 1997, **28**, 873–878.
- [143] I. Chamritski and G. Burns, *J. Phys. Chem. B*, 2005, **109**, 4965–4968.
- [144] A. M. Jubb and H. C. Allen, *ACS Appl. Mater. Interfaces*, 2010, **2**, 2804–2812.
- [145] I. R. Beattie and T. R. Gilson, *J. Am. Chem. Soc.*, 1970, 980–986.
- [146] I. V. Chernyshova, M. F. Hochella and A. S. Madden, *Phys. Chem. Chem. Phys.*, 2007, **9**, 1736–1750.
- [147] S. Li and L. H. Hihara, *J. Electrochem. Soc.*, 2015, **162**, C495–C502.
- [148] Q. Wu, C. Zhang and F. Li, *Mater. Lett.*, 2005, **59**, 3672–3677.
- [149] C. Wu, P. Yin, X. Zhu, C. OuYang and Y. Xie, *J. Phys. Chem. B*, 2006, **110**, 17806–17812.
- [150] J. Velez, A. Bandyopadhyay, W. H. Butler and S. Sarker, *Phys. Rev. B*, 2005, **71**, 1–7.
- [151] K. Sivula, F. Le Formal and M. Grätzel, *ChemSusChem*, 2011, **4**, 432–449.
- [152] Gurudayal, P. M. Chee, P. P. Boix, H. Ge, F. Yanan, J. Barber and L. H. Wong, *ACS Appl. Mater. Interfaces*, 2015, **7**, 6852–6859.
- [153] P. Liao, M. C. Toroker and E. A. Carter, *Nano Lett.*, 2011, **11**, 1775–1781.
- [154] P. Liao, J. A. Keith and E. A. Carter, *J. Am. Chem. Soc.*, 2012, **134**, 13296–13309.
- [155] A. Akbar, S. Riaz, R. Ashraf and S. Naseem, *IEEE Trans. Magn.*, 2014, **50**, 2201204.

- [156] R. Satheesh, K. Vignesh, A. Suganthi and M. Rajarajan, *J. Environ. Chem. Eng.*, 2014, **2**, 1956–1968.
- [157] A. Yogi and D. Varshney, *Mater. Sci. Semicond. Process.*, 2014, **21**, 38–44.
- [158] R. Suresh, R. Prabu, A. Vijayaraj, K. Giribabu, A. Stephen and V. Narayanan, *Mater. Chem. Phys.*, 2012, **134**, 590–596.
- [159] T. I. Bhuiyan, M. Nakanishi, Y. Kusano, T. Fujii, J. Takada and Y. Ikeda, *J. Jpn. Soc. Powder. Powder. Metall.*, 2006, **54**, 112–118.
- [160] F. S. Freyria, G. Barrera, P. Tiberto, E. Belluso, D. Levy, G. Saracco, P. Allia, E. Garrone and B. Bonelli, *J. Solid State Chem.*, 2013, **201**, 302–311.
- [161] P. B. Johnson and R. W. Christy, *Phys. Rev. B*, 1972, **6**, 4370–4379.
- [162] P. K. Jain, S. Eustis and M. A. El-Sayed, *The Journal of Physical Chemistry B*, 2006, **110**, 18243–18253.
- [163] J. Nonkumwong, P. Pakawanit, A. Wipatanawin, P. Jantaratana, S. Ananta and L. Srisombat, *Mater. Sci. Eng., C*, 2016, **61**, 123–132.
- [164] J. Zhang, X. Liu, L. Wang, T. Yang, X. Guo, S. Wu, S. Wang and S. Zhang, *J. Phys. Chem. C*, 2011, **115**, 5352–5357.
- [165] S. P. Yeap, P. Y. Toh, A. L. Ahmad, S. C. Low, S. A. Majetich and J. Lim, *J. Phys. Chem. C*, 2012, **116**, 22561–22569.
- [166] S. P. Schwaminger, P. F. García, G. K. Merck, F. A. Bodensteiner, S. Heissler, S. Günther and S. Berensmeier, *J. Phys. Chem. C*, 2015, **119**, 23032–23041.
- [167] H. Zhu, E. Zhu, G. Ou, L. Gao and J. Chen, *Nanoscale Res. Lett.*, 2010, **5**, 1755–1761.
- [168] X. Xu and M. B. Cortie, *J. Phys. Chem. C*, 2007, **111**, 18135–18142.

- [169] S. Lentijo-Mozo, R. P. Tan, C. Garcia-Marcelot, T. Altantzis, P. F. Fazzini, T. Hungria, B. Cormary, J. R. Gallagher, J. T. Miller, H. Martinez, S. Schrittwieser, J. Schotter, M. Respaud, S. Bals, G. V. Tendeloo, C. Gatel and K. Soulan-tica, *ACS Nano*, 2015, **9**, 2792–2804.
- [170] J.-h. Kim, W. W. Bryan and T. R. Lee, *Langmuir*, 2008, **24**, 11147–11152.
- [171] D. E. Gheorghe, L. Cui, C. Karmonik, A. Brazdeikis, J. M. Penaloza, J. K. Young, R. a. Drezek and M. Bikram, *Nanoscale Res. Lett.*, 2011, **6**, 554.
- [172] O. V. Dement'eva, M. a. Filippenko, M. E. Kartseva, E. M. Sedykh, L. N. Bannykh, R. I. Yakubovskaya, a. a. Pankratov, B. Y. Kogan and V. M. Rudoy, *Nanotechnol. Russ.*, 2012, **7**, 517–526.
- [173] O. V. Dement'eva, M. E. Kartseva, V. M. Sukhov and V. M. Rudoy, *Colloid J.*, 2017, **79**, 605–610.
- [174] M. E. Kartseva, O. V. Dement'eva, M. A. Filippenko and V. M. Rudoy, *Colloid J.*, 2011, **73**, 340–344.
- [175] S. Oldenburg, R. Averitt, S. Westcott and N. J. Halas, *Chem. Phys. Lett.*, 1998, **288**, 243–247.
- [176] C. Graf and A. van Blaaderen, *Langmuir*, 2002, **18**, 524–534.
- [177] D. G. Duff, A. Baiker and P. P. Edwards, *J. Chem. Soc. Chem. Commun.*, 1993, **272**, 2301–2309.
- [178] K. Biswas, N. Varghese and C. N. R. Rao, *Small*, 2008, **4**, 649–655.
- [179] W. W. Bryan, A. C. Jamison, P. Chinwangso, S. Rittikulsittichai, T.-C. Lee and T. R. Lee, *RSC Adv.*, 2016, **6**, 68150–68159.
- [180] C.-C. Huang, H.-Y. Liao, Y.-C. Shiang, Z.-H. Lin, Z. Yang and H.-T. Chang, *J. Mater. Chem.*, 2009, **19**, 755–759.
- [181] J. L. Hueso, V. Sebastián, Á. Mayoral, L. Usón, M. Arruebo and J. Santamaría, *RSC Adv.*, 2013, **3**, 10427–10433.

- [182] K. Luo, C. Hu, Y. Luo, D. Li, Y. Xiang, Y. Mu, H. Wang and Z. Luo, *RSC Adv.*, 2017, **7**, 51605–51611.
- [183] J. Turkevich, P. C. Stevenson and J. Hillier, *Discuss. Faraday Soc.*, 1951, **11**, 55.
- [184] G. Frens, *Nat. Phys. Sci.*, 1973, **241**, 20–22.
- [185] C. Deraedt, L. Salmon, S. Gatard, R. Ciganda, R. Hernandez, J. Ruiz and D. Astruc, *Chem. Commun.*, 2014, **50**, 14194–14196.
- [186] J. L. Lyon, D. A. Fleming, M. B. Stone, P. Schiffer and M. E. Williams, *Nano Lett.*, 2004, **4**, 719–723.
- [187] A. Sood, V. Arora, J. Shah, R. Kotnala and T. K. Jain, *J. Exp. Nanosci.*, 2015, 1–13.
- [188] Z. Xu, Y. Hou and S. Sun, *J. Am. Chem. Soc.*, 2007, **129**, 8698–8699.
- [189] B. L. Sanchez-Gaytan and S.-J. Park, *Langmuir*, 2010, **26**, 19170–19174.
- [190] W. Wu, Q. He, H. Chen, J. Tang and L. Nie, *Nanotechnology*, 2007, **18**, 145609.
- [191] H. H. Kyaw, S. H. Al-Harhi, A. Sellai and J. Dutta, *Beilstein J. Nanotechnol.*, 2015, **6**, 2345–2353.
- [192] Y. Y. Song, H. Hildebrand and P. Schmuki, *Surf. Sci.*, 2010, **604**, 346–353.
- [193] F. A. Cotton and G. Wilkinson, *Advanced Inorganic Chemistry : A Comprehensive Text*, John Wiley & Sons, New York, N.Y., 4th edn., 1980.
- [194] Y. Qu, Y. Yang, Z. Zou, C. Zeilstra, K. Meijer and R. Boom, *ISIJ Int.*, 2014, **54**, 2196–2205.
- [195] B. L. V. Prasad, C. M. Sorensen and K. J. Klabunde, *Chem. Soc. Rev.*, 2008, **37**, 1871–1883.
- [196] M.-C. Daniel and D. Astruc, *Chem. Rev.*, 2004, **104**, 293–346.
- [197] C. Burda, X. Chen, R. Narayanan and M. A. El-Sayed, *Chem. Rev.*, 2005, **105**, 1025–1102.

- [198] N.-M. Hwang, J.-S. Jung and D.-K. Lee, in *Thermodynamics - Fundamentals and Its Application in Science*, InTech, 2012, ch. 14, pp. 371–388.
- [199] M. L. Lin, F. Yang, J. S. Peng and S. Lee, *J. Appl. Phys.*, 2014, **115**, 1–8.
- [200] Y. Yang, X. Gong, H. Zeng, L. Zhang, X. Zhang, C. Zou and S. Huang, *J. Phys. Chem. C*, 2010, **114**, 256–264.
- [201] B. P. Binks, *Curr. Opin. Colloid Interface Sci.*, 2002, **7**, 21–41.
- [202] B. P. Binks, *Langmuir*, 2017, **33**, 6947–6963.
- [203] Y. Lin, *Science*, 2003, **299**, 226–229.
- [204] K. Du, E. Glogowski, T. Emrick, T. P. Russell and A. D. Dinsmore, *Langmuir*, 2010, **26**, 12518–12522.
- [205] P. J. Thomas, E. Mbufu and P. O’Brien, *Chem. Commun.*, 2013, **49**, 118–127.
- [206] K. Luo, S. L. M. Schroeder and R. A. W. Dryfe, *Chem. Mater.*, 2009, **21**, 4172–4183.
- [207] G. L. Stansfield, H. M. Johnston, S. N. Baxter and P. J. Thomas, *RSC Advances*, 2018, **8**, 6225–6230.
- [208] G. L. Stansfield and P. J. Thomas, *J. Am. Chem. Soc.*, 2012, **134**, 11888–11891.
- [209] P. J. Thomas, E. Albrasi, S. N. Mlondo and P. O’Brien, *J. Phys. Chem. C*, 2011, **115**, 14668–14672.
- [210] J. Yang, E. Sargent, S. Kelley and J. Y. Ying, *Nat. Mater.*, 2009, **8**, 683–689.
- [211] M. Brust, M. Walker, D. Bethell, D. J. Schiffrin and R. Whyman, *J. Chem. Soc., Chem. Commun.*, 1994, **0**, 801–802.
- [212] M. Tran, R. Depenning, M. Turner and S. Padalkar, *Mater. Res. Express*, 2016, **3**, 1–10.
- [213] G. Doria, J. Conde, B. Veigas, L. Giestas, C. Almeida, M. Assunção, J. Rosa and P. V. Baptista, *Sensors*, 2012, **12**, 1657–1687.

- [214] Y. Lu, C. Zhang, R. Hao, D. Zhang, Y. Fu, S. Moeendarbari, C. S. Pickering, Y. Hao and Y. Liu, *Mater. Res. Express*, 2016, **3**, 055014.
- [215] B. Li, S. Ye, I. E. Stewart, S. Alvarez and B. J. Wiley, *Nano Lett.*, 2015, **15**, 6722–6726.
- [216] T. Cheng, Y. Zhang, W. Lai, Y. Chen and W. Huang, *Chin. J. Chem.*, 2015, **33**, 147–151.
- [217] Q. N. Luu, J. M. Doorn, M. T. Berry, C. Jiang, C. Lin and P. S. May, *J. Colloid Interface Sci.*, 2011, **356**, 151–158.
- [218] F. Bonet, K. Tekaia-Elhsissen and K. Vijaya Sarathy, *Bull. Mater. Sci.*, 2000, **23**, 165–168.
- [219] S. Coskun, B. Aksoy and H. E. Unalan, *Cryst. Growth Des.*, 2011, **11**, 4963–4969.
- [220] S. E. Skrabalak, B. J. Wiley, M. Kim, E. V. Formo and Y. Xia, *Nano Lett.*, 2008, **8**, 2077–2081.
- [221] H. Mao, J. Feng, X. Ma, C. Wu and X. Zhao, *J. Nanopart. Res.*, 2012, **14**, 1–15.
- [222] P. Zhang, I. Wyman, J. Hu, S. Lin, Z. Zhong, Y. Tu, Z. Huang and Y. Wei, *Mater. Sci. Eng., B Solid. State. Mater. Adv. Technol.*, 2017, **223**, 1–23.
- [223] W. A. Saidi, H. Feng and K. A. Fichthorn, *J. Phys. Chem. C*, 2013, **117**, 1163–1171.
- [224] J.-Y. Lin, Y.-L. Hsueh and J.-J. Huang, *J. Solid State Chem.*, 2014, **214**, 2–6.
- [225] J. Jung, D. Seo, G. Park, S. Ryu and H. Song, *J. Phys. Chem. C*, 2010, **114**, 12529–12534.
- [226] B. Liu, H. Yan, S. Chen, Y. Guan, G. Wu, R. Jin and L. Li, *Nanoscale Res. Lett.*, 2017, **12**, 212.
- [227] B. Wiley, Y. Sun and Y. Xia, *Langmuir*, 2005, **21**, 8077–8080.
- [228] G. G. Couto, J. J. Klein, W. H. Schreiner, D. H. Mosca, A. J. A. de Oliveira and A. J. G. Zarbin, *J. Colloid Interface Sci.*, 2007, **311**, 461–468.

- [229] P. Li, J. Guan, Q. Zhang and W. Zhao, *J. Wuhan. Univ. Technol. Mat. Sci. Edit.*, 2005, **20**, 35–37.
- [230] K. J. Carroll, J. U. Reveles, M. D. Shultz, S. N. Khanna and E. E. Carpenter, *J. Phys. Chem. C*, 2011, **115**, 2656–2664.
- [231] M. McKiernan, J. Zeng, S. Ferdous, S. Verhaverbeke, K. S. Leschkies, R. Gouk, C. Lazik, M. Jin, A. L. Briseno and Y. Xia, *Small*, 2010, **6**, 1927–1934.
- [232] R. Yuksel, S. Coskun, Y. E. Kalay and H. E. Unalan, *J. Power Sources*, 2016, **328**, 167–173.
- [233] B. K. Mehta, M. Chhajlani and B. D. Shrivastava, *J. Phys. Conf. Ser.*, 2017, **836**, 012050.
- [234] J. Richardson, *Appl. Catal., A*, 2003, **246**, 137–150.
- [235] I. K. Bdikin, G. K. Strukova, G. Strukov, V. Kedrov, D. Matveev, S. Zverkov and A. L. Kholkin, *Mater. Sci. Forum*, 2006, **514–516**, 1166–1170.
- [236] C. Yang, Y. Tang, Z. Su, Z. Zhang and C. Fang, *J. Mater. Sci. Technol.*, 2015, **31**, 16–22.
- [237] H. D. Jang, D. W. Hwang, D. P. Kim, H. C. Kim, B. Y. Lee and I. B. Jeong, *Mater. Res. Bull.*, 2004, **39**, 63–70.
- [238] V. F. Puentes, *Science*, 2001, **291**, 2115–2117.
- [239] J. Wu and G.-H. Ma, *Small*, 2016, **12**, 4633–4648.
- [240] P. Pieranski, *Phys. Rev. Lett.*, 1980, **45**, 569–572.
- [241] J. Zhou, X. Qiao, B. P. Binks, K. Sun, M. Bai, Y. Li and Y. Liu, *Langmuir*, 2011, **27**, 3308–3316.